SINGLE MOLECULE INTERACTION BETWEEN CARBOHYDRATE-BINDING MODULES AND PLANT CELL WALL CELLULOSE

by

MENGMENG ZHANG

(Under the Direction of Bingqian Xu)

ABSTRACT

The world now greatly needs new sources of liquid transportation fuels to solve the economic and environmental problems. Enzymatic degradation of lignocellulosic biomass, mainly plant cell walls, has been considered as the most promising process for biofuel production. However, this process is greatly limited by the natural resistance of plant cell walls and inefficient enzyme-cellulose interactions. The carbohydrate-binding modules (CBMs) in the carbohydrate-active enzymes can facilitate the accessibility of enzymes by specifically binding to the target carbohydrates. As the beginning step in cellulose hydrolysis, the binding affinity and mechanism of this process is critical, but still unclear down to molecular level. Therefore, understanding single molecular CBM-cellulose interaction is greatly needed to improve the enzymatic hydrolysis of biomass.

In this study, a specific and reliable single-molecule approach was applied to study the CBM-cellulose binding interactions. With a CBM-functionalized AFM tip, the binding specificity and affinities of two CBMs to poplar cell wall crystalline cellulose were determined by AFM recognition imaging and single molecule dynamic force spectroscopy (SMDFS). Several dynamic and kinetic parameters were quantified on

natural and extracted plant cell wall cellulose at single-molecule level, such as unbinding forces, reconstructed free energy change, energy barrier, and bond lifetime. Specifically, a CBM3a molecule showed slightly higher binding efficiency and affinity than those of a CBM2a molecule to both natural and extracted crystalline cellulose. Both CBMs showed higher affinities to natural cellulose microfibrils than those to extracted cellulose microfibrils. The cell walls of poplar, switchgrass and corn stover before and after dilute acid pretreatment were also characterized. The results showed that the cell wall surface coverage of crystalline cellulose increased from 17-20% to 22-38% after pretreatment under different acid concentrations at 135 ^{o}C, and corn stover pretreated with 0.5% acid revealed an optimized distribution of crystalline cellulose on surface. A minimal effective CBM3a concentration of 5.1×10^{-7} M at a comparatively short reaction time of 287 min was also quantified for a more economic hydrolysis process. This study provides an in-depth understanding of the binding mechanism of CBMs to cellulose and may pave the way for advanced enzyme design and biomass degradation.

INDEX WORDS: Cellulose, the Plant cell walls, Carbohydrate-binding module (CBM), Pretreatment, Atomic force microscopy (AFM), Recognition imaging, Single molecule dynamic force spectroscopy (SMDFS), Single molecule dynamics and kinetics

SINGLE MOLECULE INTERACTION BETWEEN CARBOHYDRATE-BINDING MODULES AND PLANT CELL WALL CELLULOSE

by

MENGMENG ZHANG

BS, Dalian University of Technology, P. R. China, 2009

A Dissertation Submitted to the Graduate Faculty of The University of Georgia in Partial Fulfillment of the Requirements for the Degree

DOCTOR OF PHILOSOPHY

ATHENS, GEORGIA

2014

SINGLE MOLECULE INTERACTION BETWEEN CARBOHYDRATE-BINDING MODULES AND PLANT CELL WALL CELLULOSE

by

MENGMENG ZHANG

Major Professor: Bingqian Xu

Committee: Geert-Jan Boons
Ying Xu

Electronic Version Approved:

Julie Coffield
Interim Dean of the Graduate School
The University of Georgia
August 2014

DEDICATION

I dedicate this dissertation to my wonderful and warm family, particularly to my supportive and encouraging father Hongwei Zhang, and mother Ling Bai for their constructive suggestions for my doctoral study and good-to-excellent tendance for my life. Wish they can always be proud of me. I also thank other family members for their ubiquitous care and support during my study abroad.

ACKNOWLEDGEMENTS

This is my fifth year in the University of Georgia as a graduate student. I can hardly believe how time flies in my study toward the doctorate. Pursuing a doctorate is never an easy process. It cost plenty of time, efforts and patience and also taught me how to grow up and be more mature as a researcher in the academic field. I also feel very glad and lucky to have the chances to meet so many important people on my way to the achievements. Here I'd like to express my sincerest gratitude to them for their unselfish help and support, which has made my research experience so memorable and fruitful.

My first and deepest gratitude is to my major advisor, Dr. Bingqian Xu, for accepting me as a member of his diligent research group, and the full financial support during my doctoral research. In my entire research period, Dr. Xu kept showing patience and providing remarkable ideas and suggestions to guide me toward the real academic fields with his great accomplishments and rich experience in scientific research. His generosity, kindness and responsibility for his students also helped me overcome the hardest time in both my research and my life. I always feel honored to be able to achieve my research goals under his supervision and encouragement.

I also want to thank my knowledgeable and responsible committee members, Dr. Geert-Jan Boons and Dr. Ying Xu. I'm grateful for their support and acknowledgement to my research and many constructive suggestions, which can make me more qualified as a scientific researcher. I sincerely thank Dr. Jason Locklin and Dr. Leidong Mao for their interesting and helpful classes and generosity for sharing the lab equipment. In some

collaborated work, I acknowledge Dr. Sheng-Cheng Wu for his help in binding module preparation, and Dr. Rajeev Kumar from University of California, Riverside for his help and suggestions in biomass pretreatment. I appreciate Ms. Beth Richardson from Department of Plant Biology and Ms. Mary Ard from Department of Pathology for their help in biomass sample preparations. I also appreciate Dr. Jim Kastner and Dr. Sudhagar Mani from College of Engineering for providing biomass pretreatment facilities.

I also owe my thanks to many bright and kind-hearted fellows and friends for their help and support. I'd like to appreciate all members in Xu lab: Dr. Guojun Chen demonstrated the AFM system operation, tip modification and sample preparation to me. Dr. Jianfeng Zhou introduced me some knowledge of AFM working principles and also help me with AFM operation and trouble-shooting. I also had a great time working with other previous and current group members: Dr. Cunlan Guo, Bin Wang, Joseph Hamill, Kun Wang and Zhichao Lou. My additional thanks also go to Taotao Zhu, Rui Cheng, Feng Liu, Yen-jun Chuang, Yifei Wu, Evan White, Joe Grubbs, Anandi Roy, Chunyuan Song, Shunli Wang, Wen Sun, Jing Chen, Xiaomeng Wu and Chengbo Zhou. Their kind help and encouragement enriched and delighted my research life at UGA.

The last but not least, the greatest motivation and support came from my beloved family. Thanks to my hard-working and vigorous parents, who have been doing a good job in their own careers and taking care of themselves, so that I can completely focus on my study and life abroad. I also want to apologize and thank for their understanding for not being able to go back home more often during the past 5 years.

Finally, I'd like to show my wholehearted appreciation for all other people those are not included due to my poor memory and limited space here. Thank you all!

TABLE OF CONTENTS

Page

LIST OF TABLES

Page

LIST OF FIGURES

Page

LIST OF ABBREVIATIONS

AFM	Atomic force spectroscopy
ANTA	N-5-(amino-1-carboxypentyl) iminodiacetic acid
Arg	Arginine
Asn	Asparagine
Asp	Aspartic acid
ATR-FTIR	Attenuated total reflectance Fourier transform infrared spectroscopy
BMCC	Bacterial microcrystalline cellulose
CD	Catalytic domain
CBM	Carbohydrate-binding module
CS	Corn stover
DAP	Dilute acid pretreatment
DMF	Dimethylformamide
DTSP	Dithiobis(N-succinimidyl propionate)
DTSP-ANTA	Dithiobis-(nitriloacetic acid butylamidylpropionate)
Gln	Glutamine
GNP	Gold nanoparticle
His	Histidine
HPLC	High performance liquid chromatography
IMAC	Immobilized metal affinity chromatography

IPTG	Isopropyl β-D-1-thiogalactopyranoside
IR	Infrared spectroscopy
NaGlu	Sodium glutamate
NMR	Nuclear magnetic resonance
NTA	Nitrilotriacetic acid; Short for DTSP-ANTA
PCR	Polymerase chain reaction
PDB	Protein data bank
PEG	Polyethylene glycol
RAP	Recognition area percentage
SG	Switchgrass
SEM	Scanning electron microscope
Ser	Serine
SMDFS	Single molecule dynamic force spectroscopy
SPM	Scanning probe microscopy
SPR	Surface plasmon resonance
TEA	Triethylamine
TEM	Transmission electron microscope
ToF-SIMS	Time-of-flight secondary ion mass spectrometry
*Tr*Cel7A	*Trichoderma reesei* Family 7 cellobiohydrolase
TREC	Topography and RECognition imaging
Trp	Tryptophan
Tyr	Tyrosine
XRD	X-ray diffraction

CHAPTER 1

INTRODUCTION

The efficient conversion of lignocellulosic biomass to biofuels, especially by cellulolytic enzymes, begins to draw more public attentions as an alternative energy source to replace the traditional fossil fuels. To overcome the resistance of plant cell walls and improve the efficiency of enzyme-carbohydrate interactions, the binding mechanisms of the non-catalytic, carbohydrate-binding modules (CBMs) of cellulolytic enzymes to the plant cell wall cellulose needs to be profoundly understood. As the beginning step in cellulose hydrolysis, study of CBM-cellulose interaction, especially down to single-molecule level has the potential of improving enzymatic hydrolysis of the plant cell walls by designing enzymes with high efficiency and low cost.

1.1 Lignocellulosic biomass for biofuels

Lignocellulosic biomass has long been considered as a renewable and promising feedstock for producing biofuels and other biomaterials.[1-2] As the most abundant source of lignocellulosic biomass, wood, grasses and most agricultural residues have been converted to simple sugars followed by fermentation to produce bio-ethanol to replace the fossil fuels in the past century.[3-4] The combustion of lignocellulosic ethanol also inhibits the increasing amount of net carbon dioxide in the atmosphere with potentials of high efficiency and low cost.[5-6] Therefore, replacing the fossil fuels with biofuels

becomes an urgent need, and a more efficient biomass degradation process is required to be intensively studied.

1.2 The plant cell walls

The plant cell walls have the largest abundance in organic carbon on the earth. They are mainly composed of the polysaccharides, e.g., cellulose, hemicelluloses, pectins, etc.[7-8] The components and structure of the plant cell walls has been extensively investigated for years.[9-11] The structure of a whole plant is broken down to molecular level in Figure 1.1. The plant cell walls mainly consist of middle lamellae, primary walls and secondary walls. Crystalline and amorphous cellulose is the skeleton of all cell wall layers. Different from primary walls, secondary walls are usually covered and rigidified by lignin, a heterogenous aromatic polymer.[12]

Chemical and physical processes using acids and/or bases are commonly applied to break down the plant cell wall structure to release the sugars in cellulose and hemicellulose. Due to the high specificity of cellulolytic enzymes, or rather cellulases, they are often favored in obtaining sugar products from cellulose in higher yields.[13] One huge barrier to biomass-ethanol conversion by enzymes is the contact and interaction between enzymes and the target carbohydrates trapped within the lignocelluloses. The plant cell walls have evolved a robust structure to resist enzymatic attack and can exhibit hydrolytic stability to survive in nature. This counteraction phenomenon is usually called “biomass recalcitrance", which is attributed to the crosslinking between the polysaccharides and lignin.[14-15] Therefore, a more profound understanding of these mechanisms becomes a necessity to optimize the biomass conversion process toward fermentable sugars and ultimate bioethanol.[7, 16-17]

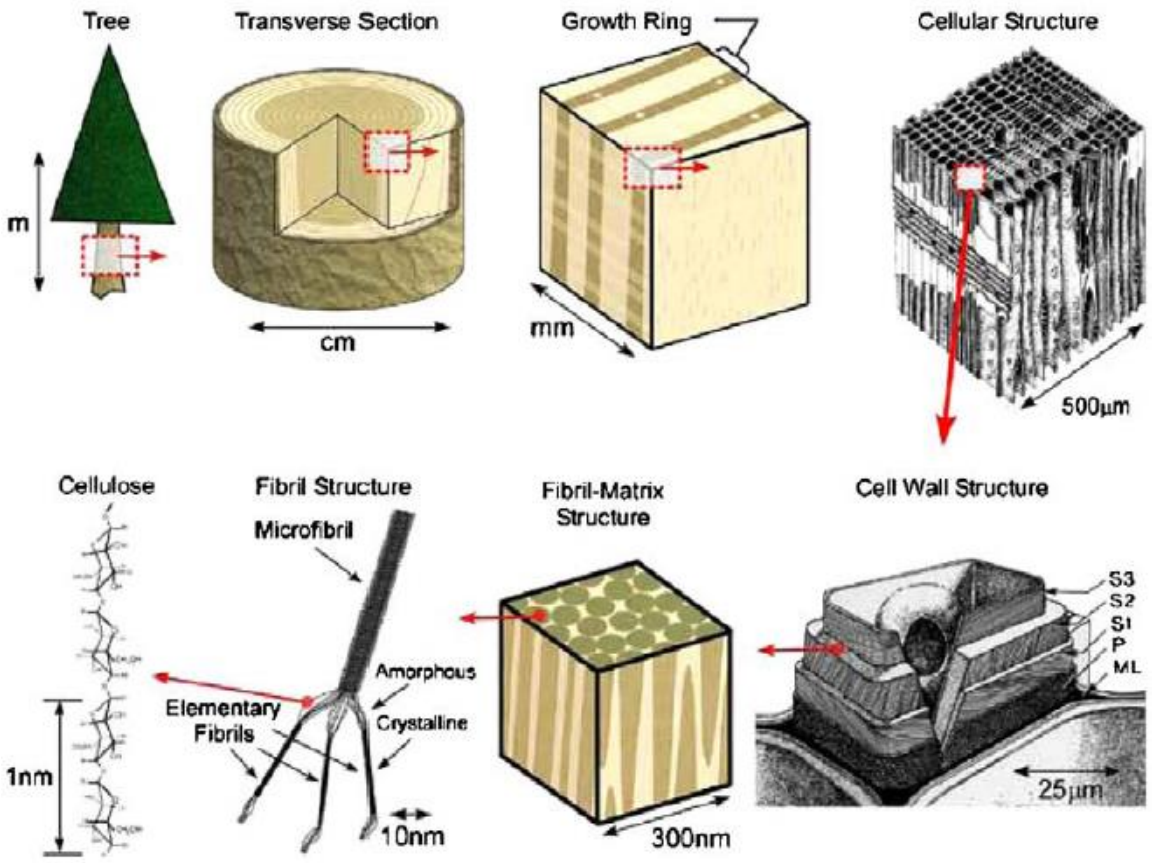

Figure 1.1 Structure of wood from the tree to the cellulose nanocrystals. ML = middle lamellae between tracheids, P = primary cell wall, S1, S2, S3 = cell wall layers.[18] (DOI: 10.1088/0957-0233/22/2/024005. © IOP Publishing. Reproduced by permission of IOP Publishing. All rights reserved)

Cellulose is the structural component of primary cell walls of green plants (from simple algae to higher trees). It is the major polysaccharide rich in organic carbon in renewable biomass.[19] In general, about 33% of all plant matter is in form of cellulose, e.g., 90% content in cotton and 40-50% content in wood. To overcome the recalcitrance during conversion of the biomass to fermentable sugars in biorefinery industry, it is critical to understand the structure and distribution of cellulose within the plant cell walls.[20-26]

Figure 1.2 illustrates the general structure and components of the plant cell walls.[11] Among all the cell wall components, cellulose is a polymer comprising a linear chain of $\beta(1\rightarrow4)$ linked D-glucose units with the formula $(C_6H_{10}O_5)_n$. The crystalline form of cellulose plays a very essential role in supporting plant structures. Hemicellulose is also made of carbohydrates covalently joined together in long chains, and generally includes five different sugars: xylose, mannose, glucose, galactose and arabinose.[27] Compared to cellulose, hemicellulose is an amorphous, branched polymer that can be more easily broken down by chemicals and enzymes.

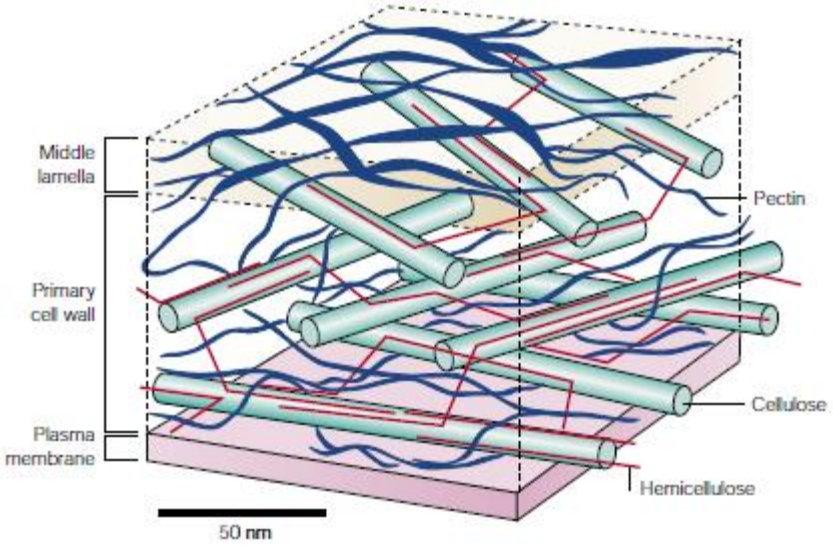

Figure 1.2 Schematics of plant cell wall components. Reprinted by permission from Macmillan Publishers Ltd: Nature Reviews Molecular Cell Biology,[11] copyright 2001.

As a straight chain polymer, cellulose presents an extended and stiff rod-like conformation constructed by the glucose residues. The chair conformation forces the -OH groups into equatorial positions and the aliphatic H atoms into axial positions. The

hydroxyl groups on the glucose from one chain are linked to oxygen molecules on the same or a neighbor chain by hydrogen bonds. The strong inter-chain hydrogen bonding between adjacent chains can hold the chains firmly together side-by-side to form microfibrils (about 5-30 nm in diameter), or large bundles (up to several hundred nm in diameter) packing in highly-ordered layers in a cellulose sheet.[14] Like most other natural polymers, cellulose bundles usually consist of both crystalline and amorphous regions. Natural crystalline cellulose is cellulose I, with structures I_α and I_β. Cellulose formed in bacteria and algae is enriched in I_α, while that of higher plants is mainly composed of I_β. Cellulose I_β is widely distributed in regenerated cellulose fibers and also more stable in property. [28-29]

In biological and industrial procedures, the photo-synthetically fixed organic carbon in the biomass is recycled by microbial enzymes, an important procedure of which can convert cell wall polysaccharides to monosaccharides and oligosaccharides.[30-32] However, more advanced technologies are still required to develop economical processes for this biomass-biofuels conversion, e.g., improving pretreatment processes to increase the output ratio of fermentable sugars to toxic byproducts, producing low-cost variations of cellulases in crystalline cellulose hydrolysis, etc.[33] Consequently, natural biomass degradation processes are generally achieved via molecular interactions between cellulolytic microbes/enzymes and well-ordered plant cell wall assemblies enwrapped by an irregular polymer matrix.[34]

Down to the molecular level, different from hemicellulose and amorphous cellulose which are readily digestible, the cellulose microfibrils are highly resistant to chemical and biological hydrolysis due to its rigid structure.[28] A dense layer of water

formed on the hydrophobic face of cellulose sheets adjacent to the hydrated cellulose surface makes crystalline cellulose resistant to acid hydrolysis.[35] Meanwhile, the strong inter-chain H-bonding network also prevents enzymatic hydrolysis process from crystalline cellulose.[14, 28-29, 35-36] This rigid structure is distinct after removing the adjacent linking and protective, but digestible polymeric substances, i.e., hemicelluloses, pectins, lignin, etc.[15, 32, 37-39] Compared to improving the chemical treatments of the biomass toward cellulose degradation, the biological methods, specifically by cellulolytic enzymes exhibit a milder and more environmental-friendly approach for biofuel production, the process and mechanism of which, therefore need to be well-understood.

1.3 Enzymatic hydrolysis of the plant cell walls

1.3.1 Carbohydrate-binding module (CBM)

The whole enzymatic hydrolysis process is initiated by the binding of the cellulolytic enzyme or the entire microorganism to the cellulose substrate. The non-catalytic protein segments that can be found in many carbohydrate-hydrolyzing enzymes are usually defined as carbohydrate-binding modules (CBMs), whose main functions are to recognize the target carbohydrate as the initial key step, and then convey the catalytic domains (CD) of these enzymes to the right place for hydrolysis (Figure 1.3).[40] The structure and functions of several CBMs have been investigated up till now; these CBMs have been grouped into more than 60 different families based on their sequence similarity on the continuously updated Carbohydrate-Active EnZymes (CAZy) database. [41-43]

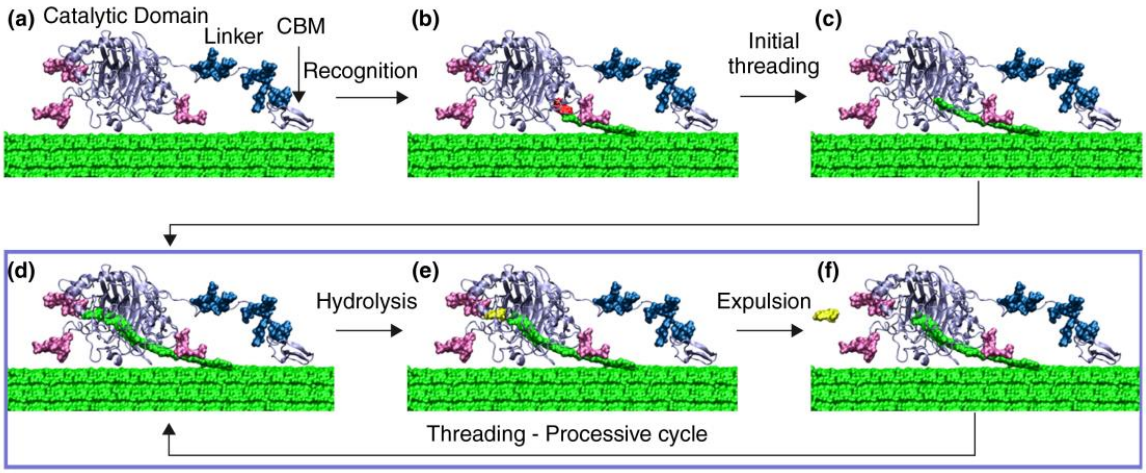

Figure 1.3 The *Trichoderma reesei* Family 7 cellobiohydrolase (*Tr*Cel7A) acting on cellulose surface. *Tr*Cel7A is comprised of a 36-amino acid CBM, a linker domain (dark blue), and a large catalytic domain with *N*-linked glycan (pink) and a 50-Å tunnel for processing cellulose chains (green). The cellobiose product is shown in yellow (e) and (f). Copyright 2011, with permission from Elsevier.[40]

Currently, the knowledge of structure and functions of CBMs introduces new insights into the mechanism of cellulose-enzyme interaction. It has been reported that increasing the concentration of enzymes on the surface of the substrate is able to cause more rapid degradation of the polysaccharide. Namely, genetic truncation of CBMs from the catalytic domains significantly reduces the activity of the enzymes on insoluble compared to soluble polysaccharides.[32, 44-49] However, to profoundly understand the binding mechanism, the cellulose-CBM interaction needs to be studied at single molecule level. This may reveal the binding process of a single CBM molecule and provide very essential information in designing more efficient enzymes for biomass-biofuel conversion.

Recent developments in the fields of optical and electron have demonstrated that single molecules can be observed at high resolution by fluorescence microscopy, scanning electron microscope (SEM), transmission electron microscope (TEM), etc.

These approaches are usually used to accomplish preliminary study of the carbohydrate-enzyme interaction via observation of specific binding sites and CBM behaviors by labeling target molecules with fluorescent tags, such as semiconductor quantum dots and fluorescent proteins.[50-51] Although the unique active site architecture of the CBMs and their binding sites on the crystalline cellulose surface have been widely studied and discussed, the detailed action of two domains, especially the targeting CBMs, and the cellulose-CBM binding kinetics on cellulose, are still indistinct down to single molecule level. The absence of the above information can significantly hinder the design and modification of effective cellulolytic enzymes; therefore obstruct the step of biofuel production behind the barrier of biomass recalcitrance.

Based on the experimentally verified structures, functions and ligand specificities, many CBMs have now been generally classified into three types: binding to specific surfaces of insoluble crystalline cellulose and/or chitin (type A), individual glycan chains (type B) and small sugars (type C). In addition to the major function as targeting group, CBMs are also presumed to mediate the non-hydrolytic disruption of cellulose fibers to facilitate the following continuous enzymatic degradation induced by the catalytic domains.[40, 43]

Theoretically, numerous simulation work and models have been developed to study the cellulose structure and interaction mechanism with CBMs.[20, 23, 26, 28-29, 36, 52-53] The conformation of the CBMs, how the CBMs bind to the cellulose surface via the multiple sets of critical binding sites, as well as the binding locations on cellulose surface, easiness and strength of the binding between the two, have long caught people's attention.[54-62]

Numerous studies have established that at least three aromatic residues on a CBM surface are needed in cellulose crystal-CBM binding activity, and tryptophan contributes to higher binding affinity than tyrosine.[63-67] For instance, the flat conserved surface at the bottom of a family 3 CBM (e.g. CBM3a) can interact hydrophobically with crystalline cellulose, involving the five amino acid residues (Trp118, Arg112, Asp56, His57 and Tyr67) which can form the planar strip (Figure 1.4).[68]

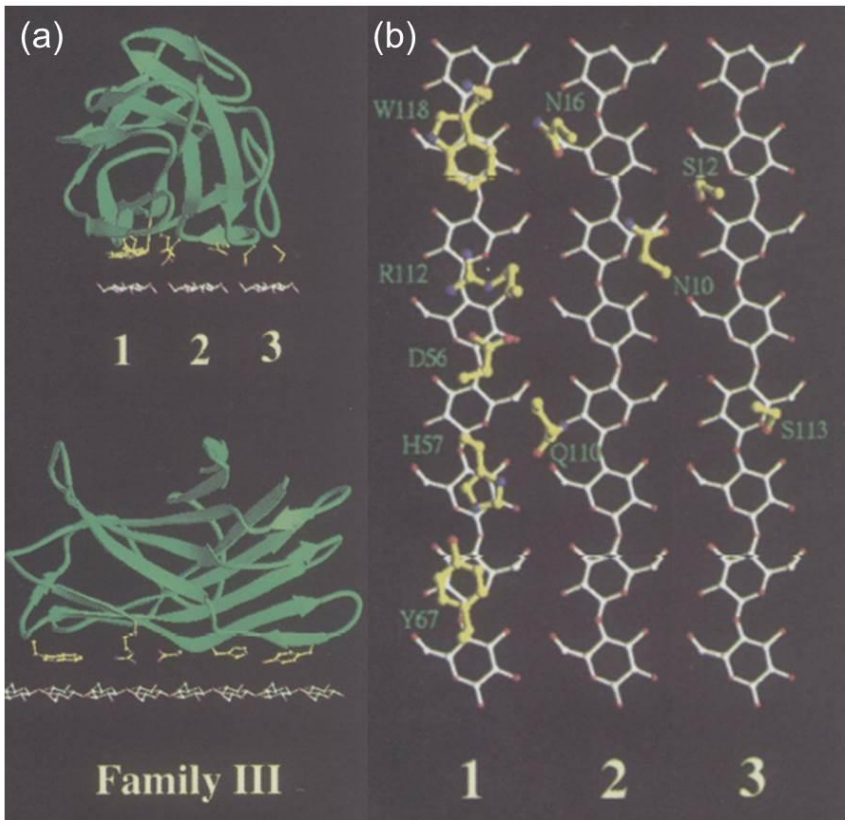

Figure 1.4 Model for the interaction of CBM3a with cellulose. (a) The lower view shows the three CBDs aligned along a single cellulose chain. In the upper panels in (a), the CBDs and cellulose chains have been rotated 90˚, separately, along the vertical axis, such that the CBDs are now aligned along three separate cellulose chains, designated 1, 2 and 3 for each structure. Amino acid side chains, which appear to interact with the cellulose, are shown in yellow. (B) Bird's-eye view of the residues proposed to interact with the cellulose chains. The residues, aligned along the cellulose chains, have been rotated 90˚ around the horizontal axis with respect to the orientations shown in the upper views of (a). The ribbon diagrams of the backbone traces have been omitted for clarity.

Similarly, McLean *et al.* reported that a family 2a carbohydrate-binding module (CBM2a) of xylanase 10A from *Cellulomonas fimi,* another type A CBM, also binds to crystalline cellulose.[69] In this work, series of conservative (phenylalanine and tyrosine) and non-conservative substitutions (alanine) of each solvent-exposed tryptophan (Trp17, Trp54 and Trp72 at the most critical locations) were prepared. They were then tested with other residues on the binding face with H-bonding potential replaced by alanine. The results demonstrated that the binding of CBM2a is predominantly mediated by three prominent, solvent-exposed tryptophan residues. With the knowledge of the most important binding residues and their locations in the CBM molecules, it is more feasible to look into the binding sites on the target carbohydrate substrate, especially crystalline cellulose and their distribution in the intricate plant cell walls.

1.4 Cellulose-CBM interaction studies

1.4.1 Characterization of the plant cell walls

A better fundamental understanding of how the structural elements assemble to form the plant cell walls is very significant for biomass degradation. Therefore, characterization of these structures with regard to their chemical and physical features at nano-scale is quite essential. Unfortunately, the commonly used diffraction-limited spectroscopic techniques (e.g., fluorescence, Raman scattering) are regarded as a barrier to high spatial resolution imaging.[21, 70-74] Some frequently used techniques to characterize the structure and chemical components of natural and pretreated plant cell walls are X-ray diffraction (XRD), nuclear magnetic resonance (NMR), infrared spectroscopy (IR), high performance liquid chromatography (HPLC), etc.[75-78] These techniques are widely

used as a combination to determine structural and component changes of the plant cell walls before and after pretreatments. However, the plant cell wall structure is usually completely or partially destroyed in the sample preparation procedures. Moreover, component changes determined by bulk chemical analysis do not necessarily reflect the surface changes. Traditionally, surface characterization of the plant cell walls have been frequently achieved by SEM and TEM.[79-82] Whereas, the sample preparation methods for the above techniques involves coating biological specimens with vaporized metal or carbon, or embedding plant specimens into a resin for stabilization to obtain a required thickness by thin sectioning. These preparation procedures used in biomass materials are considered to be very time-consuming and may ultimately change the native structure of the plant cell walls.

Comparatively, scanning probe microscopy (SPM), especially atomic force microscopy (AFM), provides a distinctive 'biophysical' methodology to investigate these materials at nano-scale with simple sample preparation procedure and perturbation.[83-85] In principle, AFM uses a micro-cantilever holding a nano-scale tip (with a radius less than 10 nm) at one end to scan the sample surface. The distance between tip and sample surface is adjusted by a feedback mechanism under the control of a piezoelectric scanner. The attractive or repulsive forces are sensitive to the surface structure and chemical properties of both the tip and sample, which can generate the deflections that are detected by photodiodes through a reflected laser spot. AFM has been used increasingly for characterizing biomolecules due to several distinct advantages. For instance, to minimize structural and activity (especially for biological specimens) modifications generated during sample preparation, samples can simply be measured in an almost *in vivo*

physiological environment (in air or aqueous environment); it is quite possible to get super high resolution (i.e., atomic even angstrom resolution); it is also possible to obtain topography (height image) and elasticitic (phase image) information of the sample simultaneously.[86-88] Although the major uncertainty for AFM measurements caused by scanning artifacts can generate misleading image broadening, these artifacts have been significantly minimized via better probe control, more accurate calibration and sharper tips.[89-93] AFM can also be used to characterize the surface morphology of the plant cell walls, as well as the binding and assembly of the cellulosome complex in the cellulosome system.[94-95]

Direct visualization of plant cell wall surface and pretreated cellulose microfibrils using AFM has proved to be able to successfully achieve imaging with higher resolution and more accurate measurement.[16] So far, several experimental results using AFM to do both the pure cellulose and pretreated plant cell walls imaging have been reported.[96-111] In order to clearly observe the binding faces on the crystalline cellulose, the first and critical step is to extract the pure cellulose microfibrils from the complicated fresh plant cell walls. An optimized condition is studying on a crystalline cellulose microfibril, which can clearly expose the distinct facets around the crystal chain to the cellulolytic enzymes. This can be achieved by disconnecting the cellulose from lignin with strong, dilute bases, acid-hydrolyzing the newly purified cellulose to dissolve amorphous region, and finally breaking them down into cellulose microfibrils or cellulose nanocrystals (whiskers).[111-119] Several works have been done to optimize pretreatments of the plant cell walls and extraction of crystalline cellulose under a low-cost and simpler process.[18, 120-125]

1.4.2 Imaging of cellulose-enzyme interactions

The high cost of cellulose-degrading enzymes remains a major hindrance on the way toward biomass conversion and biofuel production, since the catalytic efficiency of the cellulases is practically much lower than the theoretical values in the industrial production. The significant reasons are the lack of robust and cost-effective cellulases and more importantly, the direct information regarding the complicated actions of cellulases on the plant cell walls in the hydrolytic process. A critical limitation is, of course, the unavailability of proper techniques that are able to characterize the real structure of the plant cell walls and the corresponding hydrolysis enzymes. Recently, more and more research is ongoing to concentrate on developing imaging techniques via combining both optical and non-optical microscopies to explicate the enzymatic degradation processes of the plant cell walls, especially at single molecule level.[97, 126-134]

For instance, Altaner and colleagues claimed in 2007 that the wood cell wall polysaccharides can be probed with monoclonal antibodies and CBMs.[135] Typically, CBMs of different families which differ in affinities for crystalline cellulose (CBM3a) and amorphous cellulose (CBM17 and CBM28) were shown to bind to the native wood cell walls with diverse strengths. This obvious differences in affinity of the CBMs highlighted a much stronger binding of the CBMs which can specifically bind to crystalline cellulose. In 2009, Igarashi's group carried out direct observations of *Tr*Cel7A molecules sliding on crystalline celluloses using AFM.[136] It was concluded that the movement is accompanied by a catalytic activity. This was demonstrated by the observation of CD having similar sliding speed to that of the wild-type, and also the immobility of the catalytically inactive enzyme mutant. CBM had no more active role in

cellulose hydrolysis except binding and increasing the enzyme molecule concentrations on the substrate.

CBMs have been verified by past work to function as reliable molecular probes for mapping the chemical property and structure of carbohydrate-containing materials due to their polysaccharide recognition capacity.[137-139] They have also been widely used for various fluorescence and electron labelings of the plant cell walls as well as for ultrastructural labeling of *Valonia* cellulose crystals, the results of which were proved to be particularly effective.[67, 140] However, most published descriptions of CBM probes require complex labeling procedures and the resolution of the images is not very satisfactory. Although the above studies exhibit some breakthroughs in characterization of cellulose-CBMs interaction, there is still little information on binding regularity, efficiency and kinetic mechanism of the interaction involving individual CBM molecule and crystalline cellulose. Moreover, the whole processes are all controlled by diffusion of a large amount of molecules, which is the only driving force in the experiments. Therefore, the binding process and mechanism of a single CBM molecule needs to be intensively studied via a more appropriate approach.

1.5 Dynamics and kinetics study of CBM binding to cellulose

1.5.1 Binding affinity studies

The binding affinity of CBM-cellulose interaction has been investigated extensively to study the binding mechanism of this process. Bulk experimental measurements are widely used to quantitatively determine a wide range of the affinity of different CBMs on different cellulose substrates base on competition isotherms and

fluorescent labeling.[141] The results of bulk experiments quantitatively showed a wide range of the affinity of different CBMs on the crystalline or amorphous cellulose substrates, with association constant K_a ranging from 10^5 M^{-1} to 10^7 M^{-1},[142-143] weaker than the K_a of antigen-antibody interactions which can be as high as 10^{12} M^{-1}. The reported data of these traditional methods are based on the measurements of the ensemble that contains a large amount of molecules mixed together and the obtained data is averaged by a statistical mechanism, which could lead to incomplete, even contradictory conclusions. In order to reconcile the above discrepancy, it is necessary to study the CBM-cellulose binding at single molecule level, which should reveal the more realistic reaction dynamic and kinetic mechanism.

Molecular modeling and simulation work has also been reported to mimic the dynamic process of the CBM-cellulose complex using *Trichoderma reesei* cellobiohydrolase I and parallel cellulose chains.[144-146] These results play a significant role in understanding the binding mechanism of cellulolytic enzymes to crystalline cellulose surface. By simulating the binding process of a single protein molecule, the results can provide essential information for real experiments at single molecule level. However, the results from simulation work can hardly be conclusive and need more experimental supports.

1.5.2 AFM recognition imaging and single molecule dynamic force spectroscopy

Molecular recognition between receptors and ligands plays a very important role in life sciences. Although numerous literature have reported the structure and function of receptor-ligand complexes, little data was shown about the molecular dynamics during the association and dissociation process with the traditional detection techniques. Besides,

probing the spatial distribution of individual binding sites on biological sample surfaces was difficult to achieve due to absence of appropriate imaging techniques.

In general, techniques such as chemical force microscopy[147] and force-volume mapping[148] are able to determine specific nature of the molecules, but cannot identify visual components simultaneously while imaging. Stroh and coworkers described an AFM Topography and RECognition (TREC) imaging technique in 2004, which succeeded in recognition of histone H_3 in a complex sample (chromatin) while simultaneously generating high-resolution topography images.[149] Using this technique, a probe molecule is tethered to the AFM tip via a crosslinker in a few nanometers' length (providing enough freedom for the molecule). The highly specific recognition reaction between the probe molecule and sample molecules immobilized on the substrate surface can be investigated to successfully identify the specific target molecules. The principle of AFM recognition images is illustrated in Figure 1.5.[150] This efficient, reproducible, and specific recognition technique significantly extends the capability of AFM.[151-171]

In principle, when the probe molecule on AFM tip interacts with the specific molecules on substrate, the crosslinker in-between will be stretched in the retraction process of the AFM cantilever (Figure 1.5(a)). The top peak of the oscillations is reduced due to this energy loss and the specific interactions can be detected by generating a corresponding recognition signal. This process is followed by a further analysis in PicoTREC controller, which can split the raw deflection signal of the cantilever into the upper (U_{max}, marked in black) and lower (U_{min}, marked in yellow) parts (Figure 1.5(b)). These two parts of each circle are then recorded as the recognition and topography signals, respectively (Figure 1.5(c)).[172] The dark recognition patches clearly coincide

with the position of target molecules (the yellow, round spots) in the topography image; meanwhile, the molecule on the substrate which doesn't have specific interactions with the functionalized AFM tip will not generate recognition signal (Figure 1.5(c)). The method is based on detecting a small shift in the peak value of the cantilever deflection signal that occurs when a tip-tethered molecule binds to a target on the surface, bridging the gap between the surface and an oscillating tip.[149] This recognition process has been widely used due to its great potential in molecular imaging of surfaces, while such measurements are tedious and subject to errors, therefore great caution should be taken during sample preparation, data acquisition and interpretation.[149, 173]

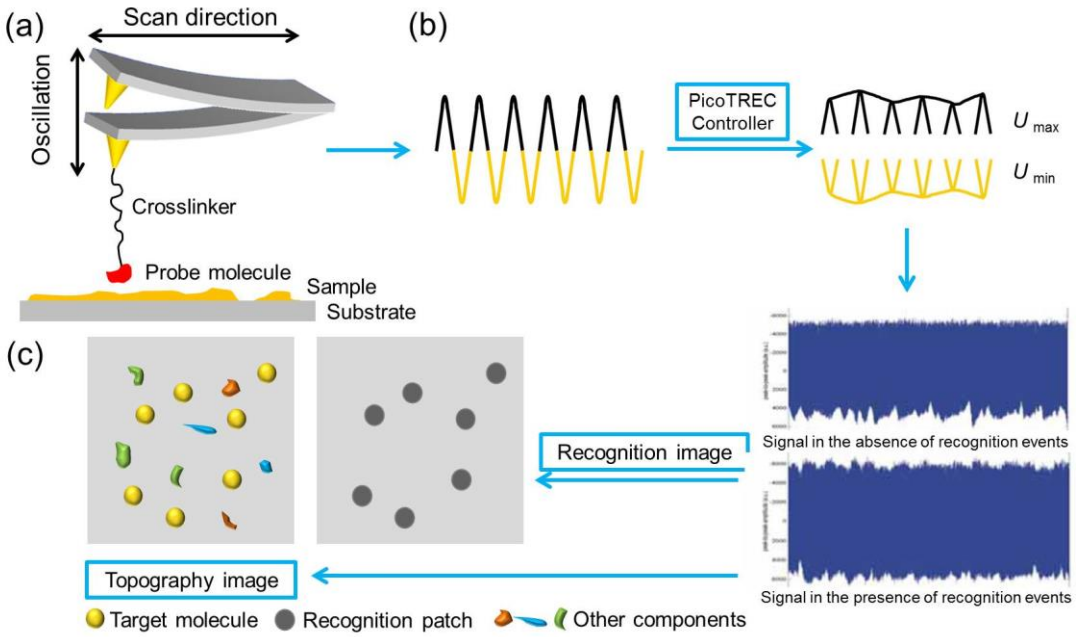

Figure 1.5 Principle of AFM topography and recognition imaging (TREC) imaging. (a) AFM tip functionalized by a probe molecule is scanning on the sample surface; (b) the signal generated by cantilever oscillation is split into lower and upper parts through PicoTREC controller, resulting in simultaneously acquired topography and recognition images (c). The recognition events of the yellow, round target molecules are shown as dark spots in recognition image. ©2005 NSTI http://nsti.org. Reprinted and revised, with permission.[150]

In a similar way, the interactions between crystalline cellulose and CBM molecules are also feasible by AFM recognition imaging technique with proper tip and substrate modification procedures.[174] Therefore, the carbohydrate components of the plant cell walls can be characterized more precisely at single molecule level. The information provided by this method will also guide the kinetics study of single CBM molecule binding to cellulose.

1.5.3 Theories in kinetics and thermodynamics study

AFM based single-molecule dynamic force spectroscopy (SMDFS) allows measurement of forces in pico-newton (10^{-12} N) scale among single molecules, therefore can provide fundamental insights into a wide range of biological phenomena and properties on single molecule basis, such as molecular recognition, protein folding/unfolding and DNA mechanics.[174,175-176] During force measurement, when the modified AFM tip is approaching the sample surface, the tip applies a constant force on the surface leading to the cantilever deflection and a flat baseline can be observed along the tip displacement distance. The repulsive force generated in-between due to the close distance can push the curve upward until the force setpoint is reached. Then the curve drops back to the baseline until an attractive force hampers tip retraction and generates a peak below the baseline. Finally, the tip withdraws from sample surface and the force becomes zero abruptly, resulting in a flat baseline again after the peak. Numerous such force-distance (F-D) curves can be recorded during this process for building a histogram and determining the most probable unbinding force of the CBM-cellulose interaction. Based on Bell's model[177] and Jarzynski's equality,[178] the F-D curves and unbinding forces can be used to determine the dynamic and kinetic parameters such as undbing

forces, dissociation rate constant, off rate (or k_{off}), energy barrier length (x_β), the free energy changes (ΔG), and so forth.

Bell claimed in 1978 that bond breaking is a statistical process. The lifetime of a bond is closely related to the mechanical load.[177] Bell's model can be briefly introduced as follows:

The unbinding force F^* is calculated from the equation based on Bell's model,

$$F^* = \frac{k_B T}{x_D} \ln r - \frac{k_B T}{x_D} \ln(k_{off} \frac{k_B T}{x_D}) \qquad \text{Equation 1.1}$$

Here, F^* is the unbinding force (pN) determined from a histogram built from several F-D curves; k_B is Boltzmann's constant ($1.3806505 \times 10^{-23}$ J K^{-1}); T is the effective temperature (300 K); x_D is the energy barrier length (nm), larger than which the bond will break; r: loading rate (nN s^{-1}); k_{off} is dissociation rate or off rate (s^{-1}).

According to Bell's model, the reaction dissociation rate or k_{off} can be determined by plotting unbinding forces under a series of loading rates. The larger the k_{off}, the lower the affinity is. But here, the force spectroscopy reflected only the non-equilibrium state of the interaction under a certain loading rate. It has proved that the equilibrium free energy change can be reconstructed using Jarzynski's equality by averaging the external work and calculating the integral.

In 1997, an equality for obtaining the equilibrium free energy difference from the irreversible work was derived by Jarzynski.[178] Some applications and extended studies showed that Jarzynski's equality is more reliable when applied in the non-equilibrium regime. The Jarzynski's equality is expressed briefly below:

$$e^{-\Delta F / kT} = \overline{e^{-W / kT}} \qquad \text{Equation 1.2}$$

Here, T is the effective temperature (300 K) and k is Boltzmann's constant ($1.3806505 \times 10^{-23} J\ K^{-1}$). The over-line presents an average over all possible instances of an external process. The system is transferred from one equilibrium state in this process to a non-equilibrium state under the same external conditions as that of the other equilibrium state. Using Jarzynski's equality, the free energy changes can be reconstructed by being related between two equilibrium states and non-equilibrium processes. Therefore, we are able to rebuild the free energy profiles of CBM-cellulose interactions using the data determined under non-equilibrium states.

1.6 Objectives and organization of this dissertation

1.6.1 Objectives of this dissertation

The objective of this research is to understand the binding mechanism of CBM-cellulose interactions at single molecule level. Both AFM topography and recognition imaging and AFM based SMDFS were applied in the following studies.

Based on the above discussion, the current methods for studying the binding kinetics of CBM-cellulose interactions can hardly meet the requirements of high resolution imaging and determination of binding affinity at single molecule level at the same time. Without a profound understanding of how a single CBM molecule plays the important role in biomass degradation, the cellulolytic enzymes are not able to take effect very efficiently and economically to overcome the biomass recalcitrance and the biofuel production is still greatly hampered.

Therefore, a specific methodology needs to be developed to investigate the CBM binding sites on the cellulose, especially crystalline cellulose, and quantitatively

determine the kinetic parameters based on a single CBM molecule. The information of structural and composition changes of the cell wall surface after pretreatment can facilitate the cell wall degradation by providing new information for efficient pretreatment. To achieve these goals, a series of experiments have been designed to investigate the binding specificity of type A CBMs which bind specifically to crystalline cellulose to plant cell wall cellulose, to determine the binding affinity and kinetic parameters of the CBM-cellulose interactions, and also to reveal the structural changes of plant cell wall surfaces before and after pretreatment.

1.6.2 Organization of this dissertation

In the following chapters, several carefully designed experiments will be introduced on plant cell wall recognition imaging and kinetics study of CBM binding to crystalline cellulose at single molecule level. In chapter 2, *in situ* AFM imaging was applied to observe the binding specificity of CBM3a to plant cell wall cellulose. In chapter 3, the binding kinetics were determined by SMDFS between CBM3a/CBM2a and crystalline cellulose, which presented a different conclusion from the statistic results obtained in bulk experiment reflecting the binding behavior of many molecules. In chapter 4, the plant cell wall surfaces were mapped by AFM recognition imaging to reflect the surface morphology and component changes before and after acid pretreatment. These changes could essentially affect the surface accessibility of cell walls for enzymes in the early stage of enzymatic hydrolytic process. In chapter 5, a minimal effective initial concentration and comparatively short reaction time were determined for CBM3a binding to crystalline cellulose, which provided the information of a more efficient binding process. The last chapter lays out the summary and outlook of the overall studies.

CHAPTER 2

SINGLE MOLECULAR BINDING SPECIFICITY OF A CARBOHYDRATE-BINDING MODULE TO NATURAL PLANT CELL WALL CELLULOSE

2.1 Introduction

It has long been a great challenge to improve the efficiency of enzymatic hydrolysis, as little is known microcosmically about the detailed structure of the plant cell walls and interaction of enzymes with the embedded polysaccharides.[11, 42] Therefore, a more profound understanding of cellulose-enzyme interactivion mechanism down to single molecule level is crucial to the enzymatic conversion of the biomass into fermentable sugars, thus ultimately optimizing production of bioethanol.[179]

As the beginning and key step in the hydrolysis process, the interactions between the plant cell wall carbohydrates and a group of unit contiguous amino acid sequences - carbohydrate-binding modules (CBMs) in cellulolytic enzymes need to be understood.[43] The main function of CBMs is to recognize the target carbohydrate substrate and then convey their catalytic segments to the substrate surface for effective hydrolysis.[14] Cellulose-specific CBMs are classified into three types based on experimentally verified structural and functional similarities, binding to specific surfaces of insoluble crystalline cellulose/chitin (type A), individual $\beta(1\rightarrow4)$ glucan chains (type B) and small sugars (type C).[43] One of the type A CBMs, CBM3a, a family 3 CBM from the cellulosomal scaffoldin subunit CipA of *Clostridium thermocellum*, has both theoretically and experimentally proved to bind specifically to crystalline cellulose.[68, 180]

In this work, we studied the *in-situ* binding activity of CBM3a to the poplar cell wall cellulose using CBM3a-functionalized gold nanoparticles (GNPs). The whole procedure was monitored by AFM recognition imaging using the CBM3a-functionalized AFM tip to map out the binding events across the plant cell wall surface samples.[174] All the experiments were performed on untreated, microtomed poplar stem sections. To quantify the binding affinity, we also measured the rupture forces between cellulose and CBM3a using AFM based single molecule dynamic force spectroscopy (SMDFS). The results of this study offered a direct, real-time and quantitative observation of the binding activities between CBM3a and plant cell wall cellulose at single molecule level.[181]

2.2 Experiments

2.2.1 Preparation of Recombinant CBM3a

The sequence encoding CBM3a was amplified by polymerase chain reaction (PCR), using primer pair, CBM3aF (5'CTCTCCATGGGCGTATCAGGCAATTTGAA-GGTTG) and primer CBM3aR (5'CTCTCTCGAGACCGGGTTCTTTACCCCATAC-AAG), from the genomic DNA of *Clostridium thermocellum* strain ATCC 27405 (GeneBank accession No. CP00568; Nucleotide No. 3620608-3621084). The amplified product was separated by 1% agarose gel electrophoresis. The 491-bp DNA band was excised and purified using the QIAquick Gel Extraction Kit (Cat. No. 28704; Qiagen Sciences, Maryland, USA). The purified DNA was digested by restriction enzyme Nco I and Xho I, then inserted into Nco I & Xho I-cleaved expression vector pET28b [product of Novagen, now a part of Merck Life Science Research; the vector info is available online at http://www.merck-chemicals.com/life-science-research/vector-table-novagen-

pet-vector-table/c_HdSb.s1O77QAAAEhPqsLdcab]. The resulting plasmid, pCBM3a, was verified by DNA sequencing for accuracy.

The translated amino acid sequence of the recombinant CBM3a is:

MGVSGNLKVEFYNSNPSDTTNSINPQFKVTNTGSSAIDLSKLTLRYYYTVDGQKD QTFWCDHAAIIGSNGSYNGITSNVKGTFVKMSSSTNNADTYLEISFTGGTLEPGA HVQIQGRFAKNDWSNYTQSNDYSFKSASQFVEWDQVTAYLNGVLVWGKEPGLE HHHHHH.

It includes a $(His)_6$ tag with a predicted molecular weight of 18770 and a pI of 6.51.

The plasmid was then transformed into *Escherichia coli* host strain Tuner (DE3) {*F*⁻ *ompT hsdS*$_B$ (r_B^- m_B^-) *gal dcm lacY1 λ(DE3 [lacI lacUV5-T7gene 1 ind1 sam7 nin5])*}. A colony transformant was grown at 37 ˚C in 1 L Luria broth media supplemented with 50 μg/mL of kanamycin as the selection drug until the culture reached a density of 0.5 OD at 600 nm. Induction was performed at 16 ˚C for 10 h in the presence of 0.2 mM isopropyl β-D-1-thiogalactopyranoside (IPTG) as the inducer. After induction, cells pelleted from the culture were re-suspended in 20 ml of a binding buffer (IBB = 25 mM Tris-Cl, pH 8.0, and 300 mM NaCl) and completely disrupted by sonication. Cell debris was removed by centrifugation at 25,000 ***g*** for 20 min at 4 ˚C. The supernatant was further cleaned up by filtration through a 0.45-μm Acrodisc Supor membrane disc attached to a 30-mL syringe.

Soluble recombinant CBM3a in the cell lysate was purified by Immobilized Metal Affinity Chromatography (IMAC) as following:

The clear supernatant was applied to a column containing 2 mL bed volume of TALON™ metal-affinity resin (Clontech product, Mountain View, CA). The column was washed with 10 vol. of IBB, followed by successive washes of 5 vol. of IBB-5mM

imidazole and IBB-10 mM imidazole, respectively. Pure CBM3a was eluted in 5 mL of IBB-100 mM imidazole, and dialyzed three times against 1 L of Tris buffer (10 mM Tris-Cl, pH 7.5, 150 mM NaCl). The final protein sample, about 5 mL at a concentration of 20 mg/mL (1.1 mM) was stored in 0.5-mL aliquots at -20°C.

2.2.2 Poplar Sample Preparations for GNP-CBM3a Binding Observation and AFM Recognition Imaging

Fresh stems of poplar plant (*Populus alba*) was collected from the University of Georgia campus. Stem sections of 50 μm thickness were prepared by microtome in the Electron Microscopy Lab (Department of Plant Biology, the University of Georgia). The poplar sections were placed between two clean glass slides at ambient temperature to prevent distortion.[95] Before scanning, the sample was immobilized on a glass slide with a trace amount of epoxy glue and then air-dried. The sample was fixed onto an AFM flow cell,[172] which was then filled with 0.3 mL of Tris buffer (10 mM Tris-Cl, pH 7.5, and 150 mM NaCl) for GNP-CBM3a binding observation and AFM recognition imaging.

2.2.3 Gold Nanoparticle Functionalization

The GNPs (6 nm, 1 mL, from Nanopartz Inc.) was incubated with the Dithiobis-(nitriloacetic acid butylamidylpropionate) (DTSP-ANTA) (shown as NTA for short hereafter) crosslinker (2 mg/mL, 0.25 mL). The synthesis procedure of NTA crosslinker is described below (Scheme 2.1).

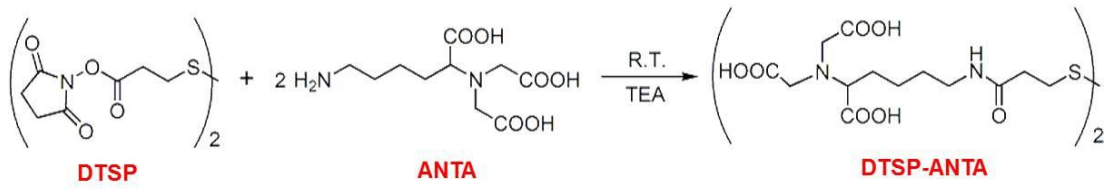

Scheme 2.1 Synthesis procedure of DTSP-ANTA crosslinker

The NTA crosslinker used to functionalize the GNPs are synthesized as follows: N-5-(amino-1-carboxypentyl) iminodiacetic acid (ANTA) (78.4 mg, 0.3 mM) was dissolved in water (1 mL). Dithiobis(N-succinimidyl propionate) (DTSP) (40.3 mg, 0.1 mM) was dissolved in dimethylformamide (DMF) (1 mL) and then added into ANTA/water solution drop by drop. Further triethylamine (TEA) (80 μl, 0.4 mM,) was added into the mixture. The reaction proceeded overnight at room temperature and then the solvent was evaporated and the residue was purified by HPLC (water: acetonitrile). Yield was 70%. ^{1}H NMR (CD_3OD, 300 MHz), δ 2.59 (t, 4H), 2.94 (t, 4H), 3.20 (t, 4H), 3.57(t, 2H). ^{13}C NMR (CD_3OD): δ 173.97, 172.57, 65.66, 54.09, 38.89, 35.36, 34.00, 29.11, 28.72, 23.53. MALDI-TOF (699.14, 721.12, 743.12).[182]

After 2-3 h incubation, the product was mixed with $NiCl_2$ solution (50 mM, 15 μL) for 30 min. The modified GNPs suspension was centrifuged for 15 min at 13,000 ***g*** in a microcentrifuge (SORVALL BioFuge Pico Microcentrifuge, Thermo Electron Corporation, Marietta, Ohio) and then washed 3 times with the Tris buffer. Finally, the GNPs were incubated in CBM3a-$(His)_6$ solution (20 μg/mL, 10 μL) with addition of 1 mL of Tris buffer. Before use, the GNP-CBM3a complexes were centrifuged again to remove excessive CBM3a and the precipitation was re-dispersed in 1 mL of Tris buffer for future imaging. The UV-vis absorbance measurements were carried out at room

temperature (UV-1700 PharmaSpec UV-VIS Spectrophotometer, Shimadzu Scientific Instruments, Inc.).

2.2.4 AFM Experimental Settings

The PicoPlus Molecular Imaging system together with a PicoScan 3000 Controller was used in this work. An Agilent multipurpose AFM scanner was used for scanning within an area size of 10 μm^2. All the images were taken using Top Magnetic AC (TopMAC) mode under PicoTREC (Agilent Technologies, Santa Clara, CA) with CS-10 silicon AFM tips (Nanoscience Instruments, nominal spring constant of 0.1 N/m). The whole system was enclosed by a PicoPlus Isolation Chamber for shielding from environmental interference. After obtaining several high resolution images on a small area of the poplar sample surface, the scanning was stopped and 0.2 mL of GNP-CBM3a suspension was gently injected into the flow cell. The scanning was then restarted to monitor the whole binding process in the following 7 h.

2.3 Results and discussions

2.3.1 Functionalization of gold nanoparticles and AFM tip by CBM3a

In order to follow the binding events of small CBM3a molecule (in size of 3 nm × 3 nm × 4.5 nm)[68] to the rough plant cell wall surface, we monitored the 6-nm GNP-CBM3a complexes anchoring on the sample by high-resolution *in-situ* AFM imaging. The GNPs were first functionalized by the synthesized crosslinker (Scheme 2.1) via the S-Au bonding.[183] The recombinant CBM3a-$(His)_6$ molecules were then attached onto the crosslinker-modified GNP surface following the procedure described in Figure 2.1.

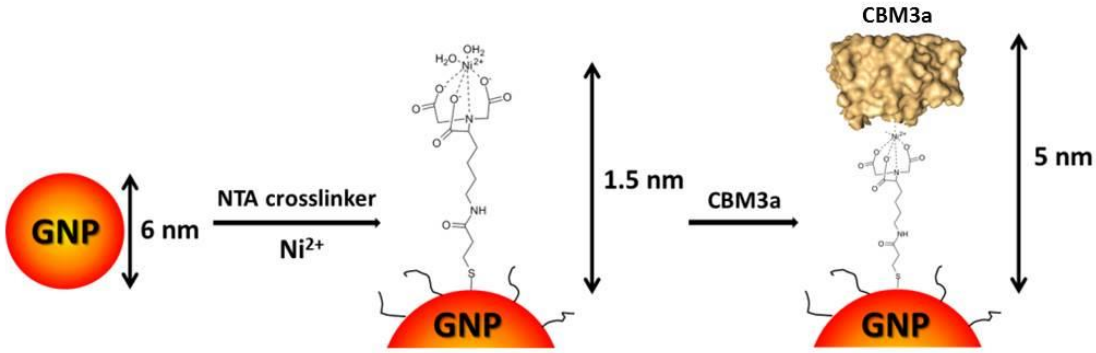

Figure 2.1 Schematics of GNP functionalization. The CBM3a model is generated by molecular visualization software PyMOL (version 0.99rc6)). The GNP, Ni-crosslinker, and CBM3a molecule (Protein Data Bank (PDB) code: 1NBC) are not drawn to scale.

The bottom-left inset in Figure 2.2 shows the color change before and after GNP functionalization. The color of the pure 6 nm GNPs suspension was originally dark red (left panel) and gradually changed into light purplish after NTA-crosslinker and CBM3a functionalization (right panel). The color change suggested the shift of the surface plasmon resonance (SPR) peaks of the GNPs at each surface reaction stage, but only this information could not reveal the whole morphological condition of the modified GNPs. Therefore, to make sure that our modification was successful without any severe aggregation, we measured the UV-Vis absorbance properties of the GNPs after each reaction step.

As shown in Figure 2.2, the characteristic absorption peak of pure 6 nm GNP appears at 516 nm before functionalization (black curve in the box). After the addition of NTA crosslinker and Ni^{2+} solution, the absorption peak shifts to 518 nm (red curve), showing an increase of the diameter of GNPs due to the formation of Ni-NTA monolayer on the surface of GNPs via Au-S bonding. When CBM3a-$(His)_6$ was mixed with the

GNP-crosslinker complexes, the absorption peak became slightly wider and shifted to 523 nm (blue curve), indicating a further coverage of the CBM-Ni-NTA monolayer. Though several factors can cause the shift of SPR peaks (e.g., size, shape and local environment),[184] it is obvious in this case that the spontaneous S-Au and Ni-histidine tag interactions primarily caused the changes in particle size and hence, the color. Therefore, the UV-Vis absorbance spectra demonstrated the successful morphological alterations of the GNPs before and after modification by CBM3a-Ni-NTA molecules.

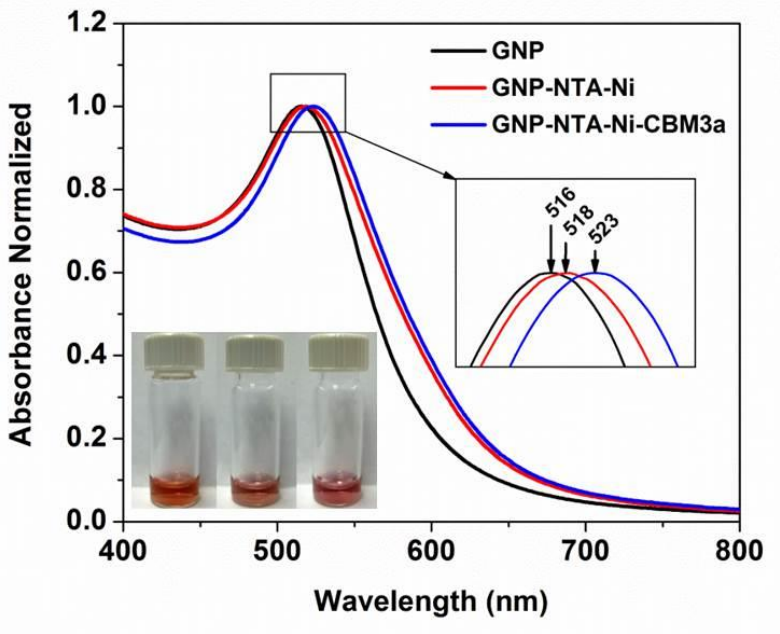

Figure 2.2 CBM3a-functionalized GNP characterization by UV-Vis spectrophotometer. Bottom-left inset: color change from pure GNPs to the CBM3a-functionalized GNPs. The peak shifts are highlighted in the black box: characteristic UV-Vis absorbance peaks of pure 6 nm GNPs at 516 nm, Ni-NTA-crosslinker bound GNPs at 518 nm and CBM3a-GNP complexes at 523 nm.

A similar method was also applied for AFM tip functionalization in the following studies. The AFM tip was first coated with a magnetic material followed by a layer of gold. The gold surface of the tip was then modified with thiol-PEG_{2000}-NTA-Ni crosslinker and CBM3a molecules, using a procedure similar to the GNP modification (Figure 2.3). Unlike the GNP functionalization, a longer and more flexible polyethylene glycol (PEG_{2000}) was used here as the major portion of crosslinker for minimizing the mis-orientation and steric hindrance during scanning.[185]

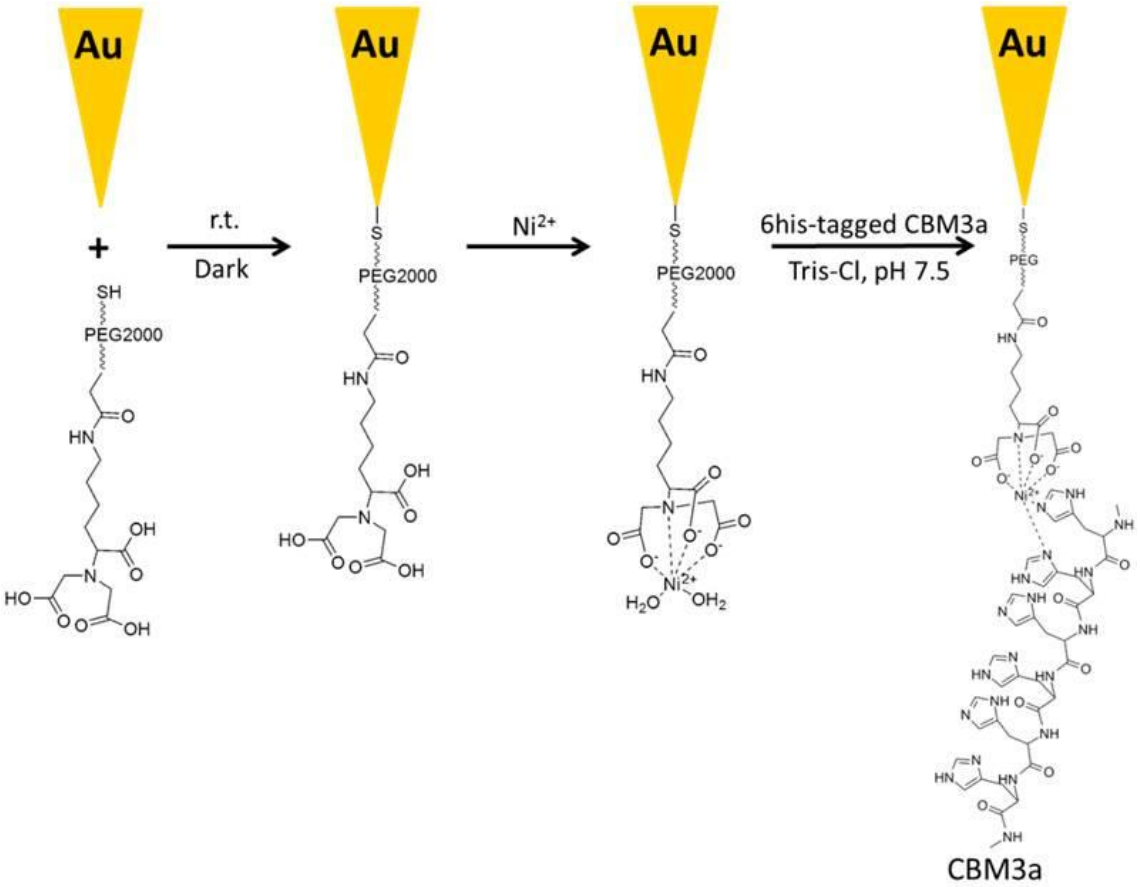

Figure 2.3 Schematics of AFM tip modified with a CBM3a molecule. The NTA crosslinker is immobilized on the AFM tip via thiol end. The AFM tip, crosslinker and CBM3a are not to scale.

Briefly, the CS-10 silicon AFM tips (Nanoscience Instruments, nominal spring constant of 0.1N/m) were first coated with a magnetic material and a layer of gold using an ion-beam evaporator.[185] As shown in Figure 2.3, the freshly coated tips were then immersed in HS-PEG_{2000}-NTA crosslinker (Nanocs Inc.) (0.2 mg/mL, 300 μL) for 3 h and in $NiCl_2$ (10 mM, 20 μL) for 30 min at room temperature. The tips were then washed repeatedly and immersed in 300 μl Tris buffer (10 mM Tris-Cl, pH 7.5, and 150 mM NaCl) with addition of CBM3a (16 μg/ml, 10 μL). The solution was kept at 4 ˚C for 8 h. The modified tips were finally washed thoroughly in Tris buffer for future imaging. The gold-NTA-Ni-$(His)_6$-tagged protein is a widely used chelating complex due to its specificity, affinity and remarkable stability in the environment of high salt, wide pH range and various solvents.[183]

2.3.2 In-situ imaging of CBM3a-GNP binding to natural plant cell wall

To observe the binding process of the GNP-CBM3a complexes to the cellulose, we first used a bare AFM tip to find a target area on the poplar sample surface with representative features (i.e. clear crystalline cellulose microfibrils in a parallel arrangement) and then stopped scanning. After the injection of GNP-CBM3a suspension into the flow cell, the scanning was restarted and the whole binding process was continuously monitored *in situ* for 7 h in the same selected scanning area. Figure 2.4 shows the snapshots of AFM topography and amplitude images of the GNP-CBM3a complexes binding on the sample surface at time 0 min (Figure 2.4(a, e)), 70 min (Figure 2.4(b, f)), 327 min (Figure 2.4(c, g)), and 395 min (Figure 2.4(d, h)). At the very beginning, the parallel cellulose microfibrils with a diameter of 10-20 nm were clearly observed on the sample surface. The irregular dots in various sizes embedded among the

microfibrils are most likely other natural polymers or membrane debris in the plant cell walls.[16] With the GNP-CBM3a complexes gradually bound to the cellulose, more and more round spots in diameter of 30-40 nm appeared on the cellulose surface. Beginning at 70 min the GNP-CBM3a complexes were found to align with each other to form a parallel structure and finally cover about 70-80% surface area of the sample at 395 min. After about 400 min, the morphology of the sample surface no longer showed much difference, suggesting that the binding of the GNP-CBM3a complexes onto the cellulose was saturated. The selected area in the red square highlights clearly how the morphology changes during the whole binding process.

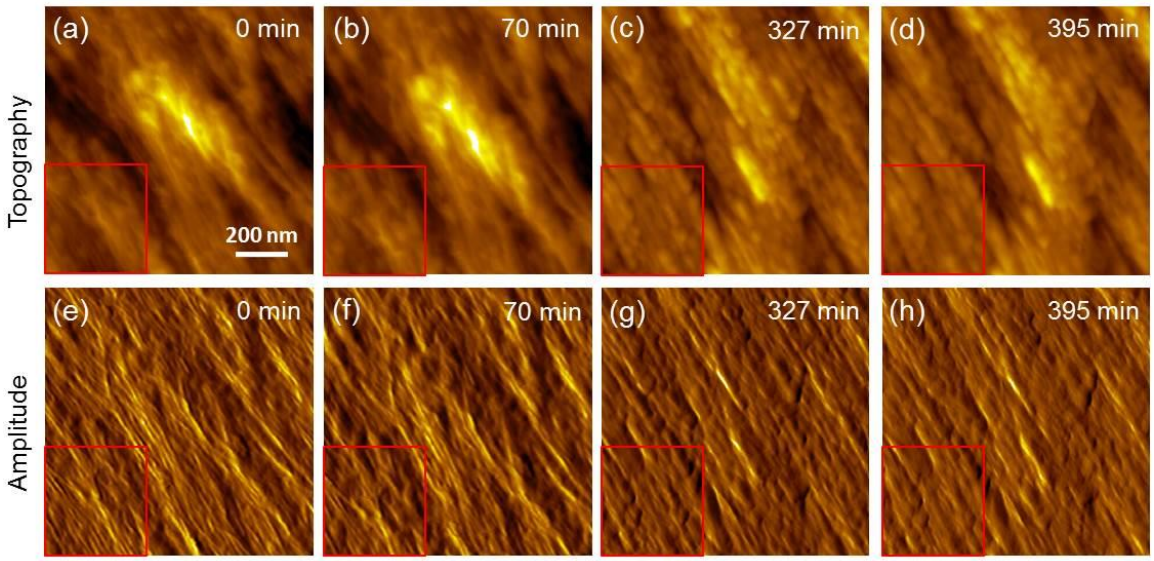

Figure 2.4 *In-situ* real-time AFM imaging of GNP-CBM3a complexes binding on the natural poplar cell wall surface. In the beginning, the cellulose microfibrils in diameter of 10-20 nm are clearly observed on the sample surface in a well-paralleled arrangement. After injection, spots in diameter of 30-40 nm gradually appeared on the cellulose surface and eventually covered about 70-80% surface area of the sample. The area in red square highlights the morphology alteration during the imaging period.

The actual size of a single GNP-CBM3a complex is around 16 nm in diameter (estimated from Figure 2.1), while the apparent size shown in the AFM images is 30-40 nm (Figure 2.4(c) and Figure 2.5) due to the tip broadening effect and compression of molecules caused by the force applied.[93] As shown in Figure 2.5, the average diameter of 100 GNP-CBM3a complexes was determined to be 38.85 nm, which corresponded very well to the observation on natural plant cell walls.

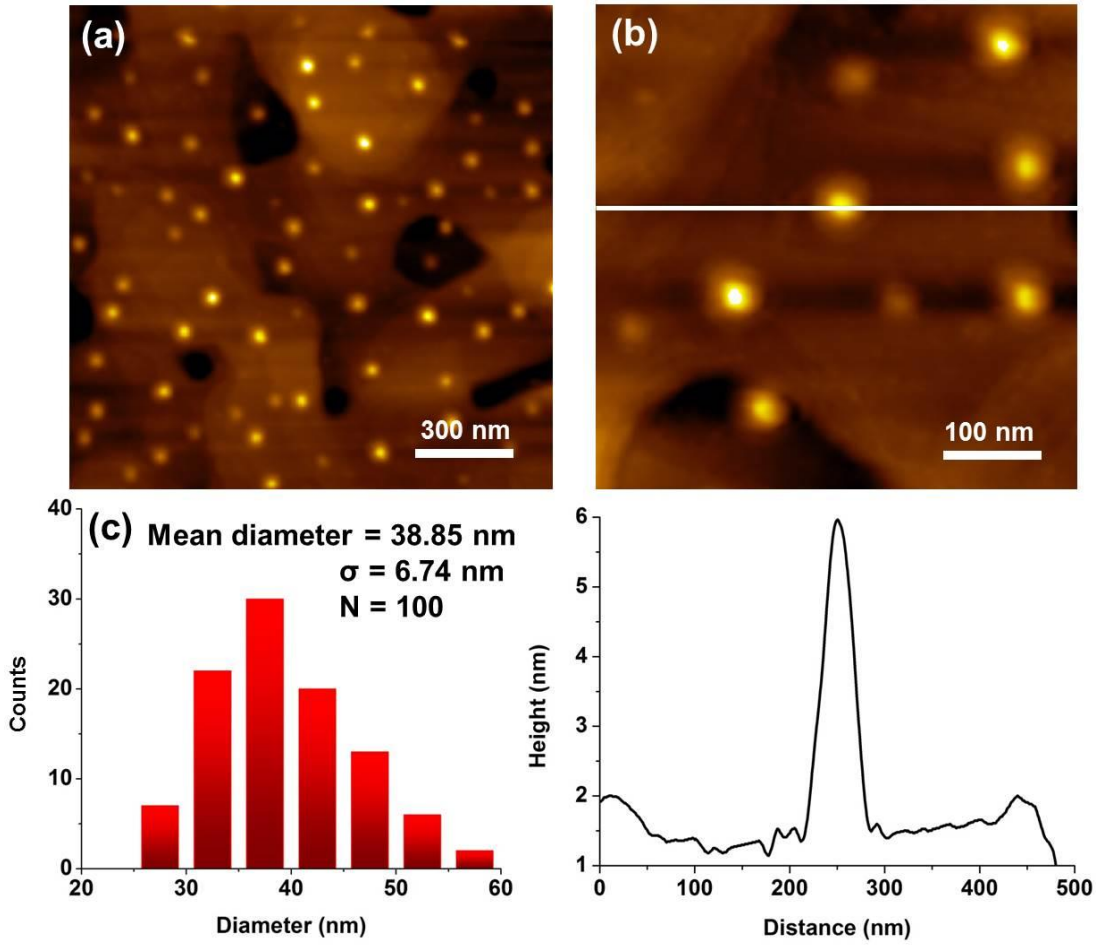

Figure 2.5 GNP-CBM3a complex sizes measured by bare AFM tip on flat Au (111) surface. (a) Topography image; (b) topography image on a smaller area and the corresponding cross-section analysis of one GNP-CBM3a complex; (c) Size distribution of 100 measured complexes.

In a previous study, (CdSe)ZnS quantum dots directed by CBM3a were used to achieve direct labeling of the planar face on an isolated single crystalline cellulose.[186] Electron microscopy results showed that these quantum dots directed by CBM3a probes aligned precisely in a linear sequence along the hydrophobic planar face of cellulose. In our observation on natural plant cell walls, the GNP-guided CBM3a still bound to crystalline cellulose microfibrils in a linear arrangement along the microfibril axis, although the specific planar face of crystalline cellulose was not seen clearly in the images due to the complexity of the natural plant cell wall structure. Nevertheless, our results directly demonstrated that CBM3a was able to bind to and densely align along the natural, parallel crystalline cellulose very fast.

To confirm that this layout was due to the specific binding between CBM3a and cellulose instead of non-specific interaction such as physical deposition, we conducted some control experiments with pure GNPs and non-crystalline cellulose surface.

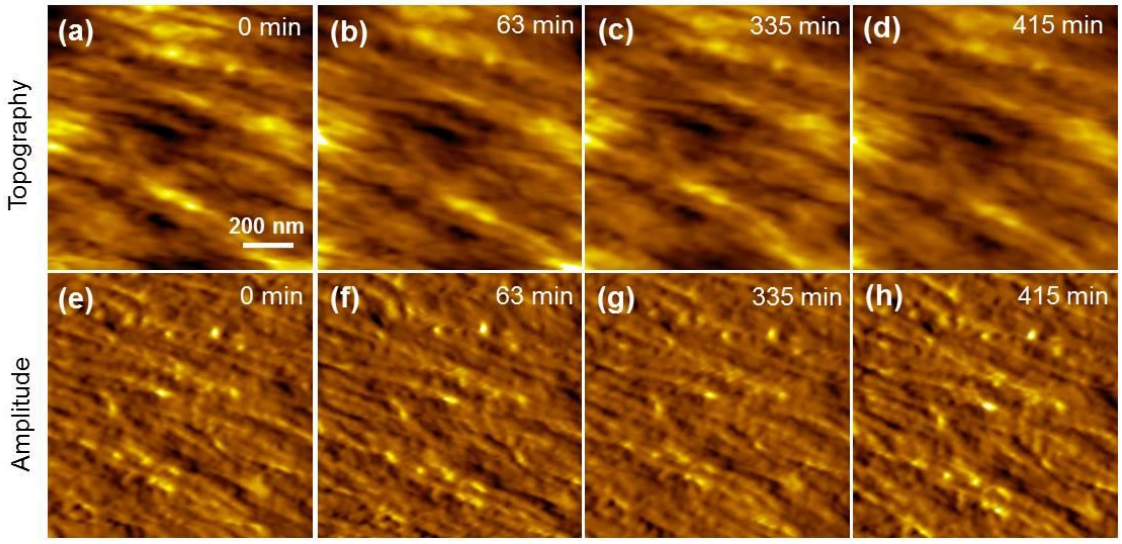

Figure 2.6 *In-situ* real-time AFM imaging of crystalline cellulose on natural poplar cell wall surface after injection of pure 6 nm GNPs. No specific binding process was observed.

In the control experiments on crystalline cellulose with pure, un-modified GNPs (Figure 2.6), no obvious specific binding was observed under the same experimental conditions. After pure GNPs (0.2 mL, 6 nm) were gently injected into the flow cell, the same area was imaged continuously for the following 1 h. No obvious bound GNPs were observed on the cellulose surface, indicating the lack of specific interactions between pure GNPs and cellulose surface.

We also observed the binding of GNP-CBM3a complexes to non-crystalline cellulose surface in another control experiment as shown in Figure 2.7. During the following 7 hours after injection of 0.2 mL GNP-CBM3a complexes buffer solution, no obvious bound GNP-CBM3a complexes were observed on the sample surface. Therefore, we concluded that GNP-CBM3a complexes could only bind specifically with crystalline cellulose.

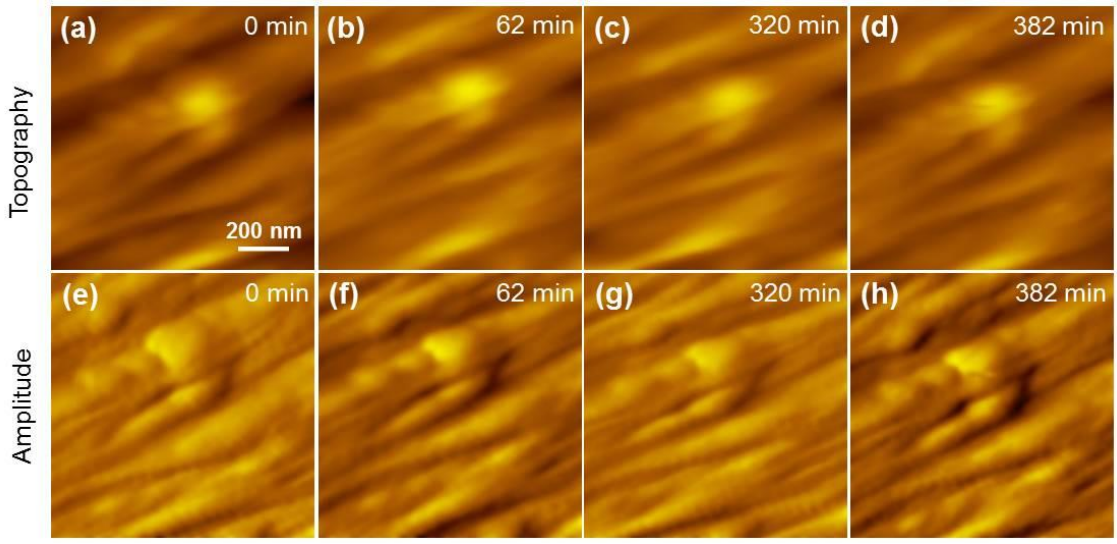

Figure 2.7 *In-situ* real-time AFM imaging of non-crystalline cellulose surface on natural poplar cell walls after injection of GNP-CBM3a complex solution. No specific binding process was observed.

In the next step, we selected the images at 0 and 395 min from Figure 2.4 to compare the binding details. Figure 2.8 depicts the representative area generated from the red square in Figure 2.4, exhibiting the detailed changes of morphology. Figure 2.8(c, d) are the height analysis generated from the white lines (a-a’ in (a) and b-b’ in (b) showing the morphological changes before (Figure 2.8(a)) and after binding (Figure 2.8(b)). Before binding, the image shows clear crystalline cellulose microfibril structure (Figure 2.8(a)) with the diameter of 10-20 nm (Figure 2.8(c)). After the binding of GNP-CBM3a, the cellulose microfibril structure gradually disappeared and the topography showed close alignment of GNP-CBM3a (Figure 2.8(b)) all over the sample surface with a larger size of 30-40 nm (Figure 2.8(d)).

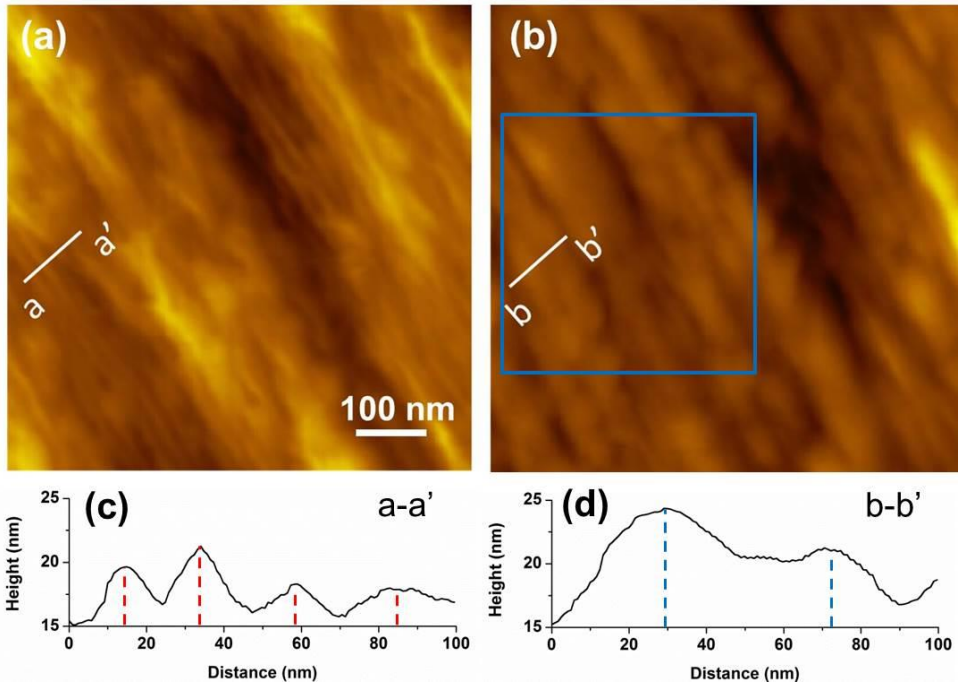

Figure 2.8 Morphology of the cell wall surface before and after GNP-CBM3a binding. (a) Before binding (0 min); (b) after binding (395 min); (c) cross-section profile of the white line a-a′; (d) cross-section profile of the white line b-b′. The center of the cellulose microfibrils and bound GNP-CBM3a complexes are marked by dashed red and dashed blue lines, respectively in (c) and (d).

A representative alignment of the particles is marked in the blue square in Figure 2.8(b) and highlighted in 3D image and schematic as shown in Figure 2.9(a). The locations of the GNP-CBM3a complexes on the cellulose surface were partially highlighted at the top by dashed, black circles. The inset of Figure 2.9(a) shows the cross-section generated from the two adjacent complexes labeled by double-headed arrow representing the distance, "D", between the centers of the two complexes. "D" was measured to be around 50 nm and the separation space between the opposite edges of two bound complexes is about 20-30 nm. This separation measured is larger than the reported average separation distances between two quantum dots binding to individual CBM3a molecules that already bond along a single crystalline cellulose.[186]

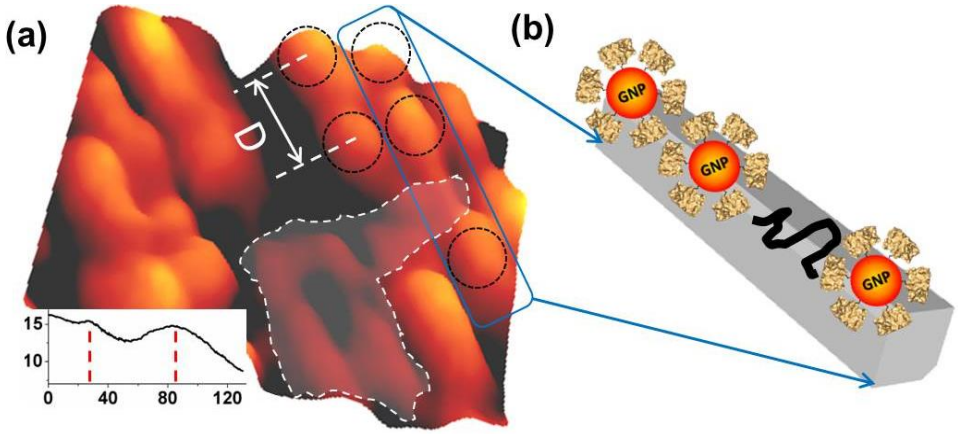

Figure 2.9 3D image and schematic of GNP-CBM3a binding to crystalline cellulose. (a) Highlighted 3D image of representative alignment of the complexes (inset: cross-section profile of two adjacent GNP-CBM3a complexes labeled by double-headed arrow from the center). GNP-CBM3a complexes bound on the cellulose surface were partially highlighted by black dashed circles. The dashed white lines in (a) highlight the center of two adjacent complexes and the distance in-between marked by letter "D" is about 50 nm, indicating the space between the edges of two bound particles is 20-30 nm. The cellulose microfibrils unbound are marked by the light grey area within the dashed white circle. (b) Schematics of the alignment of GNP-CBM3a complexes on the hydrophobic facet of a single cellulose microfibril marked in blue solid rectangle in (a).

One possible reason is that the GNP-CBM3a complexes are larger in size than a single CBM3a molecule, thus separating apart at a larger space when binding along the cellulose microfibrils due to steric hindrance during targeting. In addition, some areas on the sample surface were inevitably covered by other non-cellulose components (invisible here) due to the impurity of the natural plant cell walls, making it impossible for the CBMs to bind and thereby enlarging the space between the bound complexes. One example of the cellulose surface without any CBM3a binding is shown in Figure 2.9(a) (the light grey area in white dashed circle). The alignment of GNP-CBM3a complexes on the hydrophobic cellulose surface is marked by a blue solid rectangle and highlighted in the schematic in Figure 2.9(b), illustrating the distribution of GNP-CBM3a complexes on single crystalline cellulose.

2.3.3 Study of specific CBM-cellulose interaction by AFM recognition imaging and single molecule dynamic force spectroscopy

To clearly demonstrate that GNP-CBM3a specifically bound to crystalline cellulose, further experiments on binding specificity and affinity need to be carried out. In the next step, we studied the direct binding of CBM3a to crystalline cellulose on natural plant cell walls using AFM topography and recognition (TREC) imaging and SMDFS with a CBM3a-functionalized AFM tip.

The crystalline cellulose distributions on natural and pretreated plant cell wall surfaces can be specifically characterized by the well-established recognition imaging technique (Figure 1.5). This technique has been widely used in molecular imaging of bio-surfaces, but great caution should be taken to avoid errors and inaccurate data during sample preparation and data analysis.[149, 173] For example, proper concentrations of CBM

are critical to ensure single or just a few CBM molecules be modified on the AFM tip to avoid multi-molecular interactions.

It has been established that at least three aromatic residues on a CBM surface are required for cellulose-CBM binding activity.[66] The conserved flat surface on the bottom of the CBM3a is proposed to interact hydrophobically and selectively with the crystalline cellulose, involving five amino acid residues which form a planar strip (Figure 1.4).[68] The cellulose fibrils are clearly seen in the topography image (Figure 2.10(a)) and the corresponding recognition signals are generated at the same locations on the recognition image (Figure 2.10(b)).[149] The dashed red lines in both Figure 2.10(c) and (d) indicate the obvious correspondence between the recognition signals and the morphology of the crystalline cellulose as observed in topography images (Figure 2.10(a)). Also, the dark areas in the recognition image correspond very well to the areas where the cellulose fibrils are located in the topography images, indicating that the CBM3a molecules bound to the crystalline cellulose surface successfully during the scanning. We noticed that not the whole cellulose area was completely recognized by the modified AFM probe, which is expected given the impurity of the cellulose surface and the inevitable mis-orientation of the binding sites on CBM3a during scanning. As a result, not all the single binding sites were distinguishable on this scale. On average, 70-80% of the binding area was recognized based on the experimental observations based on the analysis of 10 recognition images of crystalline cellulose (each in size of 300 nm $\times$ 300 nm).

To reveal the individual binding sites, we focused on a smoother segment on the topography and recognition profiles for a closer look at the correspondence of the recognition events. As shown in Figure 2.11, most binding sites were clearly observed

and the binding site intervals were measured from the recognition profile of c-c′ cross section as highlighted in the blue square in Figure 2.10(c).

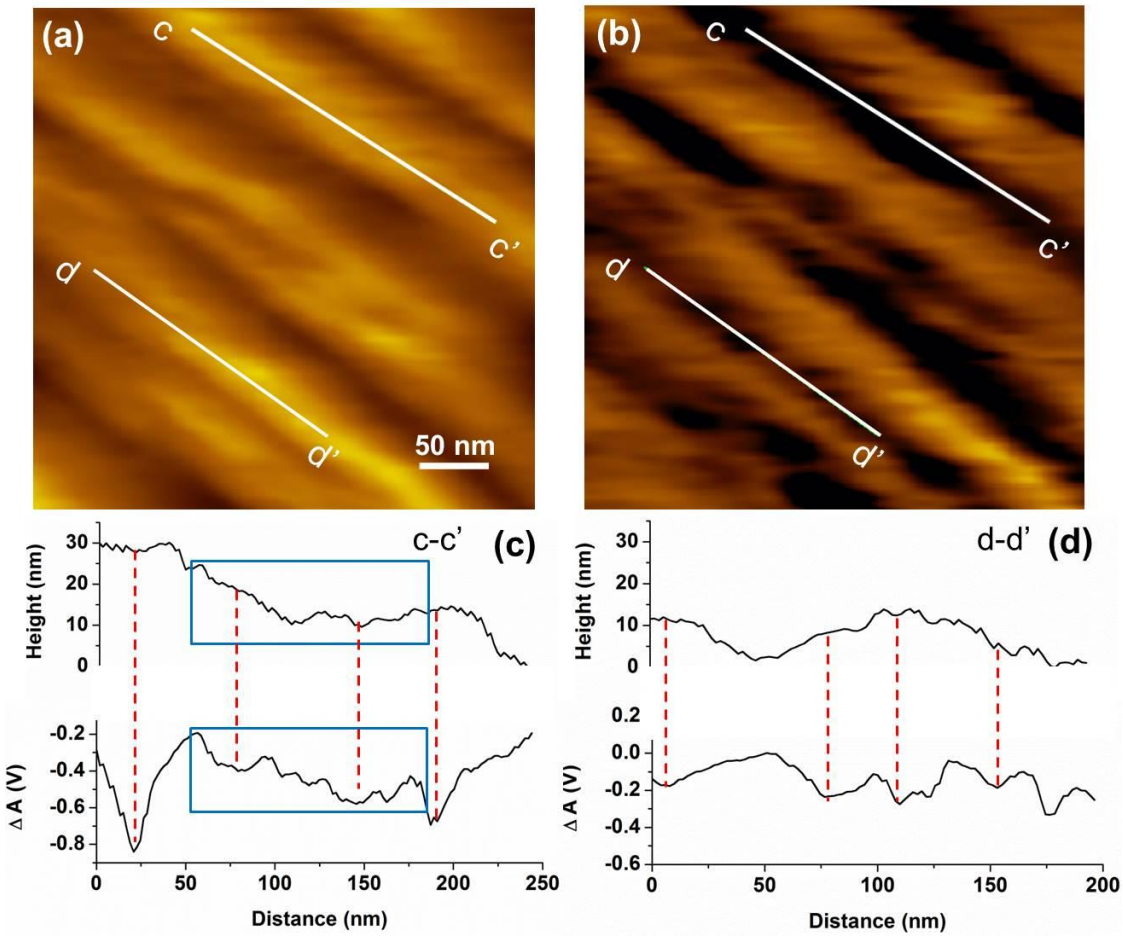

Figure 2.10 AFM topography and recognition images of CBM3a-cellulose interaction. (a) Topography image; (b) recognition image. Two representative cellulose fibrils with recognition signals are highlighted in white lines and the corresponding cross-section profiles are shown in (c) (following line c-c′) and (d) (following line d-d′), respectively. The upper profiles are generated from topography image and the lower ones are generated from recognition image in both (c) and (d). ΔA: Amplitude difference in the recognition signal.[149] The dashed red lines in both (c) and (d) indicate the correspondence of the recognition signals to the morphology of the crystalline cellulose shown in (a).

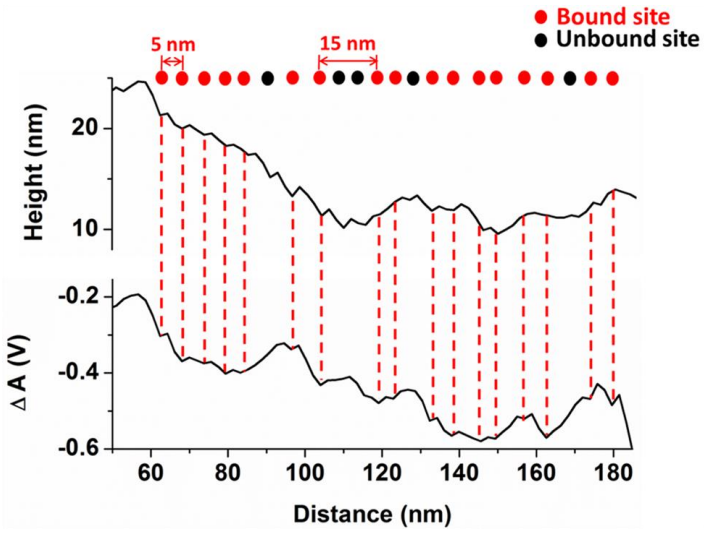

Figure 2.11 Zoom-in binding site intervals measured from the recognition profile of c-c′ cross-section in Figure 2.10(c). The red dot indicates the recognition event (bound site); the black dot indicates the missing recognition events (unbound site). The dashed red lines are shown to guide the correspondence of the recognition events to the signal changes in profiles.

In Figure 2.11, the red and black dots in diameter of about 3 nm (close to the size of single binding site) above each line indicate the recognition event (bound sites) and missed recognition events (unbound sites), respectively. The signal changes in the recognition profile correspond to the dips and bumps in the topography profile randomly, which means that the recognition signals were generated due to the specific binding sites instead of the surface roughness. Additionally, the minimum distance between the centers of two bound sites (red dots) was measured to be 5-8 nm, deducing a separation distance of 2-5 nm, which is in the range of the separation distance guided by quantum dots as discussed above. Some larger distances of 10-15 nm were also observed and were suggestive of separation by 1 or 2 unbound events. We speculated that these missing binding events were caused by short binding time under relatively fast scanning speed

and impurity of the natural cell wall cellulose. On the basis of the analysis of 50 cross-section curves from the recognition area, 41 curves (over 80%) showed similar binding distributions. To further prove the above results, a control experiment using a bare AFM tip was carried out, indicating the absence of specific interactions and binding sites between the cell wall cellulose and bare tip (Figure 2.12).

To confirm that the recognition signals were caused by specific interactions between the modified AFM tip and cellulose, we used a bare AFM tip to image a similar sample surface to observe the differences (the same area could hardly be found due to the complexity and roughness of the natural cell wall surface). Figure 2.12(a) and (b) are topography and recognition images of the same area, respectively. Figure 2.12(c) shows the corresponding topography profile (up) and recognition (down) cross-section profiles of a representative cellulose microfibril labeled by the white line along the chain axis in both Figure 2.12(a, b). The dashed red lines guide the correspondence of the signal changes. Different from the images obtained by modified tip, here no obvious recognition signals in Figure 2.12(b) corresponding to the same location in Figure 2.12(a) were observed, which suggested that there were only very weak, non-specific interactions between the bare tip and cellulose surface. To further prove this presumption, the cross-section profiles were also extracted to compare with the one in Figure 2.12. The recognition signal range (from highest to lowest value) changed only slightly (i.e., from -0.02 to –0.18 V compared to that from -0.2 to -0.6 V in Figure 2.11). Therefore, the results of this control experiment show a much weaker interaction between the bare tip and cell wall cellulose in the absence of the binding module.

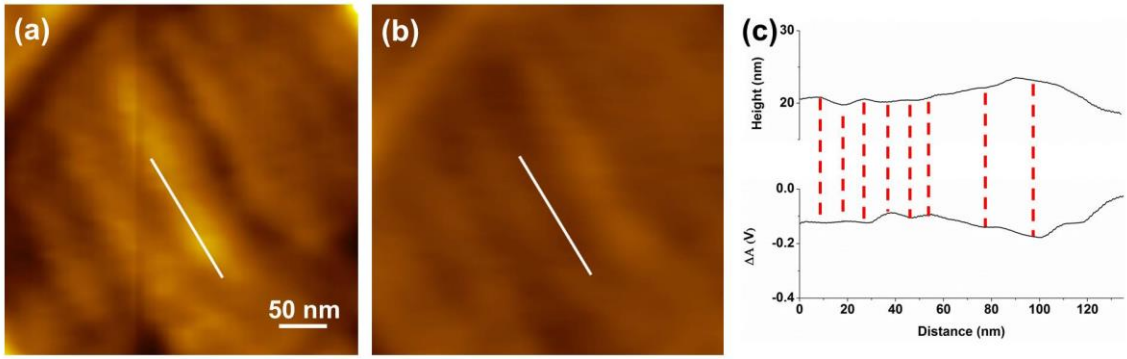

Figure 2.12 AFM topography (a) and recognition (b) images of poplar cell wall cellulose with bare AFM tip (control experiment). One representative cellulose microfibril is labeled by a white line along the chain axis and the corresponding cross-section profiles of topography and recognition images are shown in (c). The dashed red lines guide in (c) guide the correspondence of the signal changes in topography profile (up) to recognition (down) profile. No obvious recognition signals in (b) corresponding to the same location in (a) were observed due to the very weak tip-cellulose non-specific interactions.

Based on the above information, we then measured the unbinding forces between single CBM3a molecule and crystalline cellulose. To ensure the statistic data was reliable, 1000 force-distance (F-D) curves were collected under the loading rate of 67.2 nN/s for the histogram. Using the CBM3a-functionalized tip, two peaks (blue in Figure 2.13) were generated, showing simultaneously the specific (blue, lower and wider peak) and nonspecific (pink, higher and narrower peak) interactions between CBM3a and sample surface. Using the typical F-D curves (type II curves in Figure 2.13 comprising 48% of the total curves), the unbinding force between single CBM3a molecule and crystalline cellulose was determined to be 44.96 ± 18.80 pN under the loading rate of 67.2 nN/s by Gaussian fitting. The remaining 52% of the curves (type II curves in Figure 2.13) showed no evident binding as only 6.27 ± 5.76 pN force was determined in the histogram. Using a bare tip, 95% of the collected F-D curves were grouped as type I curves, giving the same result as the peak showing no binding events using CBM3a-functionalized tip.

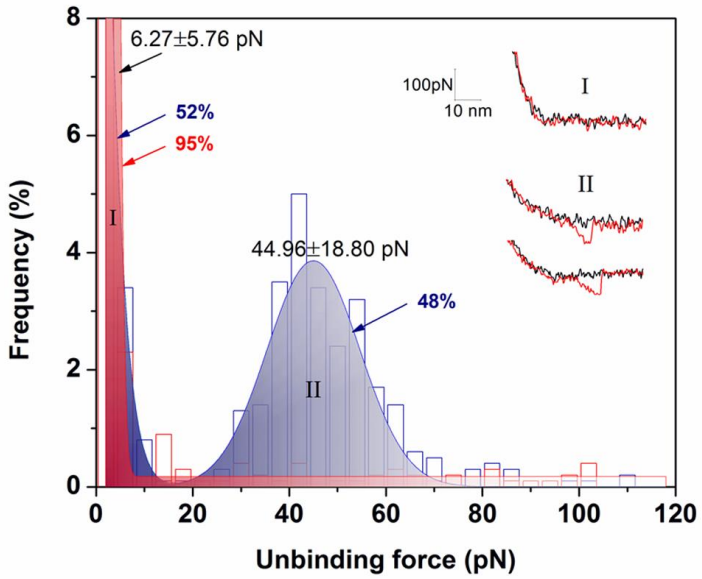

Figure 2.13 Histogram and representative force-distance curves of CBM3a-cellulose binding interactions with specific and nonspecific interaction. The blue area under Gaussian fitting curve indicates both the specific (labeled as II, the same for representative curve) and nonspecific (labeled as I, the same for representative curve) interactions between the cell wall cellulose and CBM3a-functionalized AFM tip. The red area shows the nonspecific interactions between cellulose and bare AFM tip in the control experiment. A total of 1000 curves were collected for each experiment to construct histograms for the fitting. Trace curves: black; retrace curves: red. The unbinding force was determined by Gaussian fitting under the loading rate of 67.2 nN/s.

We noticed that the unbinding force of CBM3a and crystalline cellulose was much smaller than that needed to break a covalent bond (larger than 1 nN at the loading rate of 10 nN/s),[187] or that between antibody and antigen,[175] thereby indicating a weaker interaction between CBM3a and cellulose. According to previous works, the protein-carbohydrate affinity brought about by conserved aromatic residues in the planar strip and adjacent anchoring residues at the bottom surface of CBM3a mainly relies on hydrophobic van der Waals contacts, with partial contribution by the polarization interactions between the residues with polar side-chains and the pyranose rings located on

the hydrophobic face of crystalline cellulose.[67, 188] Replacement of the above binding residues with alanine has shown a great increase in dissociation constant of the binding module, indicating a much weaker binding affinity due to the absence of the aromatic, hydrophobic interactions.[189] We speculate that the nonspecific peaks measured in Figure 2.13 was mainly attributed to mis-orientation of CBM3a molecule on cellulose surface or the feeble interactions between CBM3a and non-crystalline cellulose component on the sample surface.

2.4 Conclusions

In this work, the GNP-CBM3a complexes were observed to bind to the cellulose surface and closely aligned with the cellulose extension. The binding behavior was proved to be real after comparing the topography and recognition images of the same crystalline cellulose exposed area as well as the force measurement done by dynamic force microscopy. Quantitatively, the unbinding force between the CBM3a and crystalline cellulose was determined as 44.96 ± 18.80 pN under the loading rate of 67.2 nN/s. To further determine the CBM-cellulose interaction, additional unbinding forces under different loading rates need to be tested, and other types of type A CBMs should be selected to quantitatively measure their differences in binding affinities.

CHAPTER 3

KINETICS STUDY OF AFFINITY INTERACTIONS BETWEEN CBM AND NATURAL/EXTRACTED CRYSTALLINE CELLULOSE

3.1 Introduction

CBM binding to cellulose is one of the most significant carbohydrate-protein interactions.[157, 180, 190] Protein-carbohydrate interactions play important roles in various biological activities such as protein folding, cell adhesion and surface functions.[191-193] Therefore, understanding the CBM-cellulose interactions will also pave the way for understanding the binding properties of protein-carbohydrate interactions, such as CBM or CBM-like modules binding to the plant cell walls or cell surface. The mechanism of CBM-cellulose interactions has been studied extensively by diverse approaches in the past several years.

With the current progress in this field, researchers increasingly focus on the molecular basis of the CBM-cellulose interactions.[141] As mentioned previously, some molecular modeling and simulation work has been reported to mimic the dynamic process of the CBM-cellulose complex.[144-146] However, this approach has many limitations and can hardly reach to solid conclusions. For instance, the binding and unbinding processes of CBM molecules to the large crystalline surface of cellulose microfibrils still need tedious work to build the model and it takes a lot of computing resources and time to simulate the equilibration process. Different modeling approaches and force fields generated different structures and behavior of the crystalline cellulose

microfibril.[194] Moreover, the binding processes of different families of CBMs to the intact microcrystalline cellulose surface are still missing.

On the other hand, traditional bulk experimental measurements quantitatively showed a wide range of the affinity of different CBMs on the crystalline or amorphous cellulose substrates. However, no consistent conclusions could be drawn and some of the data reported could be somehow contradictory to each other. For instance, according to the review work done by Tomme *et al.*,[49] CBM2a exhibited high affinities for bacterial microcrystalline cellulose (BMCC) with the K_a equals to $3.2 \times 10^6\ M^{-1}$), but the K_a of CBM3 to BMCC varied from a lower value of $1.7 \times 10^6 M^{-1}$ to a much higher value of $2.9 \times 10^7\ M^{-1}$.Mclean and co-workers also reported in 2002 that the K_a of CBM2a to BMCC was $3.2 \times 10^6\ M^{-1}$, but the K_a of CBM3 to BMCC was only $1.0 \times 10^6\ M^{-1}$.[142] To understand the hydrolytic process of a single enzyme molecule, study of the CBM-cellulose binding indicating the actual reaction dynamic and kinetic mechanism is quite necessary.

Recently, AFM recognition imaging was frequently combined with SMDFS to measure intra-molecular unfolding forces of individual molecules and inter-molecular forces between various specific reaction molecules.[149, 157, 175, 195] Due to the complexity of plant cell wall surface structures, this method provides a more comprehensive approach than conventional bulk solution ones. In the previous chapter, we determined the binding specificity of a type A CBM, CBM3a to crystalline cellulose surface. In this study, we mapped the natural poplar cell wall surface and extracted crystalline cellulose by AFM recognition imaging. Subsequently, we measured unbinding forces between the CBM and cellulose using CBM3a and another type A CBM, CBM2a (derived from *Cellvibrio*

japonicus Xyn10A) functionalized AFM tips, respectively. We also determined the kinetic parameters for the interactions of these two CBMs and cellulose to understand the binding mechanisms.[196]

3.2 Experiments

3.2.1 Preparation of recombinant CBM2a

The preparation procedure of recombinant CBM3a has been described in detail in Chapter 2. The recombinant CBM2a was derived from *Cellvibrio japonicus* Xyn10A with a molecular weight of 12328 and an estimated pI of 8.08. The translated amino acid sequence of the recombinant CBM2a is:

MQTATCSYNITNEWNTGYTGDITITNRGSSAINGWSVNWQYATNRLSSSWNANV
SGSNPYSASNLSWNGNIQPGQSVSFGFQVNKNGGSAERPSVGGSICSGSVAIEGR
HHHHHH.

3.2.2 Poplar sample preparations for recognition imaging and force measurement

The natural poplar cell wall sample preparation has been described in the previous chapter.[181] The pretreatment of the extracted single crystalline cellulose followed a widely used procedure.[119] Briefly, 1 mg of microtomed poplar slice was treated by a mixture of NaOH and Na_2S solution (1% w/v and 15.5 mL, respectively) at 80 ˚C for 1.5 h (bath ratio: 1 : 30). The sample was then bleached by sodium chlorite (1.7% w/v, 5 mL) at 80 ˚C for 2.5 h in the presence of an acetate buffer (0.135 g NaOH and 0.375 mL glacial acetate acid in 5 mL de-ionized (DI) water). The bleached cellulose fibers were centrifuged 8 times with DI water (SORVALL BioFuge Pico Microcentrifuge) and then

dried in air at room temperature. Further, the fibers were hydrolyzed in sulfuric acid (64% w/w, 1 mL) at 60 ˚C for 30 min under strong agitation. The reaction was stopped by addition of 2 mL cold DI water. The diluted suspension is centrifuged at 10,000 rpm for 10 min to obtain the precipitates. The last two steps were repeated (around 10 times) until a turbid suspension was obtained. The suspension was collected and dialyzed using a micro dialyzer (QuixSep) for 5 h. Finally, the suspension was sonicated for 10 min and stored at 4 ˚C with addition of 0.05% sodium azide.

AFM sample preparation for recognition imaging and force measurement, poly-L-lysine hydrobromide (MW 53,900, 0.1 wt%, 10 mL) was dropped onto a freshly cleaved mica surface. After 5 min, the mica surface was gently washed by 200 mL DI water 4 times and dried in air. The pretreated poplar suspension (0.1 wt%, 6 mL) was dropped onto the modified mica surface. After 3 min, the mica surface was washed using 200 mL DI water 3 times to remove the extra cellulose. After drying in air, the mica surface was further incubated with sodium glutamate (NaGlu) solution (10 wt%, 10 mL) for 10min and then washed gently using 200 mL DI water 4 times. Finally the air-dried mica was fixed into an AFM flow cell and then filled with 0.3 mL Tris-Cl buffer (10 mM Tris-Cl and 150 mM NaCl, pH = 7.5) for recognition imaging and force measurement.

3.2.3 AFM tip functionalization

AFM tip modification by CBM3a has also been introduced in Chapter 2.[181] Here the AFM tip with CBM2a was functionalized in a similar way. Briefly, the gold-coated CS-10 silicon AFM tips (Nanoscience Instruments, nominal spring constant of about 0.1 N/m) were first immersed in the HS-PEG_{2000}-NTA crosslinker (Nanocs Inc.) (0.2 mg/mL,

300 mL) for 3 h, and then in $NiCl_2$ (10 mM, 20 mL) for 30 min, at room temperature. The tips were then washed repeatedly and immersed in 400 mL Tris-Cl buffer (10 mM Tris-Cl and 150 mM NaCl, pH 7.5) with addition of CBM2a (27 mg/mL, 6 mL). The solution was then kept at 4 ˚C for 8 h. The modified tips were finally washed thoroughly in Tris-Cl buffer for future imaging.

3.2.4 Experimental setup for recognition imaging and force measurement

The simultaneous topography and recognition images were obtained using Top magnetic AC (TopMAC) mode using a PicoTREC controller under a PicoPlus Molecular Imaging system (Agilent Technologies, Santa Clara, CA). During the recognition imaging of the cellulose, the F-D curves were also recorded. Over 300 representative F-D curves were used under at each loading rate and processed using a home-designed Labview program to construct the histograms. Gaussian fitting was used to identify the values of the most probable unbinding forces.

3.3 Results and discussions

3.3.1 AFM recognition imaging of natural and extracted cellulose

We first monitored the CBM-cellulose binding events on the crystalline cellulose surface using both natural and extracted cellulose microfibrils. Figure 3.1 shows the topography and recognition images of crystalline cellulose from natural poplar cell walls and after extraction using CBM3a (a-d) and CBM2a (e-h) functionalized AFM tips.

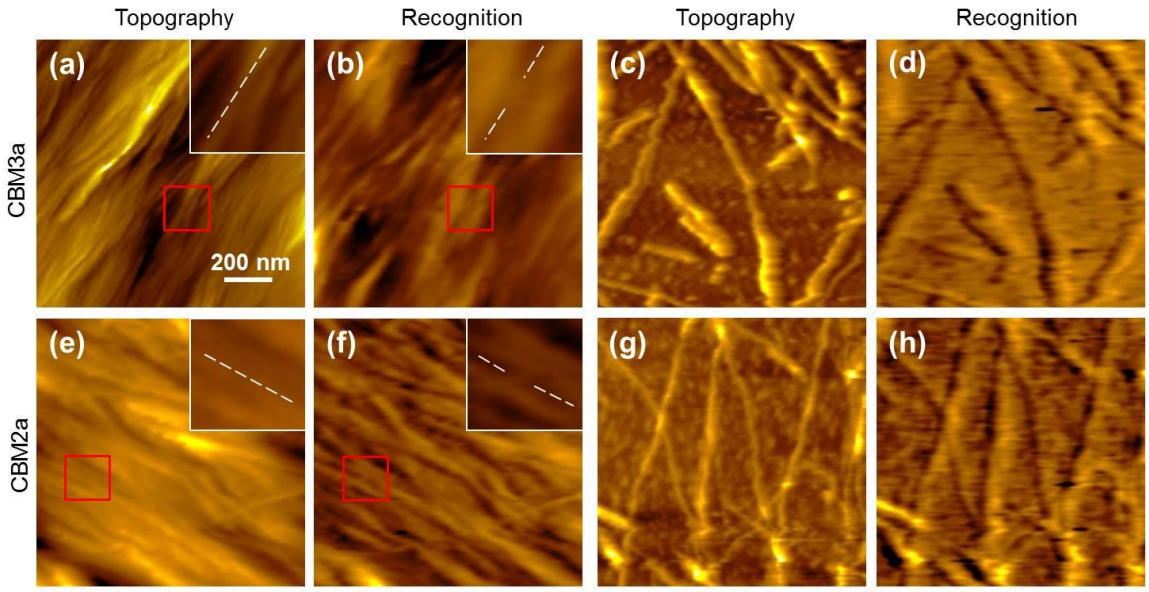

Figure 3.1 Topography (a, c, e, g) and recognition (b, d, f, h) images of natural poplar cell wall cellulose (a, b, e, f) and extracted crystalline cellulose (c, d, g, h). (a-d) are imaged by CBM3a-functionalized AFM tip; (e-h) are imaged by CBM2a-functionalized AFM tip. The red frames in (a), (b), (e) and (f) highlight the areas on the crystalline cellulose surface with probable impurities. Insets: enlarged areas in the red frames; the representative cellulose microfibrils in (a) and (e) and the corresponding recognition signals in (b) and (f) are labelled with white dashed lines.

The topography images in Figure 3.1 clearly show that the crystalline cellulose fibrils on the natural cell wall are closely packed (Figure 3.1(a, e)) while the extracted cellulose fibrils are well isolated (Figure 3.1(c, g)). The surface areas recognized by both CBM3a and CBM2a are shown as dark signals (Figure 3.1(b, d, f, h)). On the natural cellulose surface, the binding sites lay closely to each other due to the compact crystalline cellulose structure (Figure 3.1(b, f)). However, on the extracted cellulose sample, the binding sites were found to orderly align along the cellulose microfibril (Figure 3.1(d, h)). Impurities may exist on the natural cell wall surface, such as hemicellulose and other non-carbohydrate residues; hence certain small areas on the cellulose surface cannot be recognized by the CBM-functionalized tip. For example, the red frames in Figure 3.1(a, b,

e and f) highlight the small areas on the crystalline cellulose surface with probable impurities. Insets are the enlarged areas in the red frames and the representative cellulose microfibrils are labelled with dashed white lines. The recognition signals along the same cellulose microfibrils (dashed white lines) are interrupted as shown in Figure 3.1(b) and (f) (insets) due to the existence of impurities.

To further determine the binding efficiencies of CBM3a and CBM2a, the binding sites on the surface of extracted single cellulose microfibrils were recognized by the above two binding modules. Their topography and recognition images were also compared. Figure 3.2 exhibits a small area of extracted single cellulose microfibrils recognized by the CBM3a-functionalized AFM tip in topography (a) and recognition (b) images. The extracted cellulose microfibrils in the topography image (a) show clear recognition signals in the corresponding recognition image (b). To identify the individual binding sites, we analyzed the cross-section profiles of two representative extracted cellulose microfibrils marked a-a', b-b' in (a) and c-c', d-d' in (b). Figure 3.2(c) and (d) compare the cross-section profiles of the two labeled extracted single cellulose microfibrils marked in (a) and (b). Each unbinding event is highlighted by a vertical dashed red line, indicating the corresponding topography and recognition signals. The black curve in Figure 3.2(e) is a representative F-D curve measured on the extracted cellulose microfibril at point A in Figure 3.2(a), corresponding to A' in Figure 3.2(b). The red curve in Figure 3.2(e) was measured on the mica substrate at point B, corresponding to point B' in Figure 3.2(b). The overlay of these two curves indicates that the interaction between the CBM3a molecule on the AFM tip and the cellulose surface was specific, since no interaction was detected between CBM3a and mica surface.

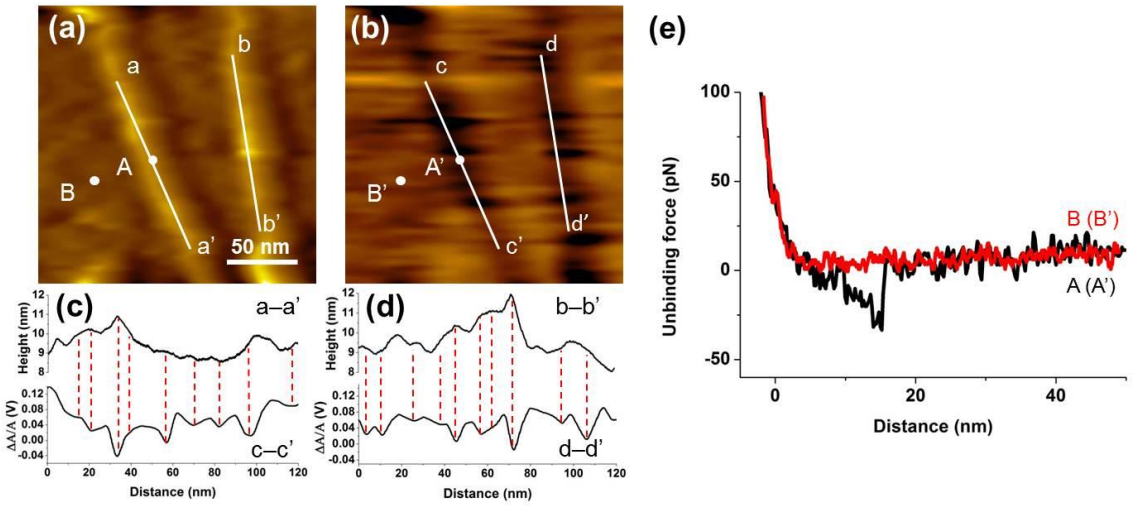

Figure 3.2. Topography (a) and recognition (b) images of extracted cellulose microfibrils with cross-section analysis (c) and (d) on smaller surface areas. The images of (a) and (b) were obtained using the CBM3a-functionalized AFM tip. The curves in (e) represent F-D curves measured (under the loading rate of 40 nN/s) at point A in (a), which corresponds to point A' in (b), and point B in (a) corresponds to point B' in (b). The F-D curve A (A') (in black) shows the specific interaction between CBM3a and the extracted cellulose microfibril surfaces; while the curve B (B') (in red) shows no interaction between AFM tip and mica surface.

As shown in Figure 3.2(c) and (d), the smallest intervals in the cross-section profiles were measured to be 5-8 nm, which is consistent with the result we obtained in Chapter 2.[181] The binding site of a single CBM3a molecule has proved to directly come into contact with 6-7 glucose units (3-4 nm in width) on the surface of cellulose microfibrils.[68] Therefore, a separation distance of 2-5 nm between two binding sites can be deduced. This value is consistent with the range of the separation distance labelled by quantum dots as reported previously by Xu *et al.*[186] Due to the relatively short unbinding time under fast scanning speed and the blocking by the impurities on the cellulose crystalline surface, some of the expected binding sites didn't show any binding signals, giving a 10-20 nm separation distance between two binding events.

To quantitatively compare the binding efficiencies of CBM3a and CBM2a, we measured the recognition area percentage (RAP) on both natural and extracted cellulose microfibril surfaces. The RAP is defined as the ratio of the bound area on single cellulose microfibrils (nm^2) to the total surface area of single cellulose microfibrils (nm^2) (Equation 3.1). The cellulose bound area to CBM3a or CBM2a was considered as the dark area generated by the recognition signal from recognition images, and the apparent surface area of cellulose included the entire bright area of cellulose from topography images. These area values were calculated using Picoscan software.

$$\mathrm{RAP}(\%) = \frac{\text{Bound area on single cellulose microfibril } (nm^2)}{\text{Total surface area of single cellulose microfibril } (nm^2)} \quad \text{Equation 3.1}$$

Here the bound area is highlighted as the black circle in the recognition image Figure 3.3(b) and the total surface area is highlighted as the white circle in both topography and recognition image Figure 3.3(a-b). Each total surface area is defined as a cellulose surface about 200 nm in length and 25 nm in width. The RAP of 20 cellulose sections was collected to construct a histogram for each CBM on each substrate. The final RAP value was determined by Gaussian fitting (Figure 3.3(c-g)). The results showed that RAPs of CBM3a and CBM2a to natural cellulose surface were 56.7 $\pm$ 10.0% and 47.0 $\pm$ 12.8%, respectively. The RAPs of CBM3a and CBM2a to extracted cellulose surface were a little larger, with the value of 73.7 $\pm$ 11.1% and 63.6 $\pm$ 13.5%, respectively. The data indicates that under the same experimental conditions, CBM3a was capable of binding about 9.7% more area than that of CBM2a on natural cellulose and about 11.1% more area than that of CBM2a on extracted cellulose microfibrils. This difference on the RAP at single molecule level is mainly due to the detailed molecular structures of these two binding modules and their cellulose binding conformations.[68-69]

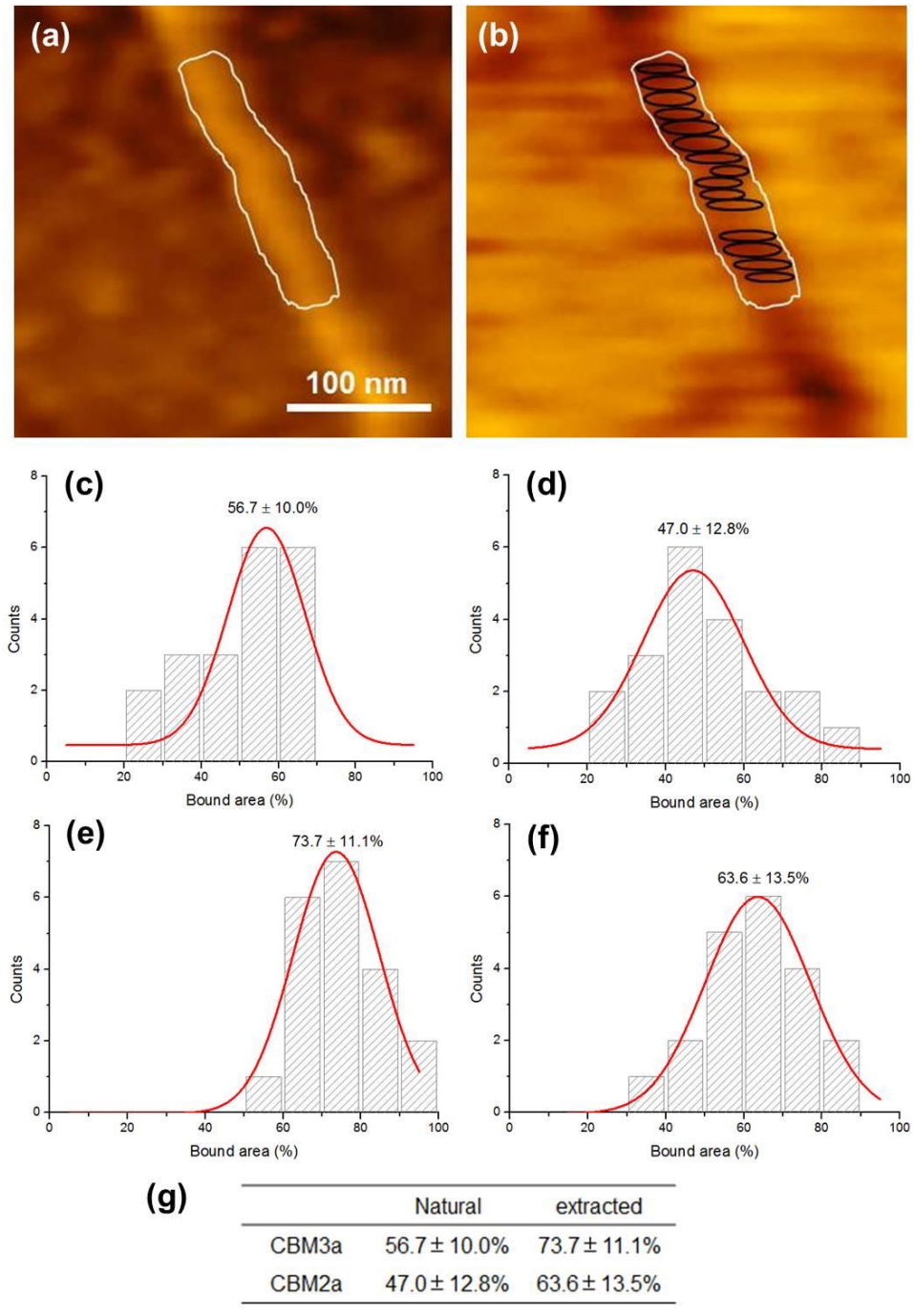

(g)

	Natural	extracted
CBM3a	56.7 ± 10.0%	73.7 ± 11.1%
CBM2a	47.0 ± 12.8%	63.6 ± 13.5%

Figure 3.3 RAP calculation of CBM3a and CBM2a binding on extracted crystalline cellulose. (a, b) Representative AFM images for calculating the RAP of CBM3a-bound cellulose microfibril. Black circle: bound area; white circle: total surface area. (c, d) RAP calculation of CBM3a and CBM2a binding to natural cell wall cellulose. (e, f) RAP calculation of CBM3a and CBM2a binding to extracted cellulose microfibril. (g) RAP summary of the CBM-cellulose interaction. Each histogram was constructed by RAP values averaged from 20 cellulose microfibril sections (approximately 200 nm in length and 25 nm in width).

Some previous work confirmed that CBM3a has 10 conserved residues participating in the cellulose binding activity, with five of them (Trp118, Arg112, Asp56, His57, and Tyr67) in the planar strip and another five of them as anchors (Asn16, Gln110, Ser12, Asn10, and Ser113).[68] Among these residues, His57 and Tyr67 can form strong hydrogen bonds with the glucose units of cellulose, and in turn stabilize the binding conformation.[68] Other residues can also contribute to possible hydrogen bonding and van der Waals interactions to help orientate the CBM3a active residues to the right locations on the cellulose surface. The CBM2a structure in the literature shows 8 conserved residues involved in binding, with four of them (Trp17, Asn87, Trp54, and Trp72) in the planar strip, and another four (Asn15, Asn24, Gln83, and Gln52) as anchors.[68] For the CBM2a used in our experiment, we found that the residues Asn15, Trp17, Trp54, and Trp72 were conserved in the similar positions in the secondary structure, but other active residues changed. For the planar strip, Asn87 helps Trp54 form the correct orientation on the cellulose surface; while for the anchor residues, only Asn15 keeps in the secondary structure.[68] Therefore, the CBM2a we used may not show affinity as strong as that reported in the literature. Compared to CBM3a, the contact area between CBM2a and cellulose in the literature is smaller than that between CBM3a and cellulose; therefore, the overall binding affinity of CBM3a in our experiments is expected to be higher than that of CBM2a. The topography and recognition images of extracted cellulose microfibrils using CBM2a-functionalized AFM tip with cross-section analysis are also provided in Figure 3.4, which shows less binding events than the CBM3a-cellulose interaction. Moreover, CBM3a and CBM2a show 17% and 16.6% more bound area on natural cell wall cellulose than that on extracted cellulose, respectively, which may be

resulted from the more impurities blocking the CBMs from binding to the cellulose crystalline surface.

As shown in Figure 3.4, the extracted cellulose microfibrils in topography image Figure 3.4(a) show clear recognition signals at the corresponding positions in recognition image Figure 3.4(b). The cross-section profiles in Figure 3.4(c) and Figure 3.4(d) are the comparison of two representative single cellulose microfibrils marked as a-a', b-b' in (a) and c-c', d-d' in Figure 3.4(b). Each binding event on these two microfibrils is highlighted by vertical red, dashed lines.

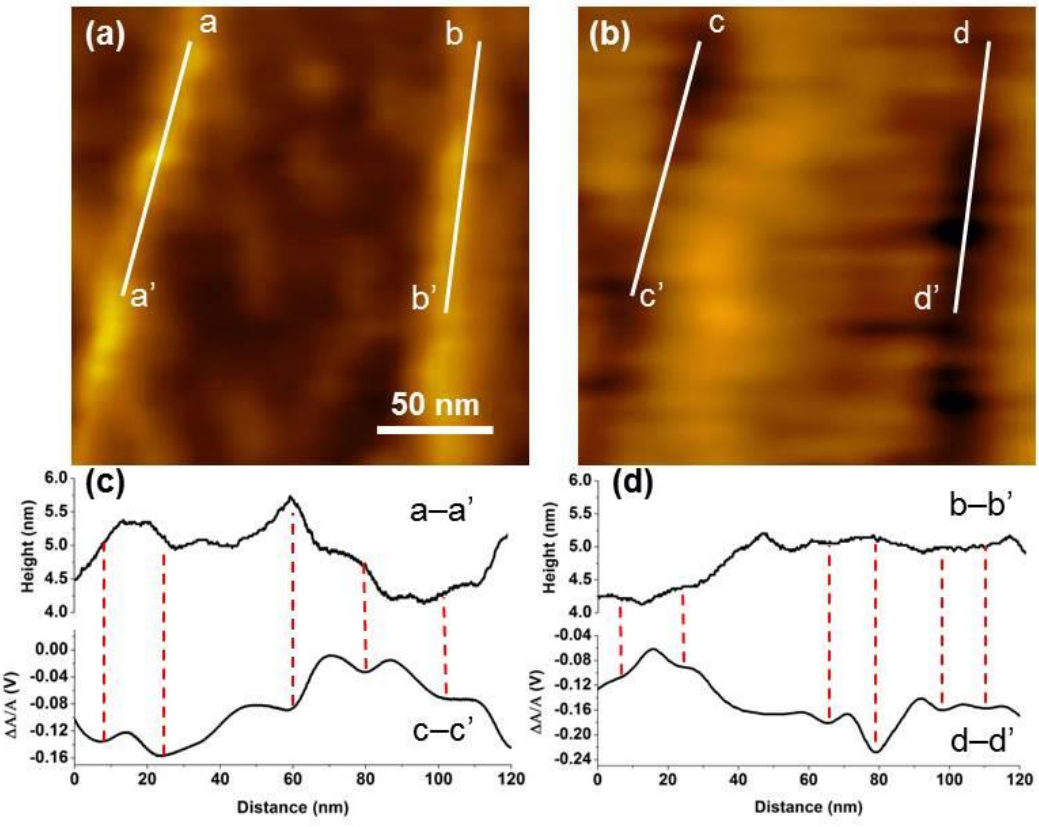

Figure 3.4 Topography (a) and recognition (b) images of extracted cellulose microfibril with cross-section analysis (c) and (d) on a smaller area. (a, b) are imaged by CBM2a-functionalized AFM tip.

The cross-section analysis of CBM2a-celluose interaction shows less binding events on the extracted single cellulose microfibril surface with the same length than those between CBM3a and the extracted single cellulose microfibril surface. The binding intervals on the cellulose microfibril surface vary from 10 to 30 nm, which is larger than 5 to 20 nm as observed on the CBM3a-bound cellulose surface, indicating a less efficient binding of CBM2a to the crystalline cellulose surface.

3.3.2 Affinity study of CBM3a/2a binding to natural/extracted crystalline cellulose

To understand the binding mechanism, we measured the single molecule binding affinity based on F-D curves. In the traditional bulk experiments, the affinity (described as association constant K_a) of different CBMs on various carbohydrate substrates is usually measured from an average value of a large amount of CBM molecules. All these results are based on statistical calculations involving numerous protein molecules each time. This may introduce various sources of uncertainties when compared with the study of affinity and binding mechanisms of a single CBM molecule. The single molecule interaction measurements may provide data to determine the in-depth dynamic and kinetic mechanisms of the CBM-cellulose interactions, which has not been reported yet.

Based on the study of molecular interactions of biological molecules with dynamic force spectroscopy,[197-199] it has been widely accepted that weak non-covalent bonds have limited lifetimes and can break apart when the applied external forces last long enough time.[200] According to Bell's model,[177] the reaction dissociation rate, or off rate, increases exponentially with the external force. Therefore, to calculate the off rates of the CBM-cellulose interactions on the cellulose surface, we measured the unbinding forces at 11 incremental loading rates from 0.5 nN/s to 500 nN/s.

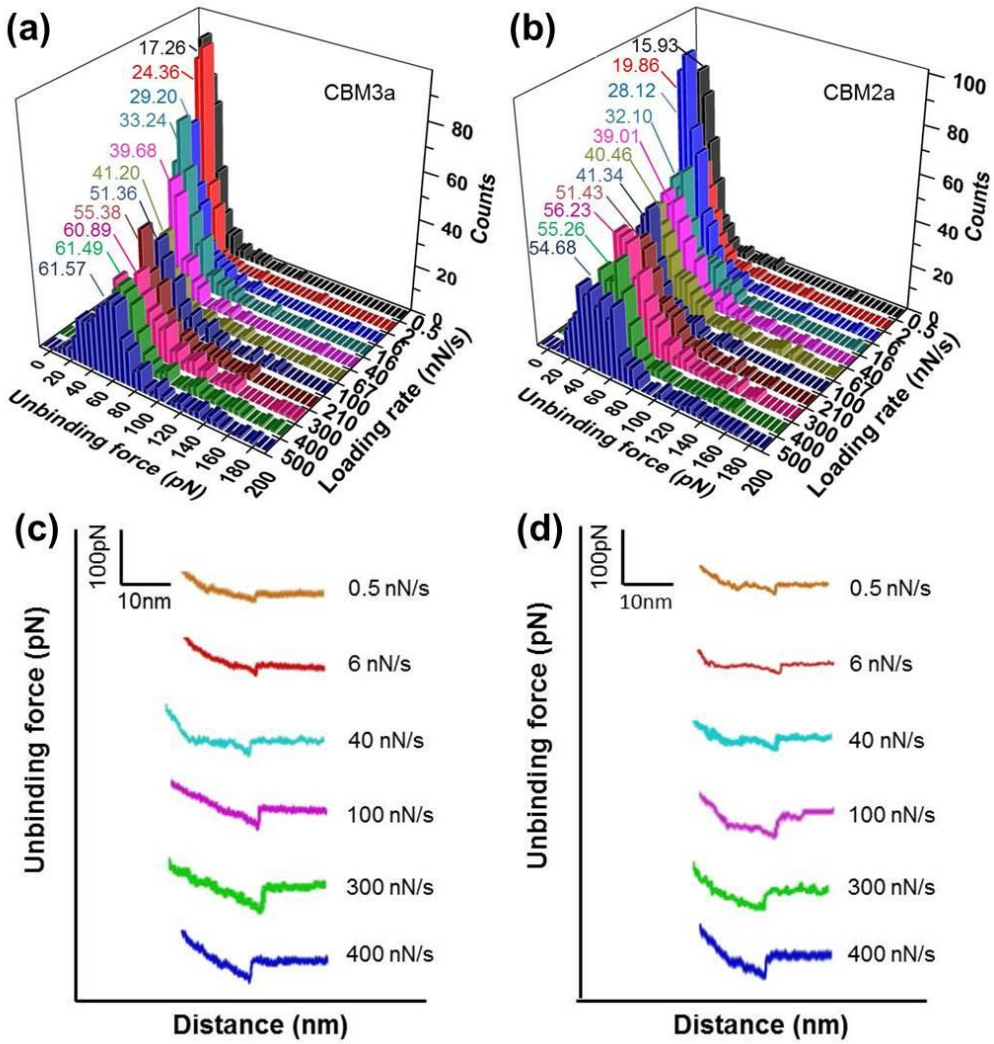

Figure 3.5 Force histograms generated under 11 loading rates and the representative F-D curves. (a) CBM3a-extracted cellulose microfibril; (b) CBM2a-extracted cellulose microfibril interactions. Each histogram was built from over 300 unbinding events and the most probable unbinding force labelled on the top was obtained by Gaussian fitting. The unbinding force increased with incremental loading rates until 300 nN/s, where the unbinding reaction reached the energy barrier and the force no longer changed. (c,d) Representative F-D curves under 6 loading rates of the CBM3a-extracted cellulose microfibril (c) and CBM2a-extracted cellulose microfibril (d) unbinding interactions.

Figure 3.5 shows the 11 force histograms, each of which was constructed from over 300 F-D curves (an example is shown in Figure 3.1(e)) for both CBM3a-extracted

single cellulose microfibril (a) and CBM2a-extracted single cellulose microfibril (b) interactions, as an example. The histograms are arranged in the 3D figure with the most probable unbinding force calculated using Gaussian fitting (force values labelled on top). We observed that, at the loading rates higher than 300 nN/s, the unbinding force reached its saturation, which indicates the minimum force to overcome the energy barrier (E_b) of CBM-cellulose non-covalent interactions instantaneously. Some representative F-D curves of CBM3a and CBM2a-extracted cellulose microfibril interactions are listed in Figure 3.5 (c, d). No obvious difference was observed between the shapes of the curves measured from CBM3a-extracted cellulose microfibril and CBM2a-extracted cellulose microfibril interaction.

We also determined the lifetime of the bond under external force (t_F). The t_F value was calculated from Equation 3.2 derived based on Bell's model,[177]

$$t_F = t_{off} e^{(-\frac{F \cdot x_D}{k_B T})} = \frac{1}{k_{off}} e^{(-\frac{F \cdot x_D}{k_B T})} \quad \text{Equation 3.2}$$

Here F is unbinding force (pN), x_D is barrier length (nm), t_{off} is natural lifetime of the bond without external force (s), k_{off} is dissociation rate or off rate (s^{-1}), T is effective temperature (300 K) and k_B is Boltzmann's constant. Due to the thermal activation, the non-covalent bonds have modest lifetimes which are gradually shortened under external force. It has already been predicted that the bond lifetime depends on the rapidity of applied forces. The most probable unbinding force will determine the most probable binding lifetime at the specific force loading rate (r). Therefore, we can establish a relationship between the measured unbinding force and the affinity between CBM and cellulose. The unbinding forces under a series of loading rates determine the k_{off}, and the

larger the k_{off} value, the lower the affinity. Taking CBM3a-extracted cellulose microfibril interaction as an example, the plot of unbinding force and t_F versus the logarithmic coordinates of loading rates is shown in Figure 3.6(a). The data points for unbinding forces are marked in black squares and the data points for t_F are marked in red triangles. The t_F decreases dramatically from 7.92 s under 0.5 nN/s to 0.01 s under 300 nN/s.

The force spectroscopy reflects only the non-equilibrium state of the CBM-cellulose interactions, since the F-D curve is measured at a certain loading rate. The most probable unbinding force, when plotted as a function of ln(r), can be used to reconstruct the energy landscape along the unbinding pathway. According to Jarzynski's equality, the free energy change of the CBM3a-extracted single cellulose microfibril interactions under the equilibrium state can be reconstructed.[178, 201] The free energy profile was rebuilt based on 20 F-D curves and the reconstructed free energy change for CBM3a-extracted cellulose microfibril interactions was calculated to be 27.06 ± 3.42 kcal/mol or 45.33 ± 5.73 k_BT (Figure 3.6(b)). The reconstructed free energy of CBM2a-extracted single cellulose microfibril interaction is 25.21 ± 2.15 kcal/mol or 42.51 ± 3.63 k_BT, for CBM3a-natural cellulose microfibril interaction, the value is 29.86 ± 2.36 kcal/mol or 50.02 ± 3.95 k_BT, and for CBM2a-natural cellulose microfibril interaction, the value is 28.61 ± 2.93 kcal/mol or 48.02 ± 3.86 k_BT (see Table 3.1 and Figure 3.6). The results show a very similar affinity of the two CBM molecules to the cellulose surface. Nevertheless, some differences can be identified for the two CBMs and for the natural and extracted cellulose microfibril surfaces: the CBM3a-natural cellulose microfibril complex has the highest free energy change and the CBM2a-extracted cellulose microfibril complex has the lowest one.

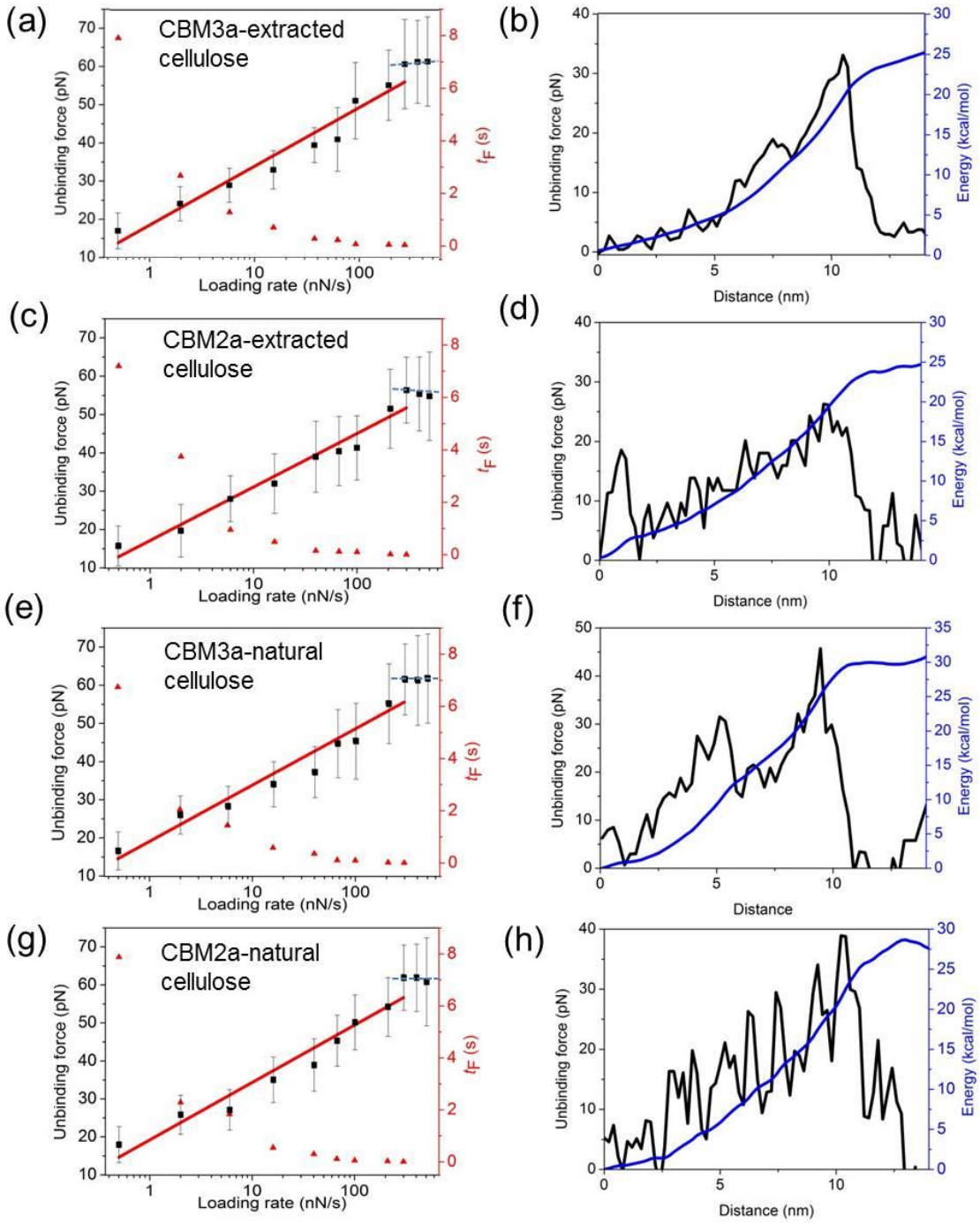

Figure 3.6 The unbinding forces and t_F vs. loading rate plots and energy profiles of CBM binding to cellulose. (a, c, e, g) The unbinding forces and t_F vs. loading rate plots for the interactions between CBM and cellulose microfibrils. The data points for the unbinding forces are marked with black squares and the data points for t_F are marked in red triangles. The unbinding forces after saturation are marked with dashed blue lines. (b, d, f, h) The weighted average F-D curves and the work integral used to obtain the reconstructed free energy changes for CBM-cellulose microfibril interactions. The averaged F-D curve is marked in black and the free energy profile is marked in blue.

Specifically, the CBM3a-celluose complexes have higher free energy changes than that of CBM2a-cellulose complexes, which can be contributed to a larger contact area of CBM3a to the cellulose surface because of more CBM3a binding residues and their wider occupancy of the binding interface.[68] The proposed reason for both CBM-natural cellulose complexes to have higher free energy than that of CBM-extracted cellulose microfibril complexes is that the crystalline structure of the extracted cellulose microfibrils may be partially damaged during the extraction procedure.[202] This may lead to the consequence that only partial binding residues of the CBMs can bind to the damaged crystalline cellulose surface so that the binding of CBMs to the extracted cellulose is not so tight as to the intact, natural cellulose.

Table 3.1 Dynamic and kinetic parameters for binding of CBM3a and CBM2a to natural and extracted cellulose microfibrils. x_D: barrier length; E_b: energy barrier; k_{off}: dissociation rate; ΔG: reconstructed free energy.

	CBM3a		CBM2a	
	Natural	Extracted	Natural	Extracted
x_D (nm)	0.64 ± 0.06	0.63 ± 0.06	0.68 ± 0.05	0.63 ± 0.05
E_b (kcal/mol)	15.12 ± 4.08	14.23 ± 2.43	14.87 ± 3.15	13.73 ± 3.44
k_{off} (s^{-1})	0.0081 ± 0.0002	0.0089 ± 0.0006	0.0082 ± 0.0002	0.0099 ± 0.0008
ΔG (kcal/mol)	29.86 ± 2.36	27.06 ± 3.42	28.61 ± 2.93	25.21 ± 2.15

Due to the small differences in free energy changes, we took a closer look at the t_F values of different CBM-cellulose complexes to compare their kinetic properties. At the lowest loading rate of 0.5 nN/s and the highest loading rate of 300 nN/s before the saturation, the CBM3a-extracted cellulose microfibil interaction shows the longest bond lifetime of 7.92 s and 0.01 s, respectively, while the CBM3a-natural cell wall cellulose shows the shortest bond lifetime of 6.74 s and 0.01 s, respectively (see Figure 3.7).

Moreover, the CBM2a-extracted cellulose microfibril complex shows a slightly shorter bond lifetime of 7.19 s and 0.01 s than that of the CBM2a-natural cell wall complex, which is 7.88 s and 0.01 s, respectively. The calculated and experimental t_F values of the four sets of experiments are plotted with the 9 loading rates before the saturation and the results are listed in Figure 3.7. These results exhibit a good agreement between the calculated and experimental t_F values. Specifically, the t_F of CBM2a-extracted cellulose microfibril interaction decreased from 7.19 s under 0.5 nN/s to 0.01 s under 300 nN/s. The t_F of CBM3a-natural cellulose microfibril interaction decreased from 6.74 s under 0.5 nN/s to 0.01 s under 300 nN/s, while that of CBM2a-natural cellulose microfibril interaction decreased from 7.88 s under 0.5 nN/s to 0.01 s under 300 nN/s. Similarly, CBM3a had a shorter bond lifetime on natural cellulose microfibril and longer bond lifetime on extracted cellulose microfibril. However, CBM2a had a shorter bond lifetime on extracted cellulose microfibril and longer bond lifetime on natural cellulose. The differences of bond lifetime among the four complexes are not very pronounced. The probable reason is that compared to CBM2a, the highly conserved binding residues on the CBM3a planar strip are more sensitive to the impurities on the natural cell wall which can block the binding sites along the cellulose microfibrils. For CBM2a, the disruption of the crystalline structure on the cellulose microfibril surface probably has more influence to the planer strip and anchor residues for binding.[68, 180]

The dissociation rates and energy barrier E_b can also provide a theoretical support for our dynamic and kinetic study on the CBM-cellulose interaction mechanism. To calculate the E_b for all of the CBM3a-natural/extracted cellulose microfibril and CBM2a-natural/extracted cellulose microfibril interactions, 100 F-D curves were collected at the

loading rate of 100 nN/s for each CBM-cellulose complex. According to Bell's model, a constant force F applied to a distance x_D will lower the energy barrier.[177] The x_D defined here in our study is the energy barrier width larger than which the bond is broken. The E_b here was estimated using $E_b = 1/2\ F_b L$, where F_b is the unbinding force and L is the stretching distance of the non-covalent bond during the unbinding event.[203]

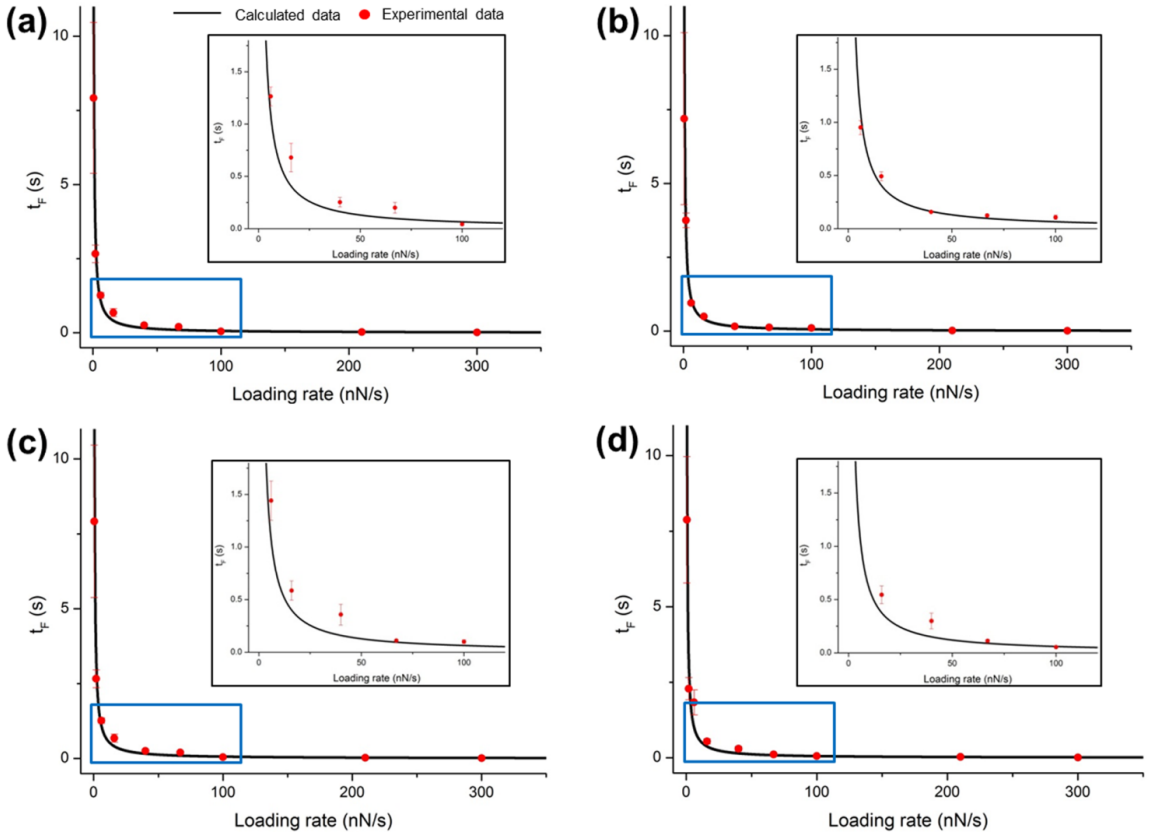

Figure 3.7 Comparisons of calculated (black line) and experimental (red dots) t_F value for CBM-cellulose interaction. (a) CBM3a-extracted cellulose microfibril complex, (b) CBM2a-extracted cellulose microfibril complex, (c) CBM3a-natural cellulose microfibril complex, and (d) CBM2a-natural cellulose microfibril complex.

The kinetic off rate (k_{off}) can provide insight into the occurrence of the bond, bond strength and relaxation time. The k_{off} of CBM-cellulose interaction listed in Table 3.1 is calculated by the linear fitting (red line in Figure 3.6(a)) of unbinding forces before the saturation. The fitted unbinding forces agreed with Bell's one-barrier bond dissociation model.[199] The complete results of calculations are all listed in Table 3.1.

The CBM3a-natural cell wall cellulose complex shows the lowest off rate (with k_{off} of 0.0081 ± 0.0002 s^{-1}) and highest energy barrier (with E_b of 15.12 ± 4.08 kcal/mol) and the CBM2a-extracted cellulose microfibrils show the highest off rate (with k_{off} of 0.0099 ± 0.0008 s^{-1}) and lowest energy barrier (with E_b of 13.73 ± 3.44 kcal/mol). The off rate of CBM-cellulose interactions measured in this study is much larger than that of streptavidin and biotin (1.67×10^{-5} s^{-1}), which is one of the strongest protein-ligand interactions.[204] Therefore this result shows a much weaker interaction between CBM and cellulose. As discussed previously about the free energy changes, the larger CBM3a-celluose contact area enhances the binding process although the differences are still not very significant.

3.4 Conclusions

Different from the bulk experiments, we determined several dynamic and kinetic parameters, such as unbinding forces, reconstructed free energy change, energy barrier, and bond lifetime, to estimate the affinities of the CBMs to natural and extracted cellulose microfibril from a single-molecule perspective. Generally, a CBM3a single molecule has a slightly higher binding efficiency and affinity than the CBM2a molecule to both natural and extracted cellulose surfaces. Both CBMs have higher affinities to the natural cellulose microfibrils compared to the extracted cellulose microfibrils. The bond

lifetime analysis showed the differences of kinetic properties of two CBMs at the single-molecule level. The CBM-cellulose interaction study using SMDFS will offer a radical approach to provide more detailed information on both the plant cell wall degradation and other single molecule interaction systems. With the above established method and conclusions, we are able to take a step further to study the plant cell wall morphology changes during the breakdown process and how to degrade the cell wall in a more efficient and economical way.

CHAPTER 4

STRUCTURAL AND COMPONENT CHANGES OF NATURAL AND PRETREATED PLANT CELL WALL SURFACES

4.1 Introduction

On the way of pursuing renewable and sustainable replacements of crude oil, the lignocellulosic biomass (such as poplar, switchgrass, and corn stover), has been considered as one of the primary feedstocks with potentials of high efficiency and low cost.[3-4, 205-206] To overcome the recalcitrance of the plant cell walls, several pretreatments have been developed to enhance the cellulose degradability.[75, 207-208]

The essential role of pretreatment is to physically and/or chemically disassemble the protective carbohydrate-lignin complex, disrupt the crystalline structure of cellulose in order to increase the surface accessibility of cell wall carbohydrates.[207, 209] Some extensively studied pretreatment technologies include steam explosion,[210-211] ammonia fiber expansion (AFEX),[212] ammonia recycled percolation (ARP),[213] lime,[214] dilute acid pretreatment,[215] etc. Each pretreatment has specific advantages and disadvantages in hemicellulose degradation and lignin removal, but they all have the capacity to change the plant cell wall structure.[75, 216] Dilute acid pretreatment (DAP), specifically dilute sulfuric acid, has received extensive attentions for several decades. Its major objective is to extensively solubilize hemicellulose (over 80% of the natural content) and disrupt the carbohydrate-lignin linkage to enhance the enzymatic digestibility of cellulose.[207, 217-218] Although little lignin is removed, the disruption and re-localization of lignin have been

clearly verified which can slightly increase the exposed surface area of cellulose for hydrolysis.[219-221]

Enzymatic hydrolysis predominantly proceeds from outer surface of the plant cell walls. Extensive surface distribution of hydrolysable components therefore can facilitate the cell wall-enzyme interactions and improve the hydrolysis efficiency. Consequently, an in-depth understanding of structural changes of pretreated cell wall surface, especially at single molecule level, can provide a fundamental insight of cell wall ultrastructure for pretreatment improvement. However, the cell wall structure after pretreatments is completely or partially destroyed, so the chemical changes determined by bulk chemical analysis do not necessarily reflect the real surface conditions. Alternatively, surface characterization techniques such as SEM, TEM, can provide surface morphology information, but do not provide information on chemical composition.[77, 222-223] Fluorescence microscopy[224] and time-of-flight secondary ion mass spectrometry (ToF-SIMS)[225] are also applied in cell wall surface analysis, but the accuracy of component distributions on surface is unsatisfactory due to the limited mapping resolution.

Based on the methods and conclusions from the previous chapters, in the following study, we characterized the natural, dilute sulfuric acid pretreated and delignified plant cell wall surfaces of poplar, switchgrass, and corn stover by AFM recognition imaging using CBM3a-modified AFM tip. The surface structural changes of plant cell walls before and after pretreatments were determined and compared based on the extended concept of recognition area percentage (RAP) on exposed crystalline cellulose.[226]

4.2 Experiments

4.2.1 Dilute sulfuric acid pretreatment of biomass samples

All biomass for pretreatment were ball-milled (8000 M Mixer/Mill, SPEX SamplePrep, Metuchen NJ) and sieved by mesh screen. The sample pieces in size of 200-250 μm were collected, washed by DI water, and dried at 45 ˚C for 24 h. 0.1 g ball-milled biomass of each species was pre-soaked in dilute sulfuric acid (0.03% w/w, 2 mL) (VWR, Radnor, PA) for 30 min in a 20 mL glass pressure tube (Ace Glass Incorporated, Vineland, NJ). The sealed pressure tube was heated in a heating block on a hot plate (Barnstead/Thermolyne-RT Elite, Dubuque, IA) at 135 ˚C for 20 min. The reaction was stopped by cooling down the tube to room temperature in cold DI water. The pretreated sample was then washed by 10 mL DI water for 5 times and centrifuged with 1 mL DI water (5,000 rpm, 10 min) for 5 times (SORVALL BioFuge Pico Microcentrifuge, Thermo Electron Corporation, Waltham, MA) and finally dried in air at 45 ˚C for 24 h. The same procedure was repeated at 135 ˚C for all three species with 0.5% w/w, 1% w/w, and 2% w/w sulfuric acid. The switchgrass and corn stover pretreated in 0.5% w/w sulfuric acid at 160 ˚C (0.095 g H_2SO_4: dry wt, 5 wt.% solids) were provided by the University of California at Riverside. The summary of all pretreatment conditions and sample nominations are compiled in Table 4.1.

Table 4.1 Dilute acid pretreatment conditions of poplar, switchgrass and corn stover.

Species	Sample ID	Solid loading (%)	Temperature (˚C)	Reaction time (min)	Acid loading (g/g dry wt.)
Poplar (P)	Natural-P	-	-	-	-
	0.03%P-135	5%	135	20	0.005
	0.5%P-135	5%	135	20	0.095
	1%P-135	5%	135	20	0.2
	2%P-135	5%	135	20	0.4
Switchgrass (SG)	Natural-SG	-	-	-	-
	0.03%SG-135	5%	135	20	0.005
	0.5%SG-135	5%	135	20	0.095
	1%SG-135	5%	135	20	0.2
	2%SG-135	5%	135	20	0.4
	0.5%SG-160	5%	160	20	0.095
Corn stover (CS)	Natural-CS	-	-	-	-
	0.03%CS-135	5%	135	20	0.005
	0.5%CS-135	5%	135	20	0.095
	1%CS-135	5%	135	20	0.2
	2%CS-135	5%	135	20	0.4
	0.5%CS-160	5%	160	20	0.095

4.2.2 Delignification of dilute acid pretreated biomass samples

The pretreated samples were subsequently delignified following one of the leading methods.[223] Briefly, 0.02 g sodium chlorite (J. T. Baker, Phillipsburg, NJ) and 40 μL glacial acetic acid (VWR, Radnor, PA) was added into each pretreated biomass water slurry (3% solid, 1 mL). The reaction was taken at 80 ˚C for 1.5 h with gentle stirring. After cooling down, the bleached sample was washed 8 times with DI water followed by centrifugation at 10,000 rpm for 10 min and then was dried in air at 45 ˚C for 24 h.

4.2.3 AFM sample preparation and experimental setup

The AFM sample preparation procedure was the same as poplar slice immobilization as described in Chapter 2.[181] All images were taken using TopMAC mode

under PicoTREC (Agilent Technologies, Santa Clara, CA). The 200-500 μm hand-cut, natural pieces of each biomass sample after mesh screening (200-500 μm in size) before pretreatments and pure microcrystalline cellulose Avicel PH-105 (FMC BioPolymer, Philadelphia, PA, nominal particle size: 20 μm) were also imaged. For each sample, about 20 pieces were randomly imaged by the functionalized AFM tip at an average scanning speed of 6 μm/s. 100 recognition images in size of 1 μm×1 μm were randomly selected for the RAP calculation.

4.3 Results and discussions

4.3.1 Surface mapping of natural plant cell walls of poplar, switchgrass, and corn stover

Previously, we visualized and recognized the crystalline cellulose on the surface of natural poplar slice. In the following work, we also characterized the natural cell wall of switchgrass and corn stover. The representative images are shown in Figure 4.1.

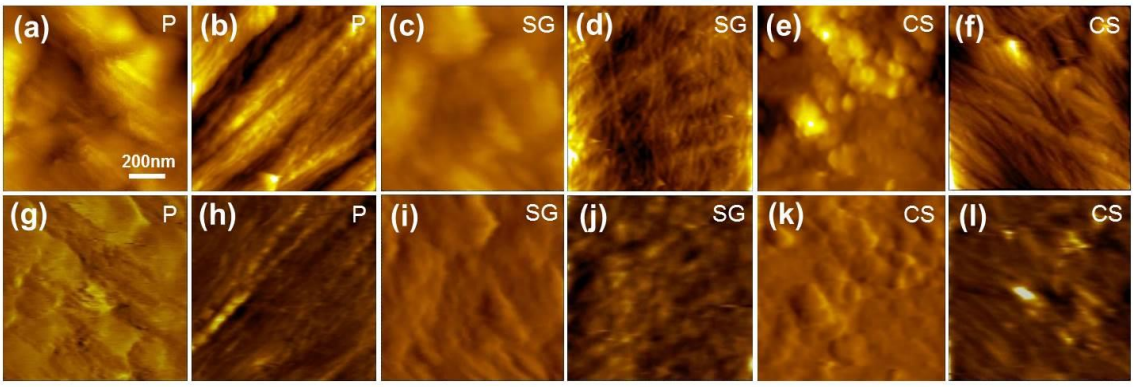

Figure 4.1 AFM topography and recognition images of the natural plant cell walls. Topography (a-f) and recognition (g-l) images of poplar (P), switchgrass (SG), and corn stover (CS). (a, c, e, g, i, k) show the representative surface mainly covered by lignin and (b, d, f, h, j, l) show the representative surface mainly covered by crystalline cellulose.

It has been confirmed that the lignin content in poplar is about 10% higher than that in switchgrass and corn stover.[77, 222] Accordingly, we observed more surface area covered by lignin or lignin-carbohydrate complex on the poplar plant cell wall than on switchgrass and corn stover. Besides, the morphology of poplar lignin exhibited smooth and intact layers while the lignin in switchgrass and corn stover formed irregular and compact granules as shown in the topography images of Figure 4.1(a), (c), and (e). Few surface components of these areas were recognized in the corresponding recognition images of Figure 4.1(g), (i), and (k), indicating the absence of specific interactions between non-cellulose components and CBM3a molecule on the AFM tip. Differently, on surface area extensively covered by parallel or interwoven crystalline cellulose microfibrils in Figure 4.1(b), (d), and (f), strong recognition signals were detected in the corresponding recognition images of Figure 4.1(h), (j), and (l).

4.3.2 Measurement of RAP on plant cell wall surfaces

The crystalline cellulose distributions on the plant cell wall surface were quantitatively determined based on recognition signal distributions. For each biomass sample, 5 different surface areas were imaged on each single piece by the functionalized AFM tip. Over 20 sample pieces were imaged and 100 recognition images in size of 1 μm × 1 μm were randomly selected for the RAP calculation. Generally, all the recognition images of each sample were divided into maximum 7 types based on the surface features represented by RAP of crystalline cellulose. Table 4.2 lists a summary of RAPs of each area type on pretreated and delignified corn stover cell wall surface (sample named as 0.5%CS-135 with 0.5% sulfuric acid concentration pretreated at 135 ˚C).

Table 4.2 Recognition area percentage (RAP) calculation of 0.5%CS-135 and delignified 0.5%CS-135 surface averaged from100 images.
Type A: < 10%; B: 10-20%; C: 20-30%; D: 30-40%; E: 40-50%; F: 50-60; G: > 60%.

Sample ID	Area Type	Image counts	Average RAP (%)	Total RAP (%)
0.5%CS -135	A	6	7.15	27.9
	B	19	17.0	
	C	25	24.7	
	D	28	34.9	
	E	9	44.8	
	F	3	58.5	
	G	0	0	
0.5%CS -135	A	0	0	42.6
delignified	B	0	0	
	C	12	26.7	
	D	21	34.5	
	E	36	43.1	
	F	25	52.4	
	G	6	59.5	

The details of extended definition of RAP and an example of RAP calculation are depicted in Figure 4.2 and Equation 4.1-4.3. A 250 nm × 250 nm area was chosen to highlight the binding sites.

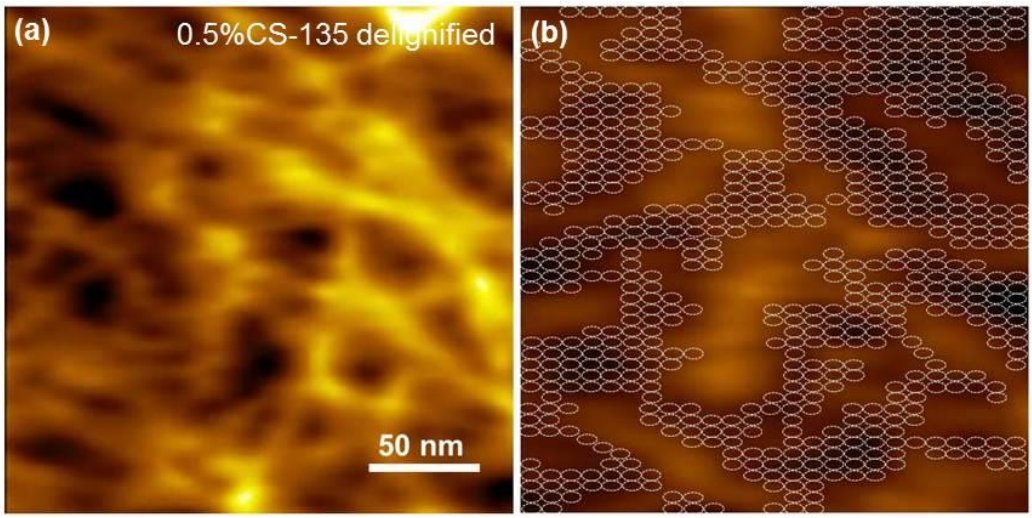

Figure 4.2 Example of recognition area percentage (RAP) calculation on delignified corn stover cell wall pretreated by 0.5% sulfuric acid. (a) Topography image; (b) recognition image. The recognition binding sites are highlighted by white circles.

The RAP of a single recognition was calculated using Equation 4.1:

$$\text{Individual RAP (\%)} = \frac{\text{Recognition area on crystalline cellulose microfibrils (nm}^2\text{)}}{\text{Total surface area of imaged plant cell wall surface (nm}^2\text{)}}$$

Equation 4.1

The average RAP and total RAP were defined in Equation 4.2 and 4.3:

$$\text{Average RAP (\%)} = \frac{\sum \text{Individual RAP of area N}}{\text{Number of area N}} \qquad \text{Equation 4.2}$$

$$\text{Total RAP (\%)} = \frac{\sum \text{Individual RAP of area N}}{100} \qquad \text{Equation 4.3}$$

Here N is the area type (A-G). The recognition area was highlighted as the white circle in the recognition image as shown in Figure 4.2(b). The un-recognized area was supposed to be covered by non-carbohydrate residues, exposed amorphous cellulose or partially twisted crystalline cellulose.

The representative topography and recognition images selected from each area type are shown in Figure 4.3. Based on surface components of pretreated cell wall before and after delignification, the majority of recognition images of 0.5%CS-135 were classified into type A through D, while most of the recognition images of delignified 0.5%CS-135 showed the features of type E-G.

The type A surface was mainly covered by irregularly shaped agglomerates with different sizes, which were mainly supposed to be the re-localized lignin after dilute acid pretreatment (DAP).[221] The RAP of Figure 4.3(h) was lower than 10%, indicating little CBM3a-cellulose interactions. From Type B to G, the amount and size of surface agglomerates gradually decreased and more crystalline cellulose appeared, resulting in an increase of RAPs to over 60%.

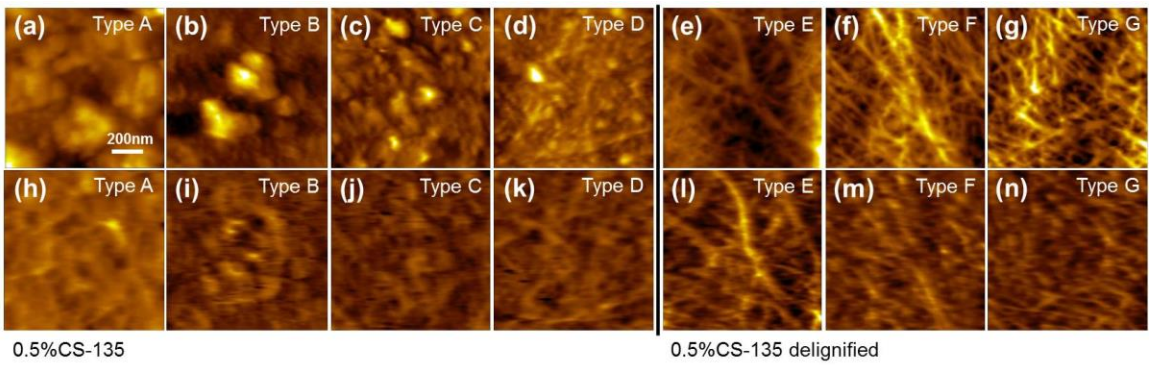

Figure 4.3 Representative topography and recognition images of 0.5%CS-135 and delignified 0.5%CS-135 surface of different area types. (a-g) Topography images; (h-n) recognition images. 0.5%CS-135: corn stover cell wall pretreated by 0.5% sulfuric acid at 135 ˚C.

This difference denoted that the lignin locating on the surface of pretreated plant cell walls was extensively removed during after delignification, therefore the crystalline cellulose underneath was exposed and recognized by the CBM3a-modified AFM tip.[223]

4.3.3 Effect of dilute acid pretreatment under different concentrations

Hydrolysis of hemicellulose is considered as the main reaction during acid pretreatment accompanied by fast condensation and precipitation of solubilized lignin as inevitable physical process.[75, 227] The coalesced lignin deposits back onto the plant cell wall surfaces and potentially blocks further access to cell wall components as observed by SEM and AFM.[221, 228] To quantify the component changes before and after DAP, we compared the surface of natural, dilute acid pretreated and delignified plant cell walls and calculated the RAPs. The plant cell wall surfaces were predominantly covered by lignin sheath, which was unevenly distributed all over the surface (Figure 4.4(a)). Recognition signals can hardly be seen due to the absence of specific CBM3acellulose interactions (Figure 4.4(e)). Remarkably, more crystalline cellulose microfibrils could be seen on the

surface of 0.5%CS-135 sample in Figures 4.4(c) and (g) with higher RAPs than that of poplar (0.5%P-135) and switchgrass (0.5%SG-135) (Figure 4.5). This result demonstrated that the cell wall of corn stover is less recalcitrant to DAP process.

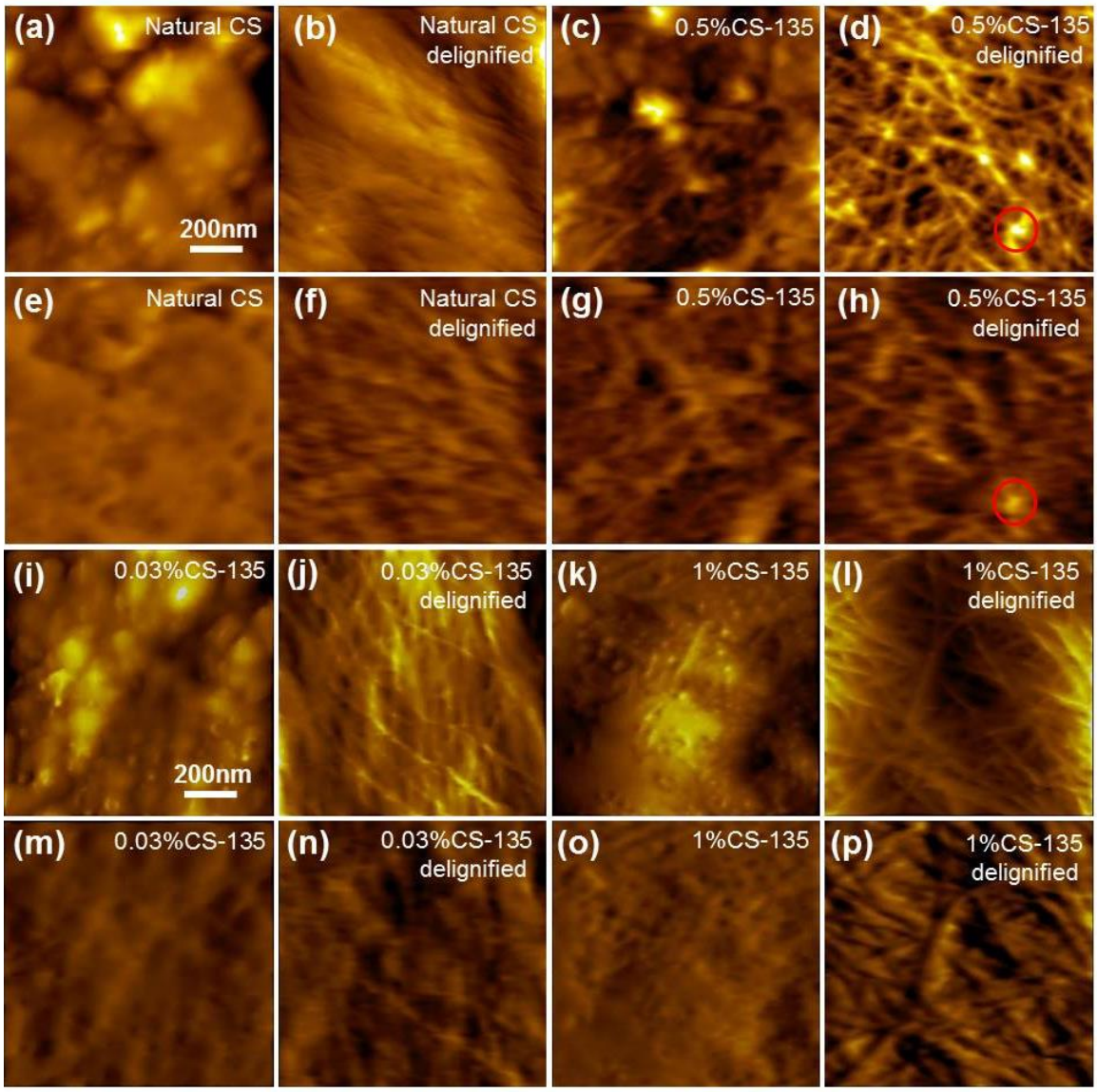

Figure 4.4 Topography and recognition images of natural, dilute acid pretreated, and delignified corn stover cell walls. Topography (a-d, i-l) and recognition (e-h, m-p) images of natural, dilute acid pretreated (pretreated by 0.03%, 0.5%, and 1% sulfuric acid at 135 ˚C) and delignified corn stover cell wall. Some possible residues in (d) which do not have recognitions in (h) are highlighted in the red circles.

To determine the effect of DAP on cell wall surface structural changes other than lignin re-distribution, we removed the lignin by acidified sodium chlorite as shown in Figure 4.4(b, d, f and h). In Figure 4.4(b), the crystalline cellulose exhibited a compact configuration and individual crystalline cellulose microfibrils could hardly be distinguished. Some agglomerates could also be observed in Figure 4.4(d), which were supposed to be lignin residues (marked in red circles) that could not be recognized in Figure 4.4(h). The RAPs of natural and delignified corn stover were measured to be 15.2% and 29.4%, respectively. The RAPs of natural corn stover and switchgrass (RAPs of natural switchgrass increased from 13.6% to 26.1% after delignification) nearly doubled after delignification; meanwhile the RAPs of delignified poplar increased by 70% (RAPs of natural poplar increased from 12.9% to 21.8% after delignification) (Figure 4.5 and 4.6). The less efficient delignification effect on poplar might due to a naturally higher content of intact lignin and a more solid cell wall structure. Comparatively, the surfaces of delignified cell walls after 0.5% sulfuric acid pretreatment at 135 ˚C exhibit a more interrupted and interwoven configuration, especially for corn stover (Figure 4.4(d)) and switchgrass (Figure 4.6(d)). This morphology change was mainly caused by the removal of hemicellulose, therefore the linkage between crystalline cellulose was destroyed and individual crystalline cellulose microfibrils were released. The RAPs of 0.5%CS-135, 0.5%SG-135 and 0.5% P-135 were 27.9%, 20.4%, and 17.4%, respectively. After delignification, the RAPs of dilute acid pretreated corn stover and switchgrass increased by over 50% of their pretreated condition and that of pretreated poplar even doubled (Figure 4.6). The higher cellulose content in natural plant cell walls of poplar also contributed to a more substantial increase of RAP when more re-localized

lignin droplets was removed (Figure 4.6(f)). The surfaces of natural and 0.5% sulfuric acid pretreated poplar and switchgrass cell walls were characterized and the results are shown in Figure 4.5.

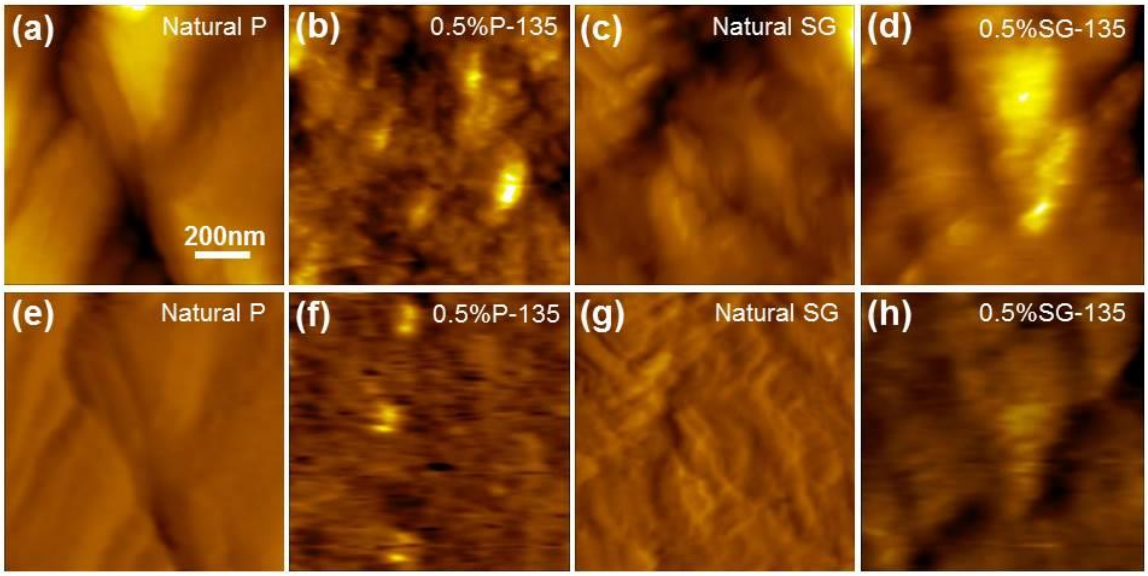

Figure 4.5 Topography (a-d) and recognition (e-h) images of natural and dilute acid pretreated poplar (0.5%P-135) and switchgrass (0.5%SG-135).

The size of lignin agglomerates on poplar cell wall surface was larger than that on switchgrass, showing a more intact solid structure of lignin on poplar cell walls. The RAPs of natural poplar and switchgrass was 12.9% and 13.8%, respectively. After DAP with 0.5% sulfuric acid, the RAPs of poplar and switchgrass increased to 17.4% and 20.4%, respectively.

After delignification, the fine crystalline cellulose structure was exposed and the recognition was largely improved as shown in Figure 4.6.

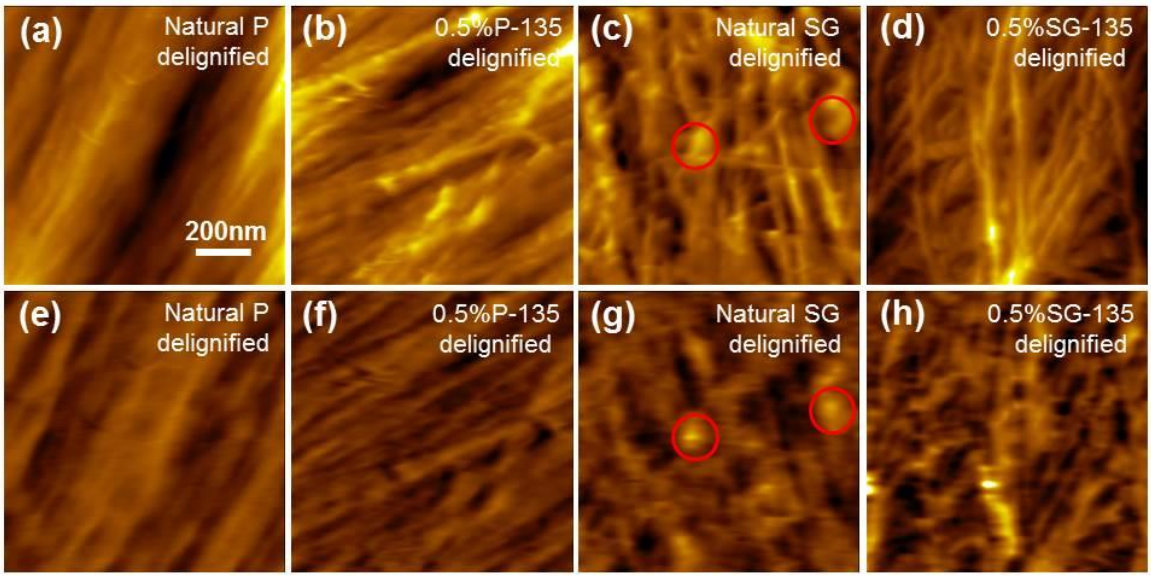

Figure 4.6 Topography (a-d) and recognition (e-h) images of delignified natural and dilute acid pretreated poplar (0.5%P-135) and switchgrass (0.5%SG-135). Residual components or unfavorable position of crystalline cellulose which are not recognized are highlighted in red circles.

For both poplar and switchgrass cell walls before DAP, the surfaces after delignification were majorly composed of crystalline cellulose together with other un-removed, linking matrix components (e.g., hemicellulose). Some representative non-cellulose components which were not recognized were marked in red circles. The RAPs of delignified poplar and switchgrass without DAP were 21.7% and 26.1%, respectively. With 0.5% acid pretreatment, the RAPs of poplar and switchgrass increased to 32.3% and 33.1%. The delignified switchgrass cell wall structure showed more interwoven crystalline cellulose than those of poplar.

Various DAP conditions (e.g., altering temperature, acid concentration, reaction time, etc.) have been investigated to optimize the pretreatment results for better cell wall degradability.[76] The hemicellulose removal and re-localization of lignin are proved to be

more pronounced with stronger acid or higher reaction temperature.[75, 221] In the following work, we quantitatively studied the surface structural changes during DAP under different acid concentrations (i.e., 0.03%, 0.5%, 1%, and 2%). The corn stover surface structural changes after 0.03% and 1% DAP can be clearly seen in Figure 4.4(i and k). The AFM images of poplar and switchgrass cell walls pretreated by 0.03% and 1% sulfuric acid are shown in Figure 4.7. The size of agglomerates formed on cell wall surfaces after 0.03% DAP was larger than that observed on surfaces pretreated by 1% acid, especially on 0.03%P-135 and 0.03%SG-135 (Figure 4.7). The re-localized lignin was assumed to overlay the cell wall surfaces more evenly under high acid concentration and thereby reduce the RAPs.[220-221] Some hemicellulose re-precipitated onto the cell wall surfaces under lower acid concentrations was also presumed to reduce the RAPs.[220]

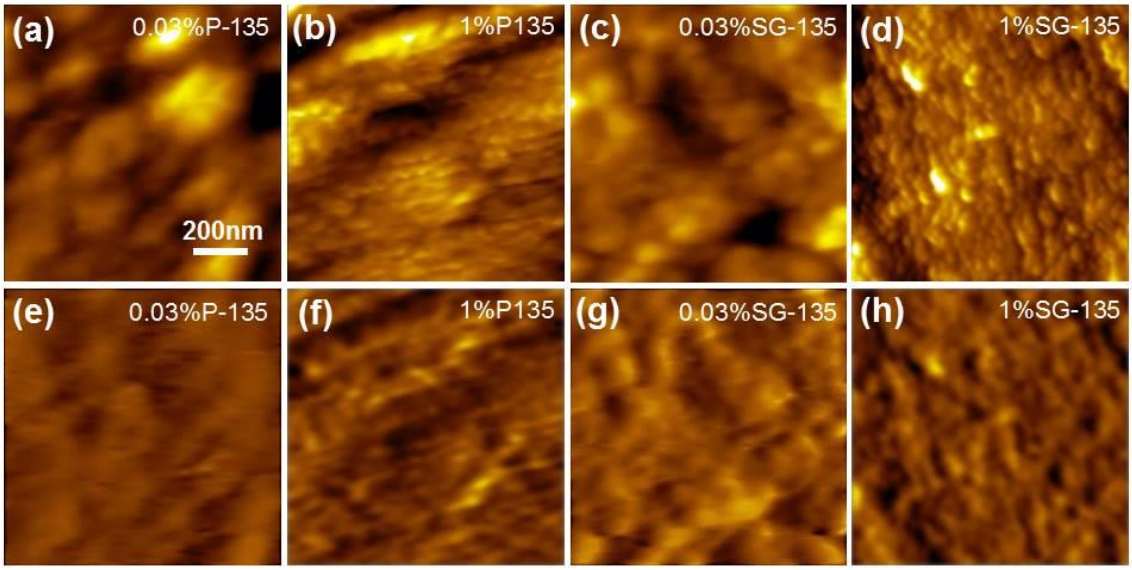

Figure 4.7 Topography (a-d) and recognition (e-h) images of dilute acid pretreated poplar (0.03%P-135 and 1%P-135) and switchgrass (0.03%SG-135 and 1%SG -135) cell walls.

To further understand the effect of acid concentrations on hemicellulose removal, we also removed the surface lignin to see the compositional changes underneath. Figure 4.8 shows the topography and recognition images of the above pretreated poplar and switchgrass cell walls after delignification. In Figure 4.4(j), the exposed crystalline cellulose on 0.03%CS- 135 presented some interwoven arrangement, similar to the morphology observed on 0.03%SG-135 (Figure 4.8(c)); while the exposed crystalline cellulose exhibits a more intact, parallel structure on 0.03% P-135 (Figure 4.8(a)). Moreover, less surface components were recognized on 0.03% P-135 (Figure 4.8(e)) than on 0.03%SG-135 (Figure 4.7(g)) and 0.03%CS-135 in Figure 4.4(n). Therefore, the surface of delignified 0.03%P-135 was expected to be covered by a large amount of hemicellulose, denoting a less effective removal of this component. When the cell walls of corn stover were previously pretreated with stronger acid, e.g., 1% or 2% acid, a denser, more regular crystalline cellulose structure were exposed after delignification (Figure 4.4(l)) and the corresponding recognition area also greatly increased (Figure 4.4(p)). The similar results were also observed on the delignified poplar and switchgrass (Figure 4.8(b) and (d)).

Under higher acid concentrations, the lignin residues were smaller in size but covered the cell wall surface more evenly therefore reduced the recognition area and RAPs. The RAPs of pretreated poplar decreased from 14.8% (0.03%P-135) to 13.5% (1%P-135) and the RAPs of switchgrass decreased from 17.3% of 0.03%SG-135 to 15.2% of 1%SG-135.

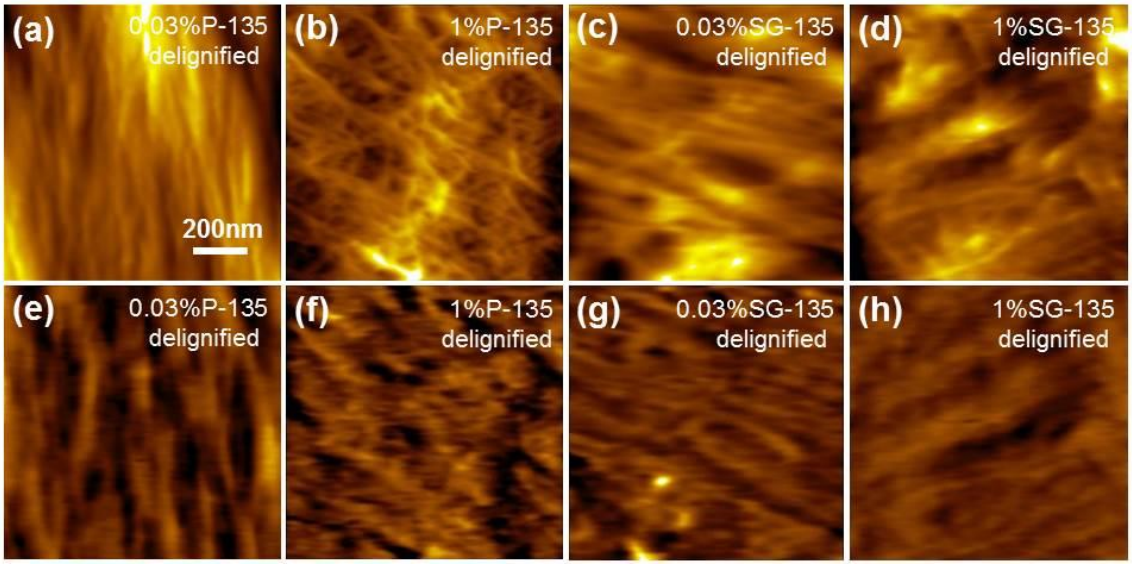

Figure 4.8 Topography (a-d) and recognition (e-h) images of delignified, dilute acid pretreated poplar (0.03%P-135 and 1%P-135) and switchgrass (0.03%SG-135 and 1%SG-135) cell walls.

It can be clearly seen that the cell wall pretreated with higher acid concentration showed a more interwoven morphology, indicating a more efficient removal of hemicellulose. The RAPs of delignified cell walls after DAP increased from 29.4% (0.03%P-135) to 41.2% (1%P-135) for poplar and increased from 31.1% (0.03%SG-135) to 43.8% (1%SG-135) for switchgrass. This result again demonstrated a better effect of hemicellulose removal under higher acid concentration.

Additionally, the cell walls of poplar, switchgrass, and corn stover pretreated by 2% acid were also characterized and the representative images are shown in Figure 4.9. The cell walls of all species pretreated with 2% acid showed well-distributed small lignin agglomerates and cross-linking crystalline cellulose morphology after delignification. The RAPs of 2%P-135, 2%SG-135 and 2%CS-135 increased from 13.2%, 16.8% and 16.2% to 41.9%, 42.6% and 47.5%, respectively after delignification.

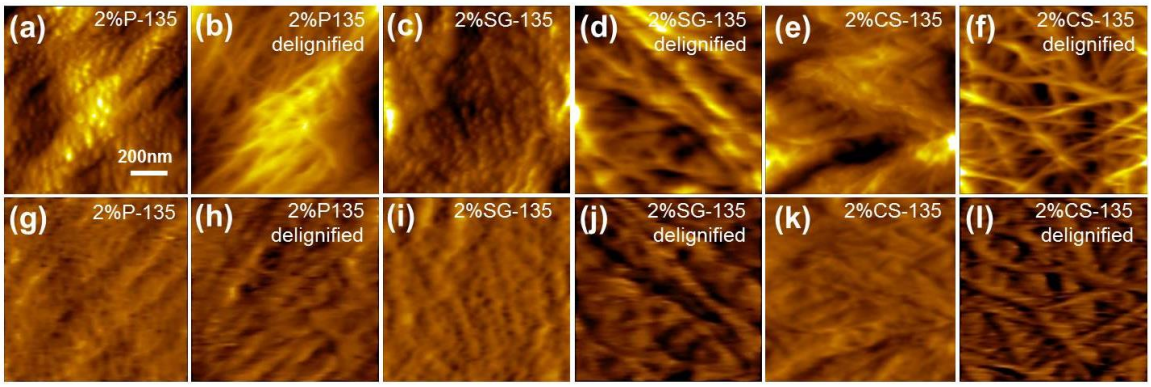

Figure 4.9 Topography (a-f) and recognition (g-l) images of dilute acid pretreated and delignified poplar (2%P-135), switchgrass (2%SG-135) and corn stover (2%CS-135) cell walls.

Similarly, the RAPs of 0.03%CS-135 and 1%CS-135 were determined to be 19.4% and 15.9%, respectively. The RAPs of 0.03%P-135 and 0.03%SG-135 also decreased from 14.8% to 13.5% and 17.3% to 15.2%, respectively when compared with 1%P-135 and 1%SG-135. The results demonstrated that the RAPs decreased with a higher acid concentration which caused more extensive and even lignin coverage by smaller lignin droplets and corn stover exhibited better accessibility. After delignification, the RAP of 0.03%CS-135 was 35.3% and the RAP of 1%CS-135 became 50.8%. The RAPs of delignified poplar and switchgrass also showed the same trend, i.e., the RAPs of poplar increased from 29.4% (0.03%P-135) to 41.2% (1%P-135), while the RAPs of switchgrass increased from 31.1% (0.03%SG-135) to 43.8% (1%SG-135) (Figure 4.8). Hence, compared with 0.03% acid, cell wall pretreatment with 1% acid exhibited 6-12% more surface accessibility of crystalline cellulose by dissolving more hemicellulose, although the surface lignin was hardly removed. Notably, the polymerization of the crystalline cellulose was also affected under the high acid concentration by inducing the

decrease of microfibril length as shown in Figure 4.4(d) and (l), therefore more reducing-ends were supposed to be produced.

To sum up, the dilute acid pretreatment effectively dissolve hemicellulose but showed no pronounced removal of lignin, at least on the outer surface of plant cell wall. The plant cell wall was also deconstructed due to removal of hemicellulose and lignin after delignification. The corn stover cell wall showed less recalcitrance compared to poplar and switchgrass.

4.3.4 Area type distributions and RAP summary of natural and pretreated plant cell walls

As an average value, however, RAP cannot tell the differences of surface conditions before and after pretreatments. For instance, the RAP of natural corn stover is 15.2%, which is very close to the RAPs of 1%CS-135 (15.9%) and 2%CS-135 (16.2%). However, it doesn't necessarily mean that the surface component distributions are the same. To explore the changes of plant cell wall structures, the number of recognition images in each area type was counted and the results were compiled in Figure 4.10.

The distributions in Figure 4.10(a) clearly manifested that for natural corn stover, more than half of the surface structures were defined as type A and B and about one fourth of the recognitions images showed the features of type E and F. The crystalline cellulose in natural plant cell walls were highly ordered, lacking the favorable position for specific CBM binding, therefore the recognized area was quite limited and the RAP cannot reach to over 60% as defined in type G. After DAP, over 60% of surface features were grouped in type B and C, indicating a slight interruption of lignin coverage and higher crystalline cellulose accessibility. Remarkably, for 0.5%CS-135, the majority of recognition images located in type C and D, which also gave a much higher RAP value

and exhibited a more evenly distributed crystalline cellulose. Similar results could also be obtained on poplar and switchgrass.

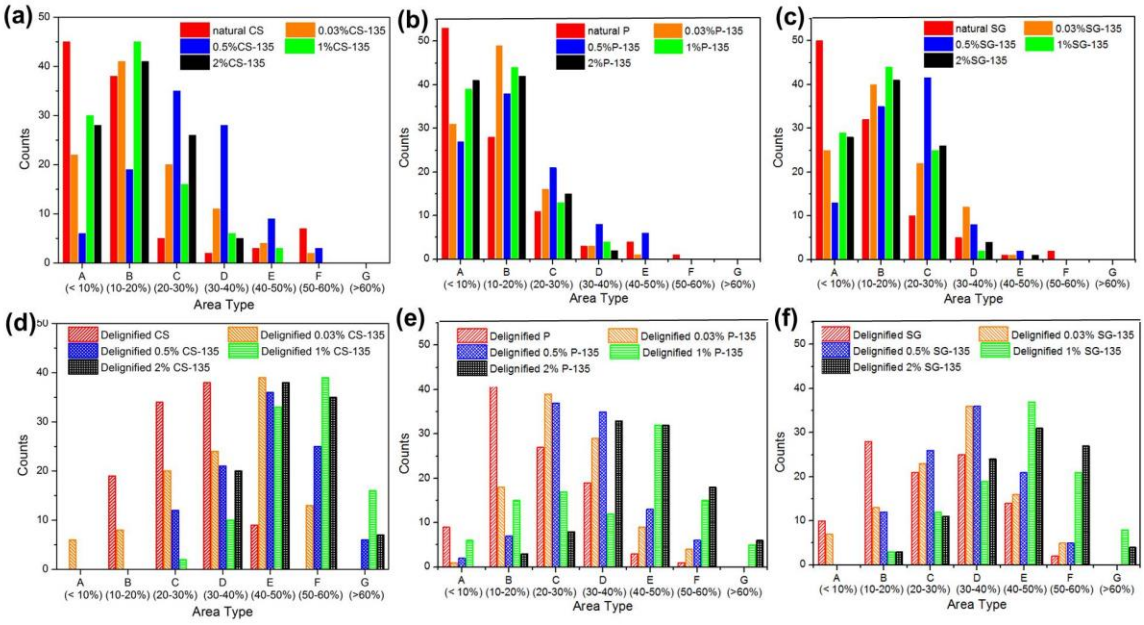

Figure 4.10 Area type distributions. (a, b, c) Area type distributions of natural and dilute acid pretreated cell wall surfaces of corn stover, poplar and switchgrass; (d, e, f) Area type distributions of delignified cell wall surfaces of corn stover, poplar and switchgrass.

Figure 4.10(b, c, e and f) reveals diverse distributions of recognition images of natural and dilute acid pretreated poplar and switchgrass. Similar to corn stover, for natural poplar and switchgrass, more than half of the surface morphologies were located in type A and B. After DAP with 0.03%, 0.5%, 1% and 2% dilute acid, the more cell wall surfaces showed the features in type C and D. After delignification, the surfaces of dilute acid pretreated cell walls showed more features determined as type D through G and the majority of recognition images of natural samples were determined as type A though D.

After removal of lignin, the image distributions changed evidently as shown in Figure 4.10(d, e, f). The area types distributed more widely and more surface features were determined as type D through G. For delignified corn stover before DAP, for instance, more than half of the images areas revealed features of type C and D, whereas the majority of surface features of 0.03%CS-135, 1%CS-135, and 2%CS-135 were determined as type D through F. Some areas classified as type G, especially on 2%CS-135, validated a more effective removal of hemicellulose under higher acid concentration.

Due to the limitation of high scan speed during imaging, surface roughness and unfavorable position of crystalline cellulose for binding, the recognition efficiency and accuracy are supposed to have their own limitations.[149, 229] Therefore, to reflect more accurate surface crystalline cellulose distributions, we used Avicel as a control to calibrate the RAPs. The RAP of Avicel, a commercial product containing up to 97% of microcrystalline cellulose, was measured to be 72.1% (Figure 4.11).

The surface of Avicel was full covered by short microcrystalline cellulose fibrils and over 70% of the surface components were recognized in Figure 4.11(b). More than 90 recognition images showed the features of type G (with RAP > 60%) as shown in Figure 4.11(c). Hence the recognition efficiency was simply defined as 72.1% / 97% = 74.3%. After calibration, we summarized the new RAPs obtained under different acid concentrations at 135 ˚C into Figure 4.11(d).

Figure 4.11(d) illustrates a direct view of RAPs measured on all biomass species under different pretreatment conditions. After DAP, the RAPs of poplar, switchgrass, and corn stover increased slightly and reached a highest value when the acid concentration was 0.5% and then decreased.

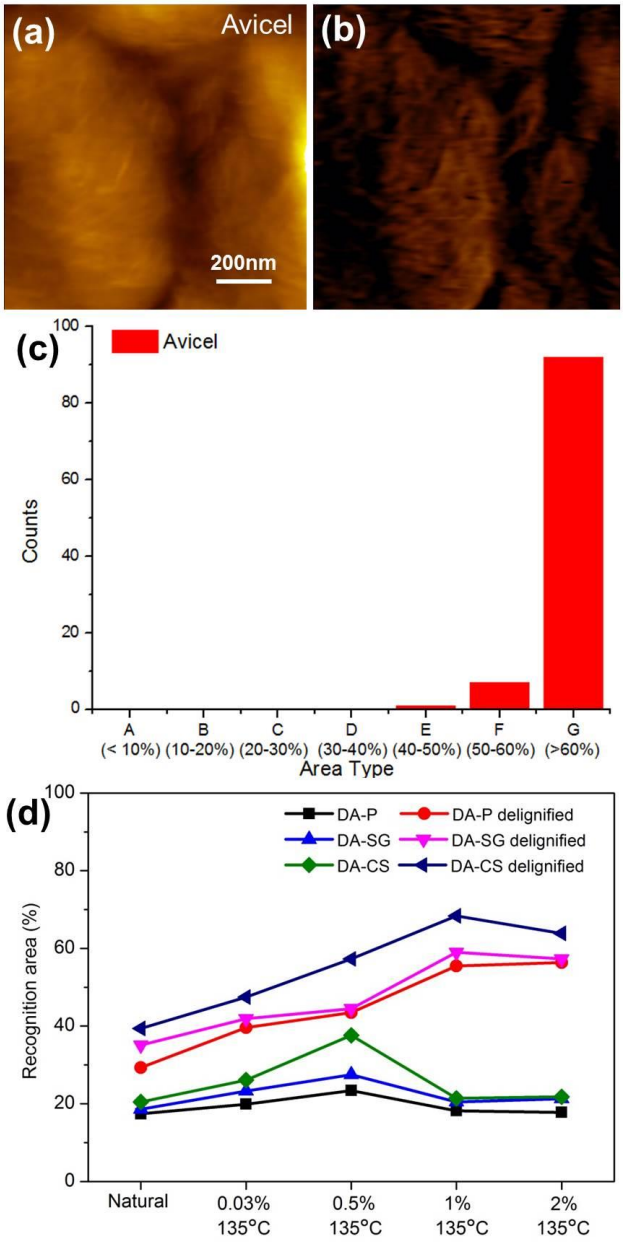

Figure 4.11 Recognition area percentage (RAP) calibration and summary. Topography (a) and recognition (b) images of pure microcrystalline cellulose (Avicel). The area type distribution of Avicel surfaces are shown in (c). (d) RAP summary of natural and pretreated poplar, switchgrass, and corn stover cell wall surfaces.

At the acid concentration higher than 1%, the surface structure was supposed to have less correlation to the acid concentration and no further improvement of RAPs was

observed. With 0.5% DAP, the cell wall deconstruction, hemicellulose removal, and lignin re-precipitation reached to a balance point so that the crystalline cellulose skeleton was exposed to a maximum level with the highest RAP. After delignification, however, the RAPs could be correlated to acid concentration up to 2%. When the surface lignin droplets were nearly completely removed, the blocking effect was greatly eliminated and the cell walls pretreated under higher acid concentrations presented more interrupted structures with more binding-favorable positions of crystalline cellulose. A slight decrease of RAPs in switchgrass and corn stover pretreated by 2% acid could be attributed to a more evident effect of depolymerization of crystalline cellulose, lower surface density of surface crystalline cellulose microfibrils due to extensive removal of hemicellulose or partial generation and deposition of pseudo-lignin.[230-231]

In summary, the RAPs after calibration indicated that the increasing acid concentration caused more effective removal of hemicellulose on all plant cell wall surfaces; meanwhile the surface coverage of re-precipitated lignin droplets reduced slightly and then intensified with highest RAP at 0.5% acid. The surface chemical components changes were further qualitatively determined by grazing angle attenuated total reflectance Fourier transform infrared spectroscopy (ATR-FTIR). The spectra of poplar, as an example, indicated a conclusion similar to RAP results (Figure 4.12).

FTIR measurements were taken with a Nicolet Model 6700 spectrometer (Thermo Electron Corporation, Waltham, MA) with a grazing angle attenuated total reflectance accessory. Spectra were obtained with 4 cm^{-1} resolution at 64 scans for both the background and samples. After drying, the sample was pressed against the Ge hemispherical ATR crystal surface by a build-in pressure applicator (Harrick Scientific

Products, Inc. Pleasantville, NY). The representative spectra of each poplar sample are shown in Figure 4.12 below.

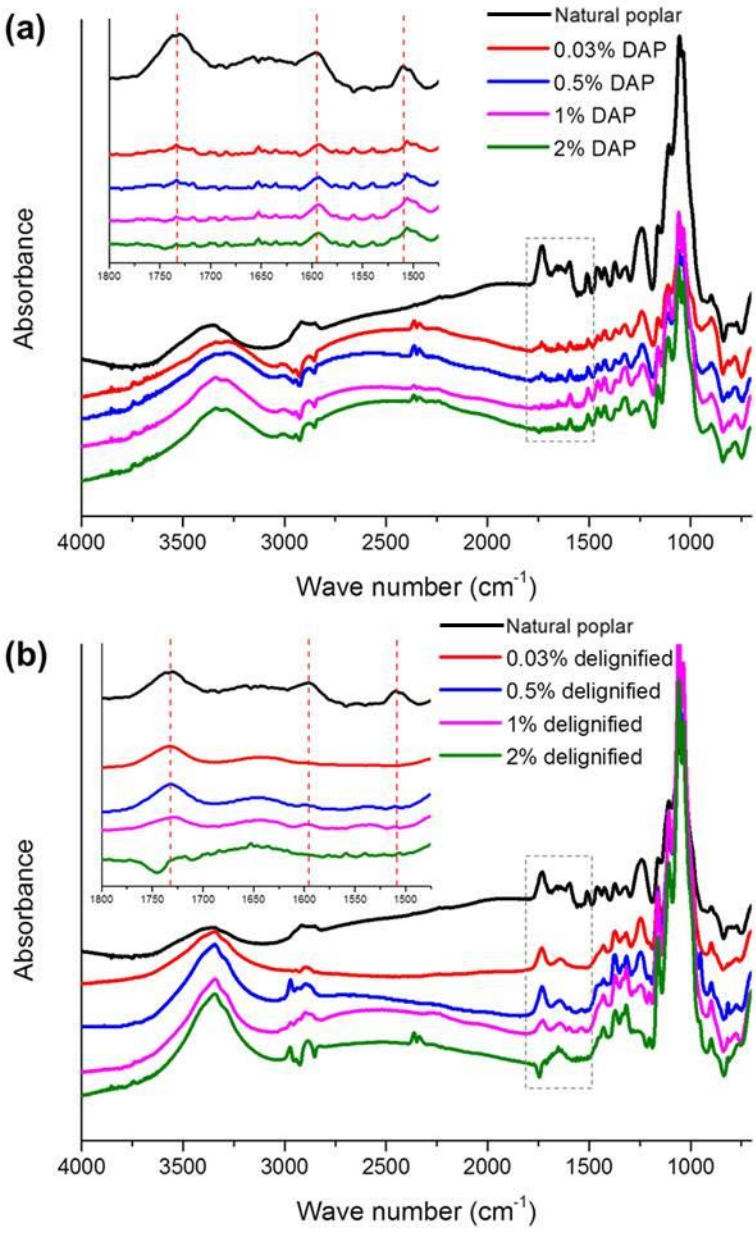

Figure 4.12 ATR-FTIR spectra of natural, dilute acid pretreated (a) and deliginified (b) poplar cell wall surface.

In Figure 4.12, the ATR-FTIR spectra show the chemical component changes of dilute acid pretreated poplar cell wall surface. The inset from the dashed, grey square highlights the surface content changes of hemicellulose and lignin. The dashed, red lines highlight the positions of the bands at 1732 cm^{-1} (ascribed to carbonyl group, indicating hydrolysis of hemicellulose and cleavage of lignin side chains), 1595 cm^{-1} and 1510 cm^{-1} (ascribed to aromatic skeletal vibrations of lignin).[77, 223, 232] The spectra showed an obvious decrease of hemicellulose and slight decrease of lignin in peaks. For sample pretreated by 1% and 2% acid, the surface content of lignin started to slightly increase, indicating a possibility of more extensive surface coverage of lignin which agreed with the AFM recognition result.

After delignification, the lignin on the cell wall surface almost disappeared and the decrease of hemicellulose under higher acid concentration is more pronounced as previously determined by RAP result (Figure 4.12(b)).

4.3.5 Effect of dilute acid pretreatment under different temperatures

DAP under high temperatures (130 ˚C-220 ˚C) was considered to highly improve plant cell wall deconstruction.[221] According to Moxley *et al.*,[220] cellulose accessibility was closely correlated to hemicellulose solubilization at lower pretreatment temperatures; at higher temperatures, however, lignin degradation has a better correlation with cellulose accessibility. Here we compared the surface structural changes of corn stover and switchgrass cell walls pretreated by 0.5% acid at 135 ˚C and 160 ˚C. Figure 4.13(a, c) reveal re-deposited lignin droplets on the cell wall surfaces. Notably, the droplet on surfaces of 0.5%CS-135 was slightly larger than that on surfaces of 0.5%CS-160. This

difference could be attributed to depolymerization and translocation of lignin under higher pretreatment temperature.[221]

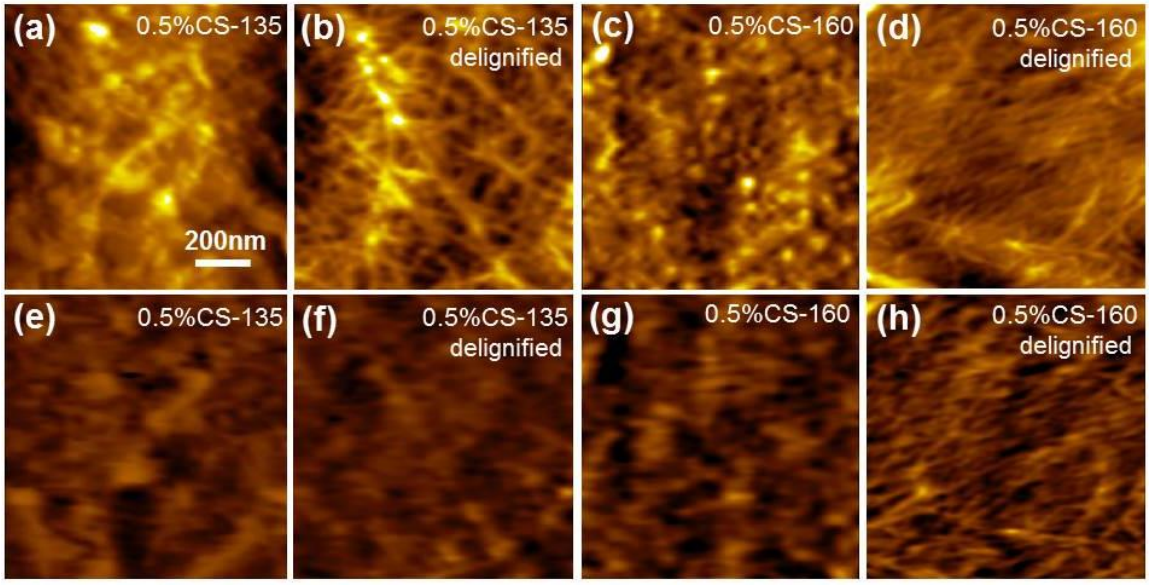

Figure 4.13 Topography and recognition images of corn stover pretreated by 0.5% dilute acid at 135 ˚C and 160 ˚C and after delignification. (a-d) Topography images; (e-h) recognition images. 0.5%CS-135, corn stover cell wall pretreated by 0.5% sulfuric acid at 135 ˚C; 0.5%CS-160, corn stover cell wall pretreated by 0.5% sulfuric acid at 160 ˚C.

After delignification, the deconstructed cell wall surfaces were fully exposed with features of parallel and interwoven crystalline cellulose. As shown in Figure 4.13(b, d) and Figure 4.14, the crystalline cellulose microfibrils on surfaces of 0.5%CS-160 and 0.5% SG-160 were better separated than those on surfaces of 0.5%CS-135 and 0.5%SG-135, depicting a more in-depth and delicate removal of hemicellulose among individual cellulose microfibrils.

The topography and recognition images of switchgrass pretreated by 0.5% acid under 135 ˚C and 160 ˚C are shown in Figure 4.14. Similar to corn stover, the re-

precipitated lignin agglomerates on surface of dilute acid pretreated switchgrass decreased under higher reaction temperature and the RAPs also increased slightly from 27.5% to 28.5% (after calibration, the same for the following RAPs). After removal of lignin, the crystalline cellulose underneath showed more fine structure and was better separated under higher pretreatment temperature with the increase of RAP from 44.5% to 47.8%.

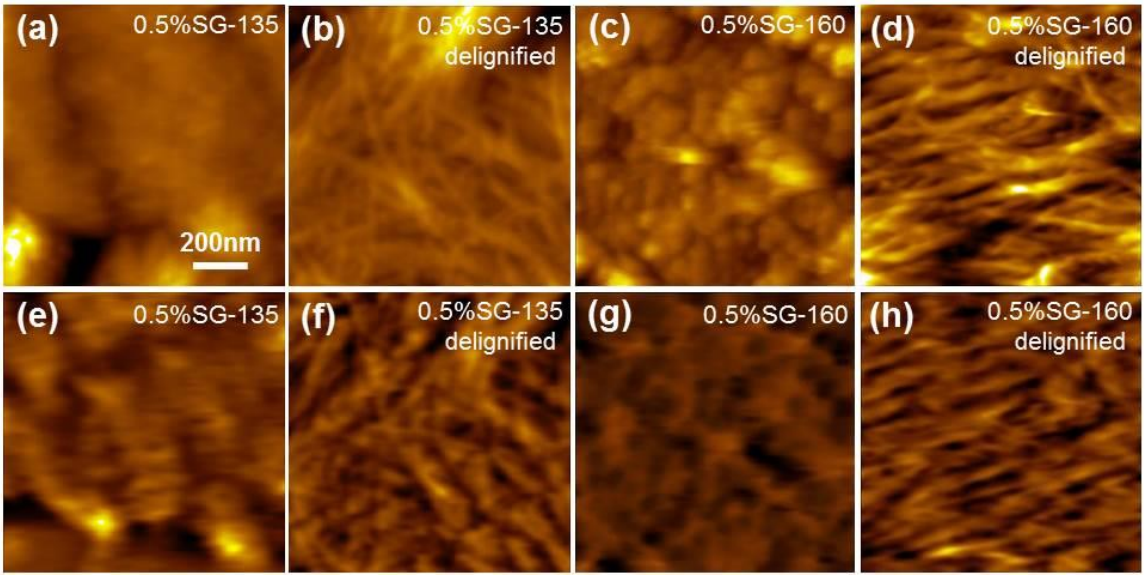

Figure 4.14 Topography (a-d) and recognition (e-h) images of switchgrass pretreated by 0.5% dilute acid at 135 ˚C and 160 ˚C and after delignification (0.5%SG-135 and 0.5%SG-160).

The recognition signals in Figure 4.13(h) also showed more delicate distribution compared with that in Figure 4.13(f). On the other hand, 0.5%SG-135 and 0.5%CS-135 showed the RAPs of 27.5% and 37.6%, respectively (after calibration, the same for the following RAPs). These values were slightly lower than the RAPs of 0.5%SG-160

(28.5%) and 0.5%CS-160 (39.9%). Corn stover cell walls again seemed to be more sensitive to higher temperature. Accordingly, the RAPs of delignified 0.5% SG-135 and 0.5%CS-135 were measured to be 44.5% and 57.3%, respectively, lower than the RAPs of 0.5%SG-160 (47.8%) and 0.5%CS-160 (61.1%) respectively. Therefore, DAP under higher temperature revealed a higher efficiency in plant cell wall deconstruction, especially for corn stover.

4.4 Conclusions

Based on AFM recognition imaging and area percentage calculations, the results showed that 17-20% of plant cell wall surfaces were covered by crystalline cellulose before pretreatment. This coverage increased to 23-38% after dilute acid pretreatment under different temperature and acid concentrations. When the plant cell walls were pretreated with 0.5% sulfuric acid, the crystalline cellulose surface distribution of 23% on poplar, 28% on switchgrass, and 38% on corn stover was determined as an optimized result at 135 ˚C. Compared to bulk component analysis, this method exhibits pronounced advantages in providing detailed surface information of plant cell walls.

CHAPTER 5

BINDING KINETICS OF CBM WITH CRYSTALLINE CELLULOSE UNDER AN OPTIMIZED CONDITION

5.1 Introduction

The CBM binding can guide the movement of intact cellulase molecules on cellulose surface; hence the binding equilibrium is important for understanding hydrolysis process. In the intact cellulolytic enzyme molecule, CBM has been presumed to be responsible for the apparently irreversible binding, rather than the catalytic domain.[13, 233] The adsorption of CBMs is therefore required to be fully understood and well-controlled.[234]

In the past decades, bulk experimental measurements quantitatively revealed a wide range of affinities of different CBMs binding to various cellulose substrates under a series of temperature.[139, 141, 235-238] In 1996, Linder and Teeri studied the kinetics of binding of the CBM from *Trichoderma reesei* cellobiohydrolase I on microcrystalline cellulose based on binding isotherm data.[234] In this work, free CBM molecules (100 μL, 20 μM) were incubated with the same volume of bacterial microcrystalline cellulose (2 mg/mL) for 3 h. Binding affinity of the CBM was found to increase at lower temperatures. The exchange rate measured for the CBM-cellulose interaction compared well with the hydrolysis rate of cellobiohydrolase I with $k_{off} = 0.012 \pm 0.0025$ s^{-1} at 22 ˚C. McLean and co-workers extended the CBM species and cellulose substrates in 2002 to identify the specificities of different CBMs to different cellulose structures by competition isotherms and fluorescent labeling.[142] The adsorption isotherms were obtained by incubating 2-20

μM of competing fluorescence-labeled CBM species with cellulose substrates (1 mg/mL) for 3 h at 4 ˚C. The surface and solution concentrations of each CBM were monitored as a function of time and composition. A very fine binding specificity of cellulose-specific CBMs was determined down to the resolution of cellulose microstructures. This research provided a comprehensive understanding of how an enormous number of CBM molecules from different enzyme species bound to the carbohydrate substrates competitively and the specificity of each CBM was quantitatively determined. However, the complicated labeling procedure and averaged kinetic values made the measurement of binding efficiency down to the single CBM molecule impossible.

In this project, we studied the binding process of the CBM-cellulose interaction on extracted crystalline cellulose of poplar monitored by AFM topography and recognition images. CBM3a molecules were used for both AFM tip functionalization and free CBM molecule binding under a series of concentrations. We also observed the distribution of bound CBMs on cellulose sample surface and determined the binding kinetics by a single-molecule kinetics model, which is based on counting the surface concentrations of CBM3a-cellulose complexes along the reaction time. Consequently, a minimal effective initial concentration of CBM3a was determined at a comparatively short reaction time using this kinetics model.[239]

5.2 Experiments

5.2.1 Preparation of extracted plant cell wall cellulose and AFM sample

The extraction of crystalline cellulose fibrils were depicted in Chapter 3.[119, 196] To prepare the AFM sample for recognition imaging and binding sites calculation, the

extracted poplar suspension (0.1% wt, 20 μL) was dropped onto the cleaned glass surface. After 20 min, the glass surface was washed by 200 μL purified water five times to remove extra cellulose that had weak adsorption to glass. Finally, the air-dried glass chip was fixed into an AFM flow cell and then filled with 0.4 mL Tris-Cl buffer (10 mM Tris-Cl and 150 mM NaCl, pH=7.5) for recognition imaging and binding site calculation.

5.2.2 AFM experimental setup

The PicoPlus system combined with an Agilent 5500 Controller was used in this work. After obtaining repeatable AFM images of extracted crystalline cellulose within the same scanned area, the CBM3a solution in 100 μL Tris-Cl buffer was gently injected into the flow cell. The CBM3a concentrations used in this work were 3.38 μM, 2.37 μM, 1.20 μM, 0.5 μM, 0.3 μM, 0.2 μM, and 0.1 μM. The binding process of CBM3a onto crystalline cellulose was then monitored in the following 3-8 h.

5.2.3 Binding sites calculation by AFM recognition imaging

Under each CBM3a concentration, the binding experiment was repeated 3 times. The binding sites were calculated in a 300 nm × 300 nm scanned area, and 5 randomly selected locations on sample surface were used to obtain the images with the same scan size in order to obtain averaged results. The functionalized AFM tip was set at a scanning speed of 6 μm/s. AFM recognition images have been used to calculated the RAP in our previous work.[196, 226] To study the kinetics of CBM3a binding process, the numbers (or concentrations) of available binding sites on cellulose sample surface were counted from individual binding site, which was estimated as 5 nm in width with 5-8 nm interval along a single crystalline cellulose fibril.[181] Both the total binding sites at the beginning of

reaction and the unoccupied binding sites after a certain reaction time (which were converted into the numbers of formed CBM-cellulose complex) were calculated from the AFM images with 300 nm × 300 nm scanned area.

5.3 Results and discussions

5.3.1 Binding of CBM3a to crystalline cellulose

The schematics of CBM3a gradually binding to crystalline cellulose is shown in Figure 5.1. The CBM3a molecule functionalized on the AFM tip was induced to interact with the crystalline cellulose on substrate during scanning. A series of recognition signals could be generated at the supposed binding sites along each crystalline cellulose fibril. The binding kinetics study was based on the initial concentrations of free CBM3a, the number of estimated available or initial binding sites on cellulose surface at the beginning of reaction, and the time-dependent formation of CBM-cellulose complex along the binding reaction course (Figure 5.1). The number of estimated binding sites was defined as the total number of binding sites located on the entire crystalline cellulose sample surface (300 nm × 300 nm scanned area). The interval between two adjacent binding sites was measured to be 5 to 8 nm.[181]

The crystalline cellulose surface with and without CBM binding was illustrated by AFM topography (Figure 5.2(a, b)) and recognition (Figure 5.2(c, d)) images. After injecting the CBM3a solution, the binding sites were gradually blocked by the free CBM molecules in solution; therefore, the number of available binding sites decreased. When coverage of the CBM3a molecules on the crystalline cellulose surface became saturated, most binding sites were blocked.

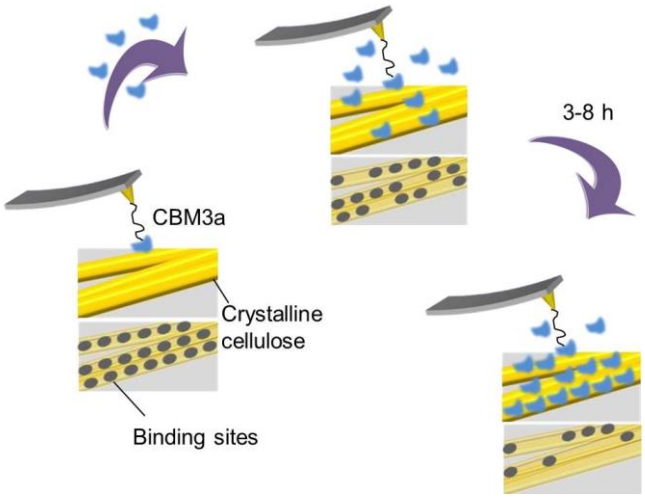

Figure 5.1 Schematics of blocking of binding sites on crystalline cellulose after injection of free CBM3a molecules.

The number (or concentration) of the CBM3a-crystalline cellulose complexes could be calculated by subtracting the number (or concentration) of un-blocked binding sites (Figure5.2(h)) from the total number of estimated available (initial) binding sites (Figure 5.2(g)). Therefore, the number of bound CBM3a-crystalline cellulose complexes was estimated to be 15 -20 along a 200 nm fibril.

A representative crystalline cellulose fibril of diameter 20-25 nm was labeled by a white line along the axis. The cross-section along the white line was analyzed to show the difference of the surface morphology before and after CBM binding (Figure 5.2(e-h)). Before injecting the CBM3a solution, the surface of cellulose was comparatively rough with numerous binding sites available, as labeled by red dashed lines with the intervals of 5-15 nm in Figure 5.2(g). At 180 min after injection of 3.38 μM of CBM3a, more small features appeared on the surface of cellulose fibril, which were supposed to be individual CBM3a molecules aligning along the cellulose fibrils. Therefore, the number of binding

sites greatly decreased (less red dashed lines in Figure 5.2(h)), indicating the blocking of binding sites by free CBM molecules. The blue boxes in Figure 5.2(g) and (h) highlight the details of the change in binding sites between 0 min and 180 min within a distance of 200 nm on cellulose fibril surface. Base on the observation of 15 crystalline cellulose fibrils, the average blockage ratio of the binding sites at 180 min was around 70-80% under this relatively high CBM concentration of 3.38 μM.

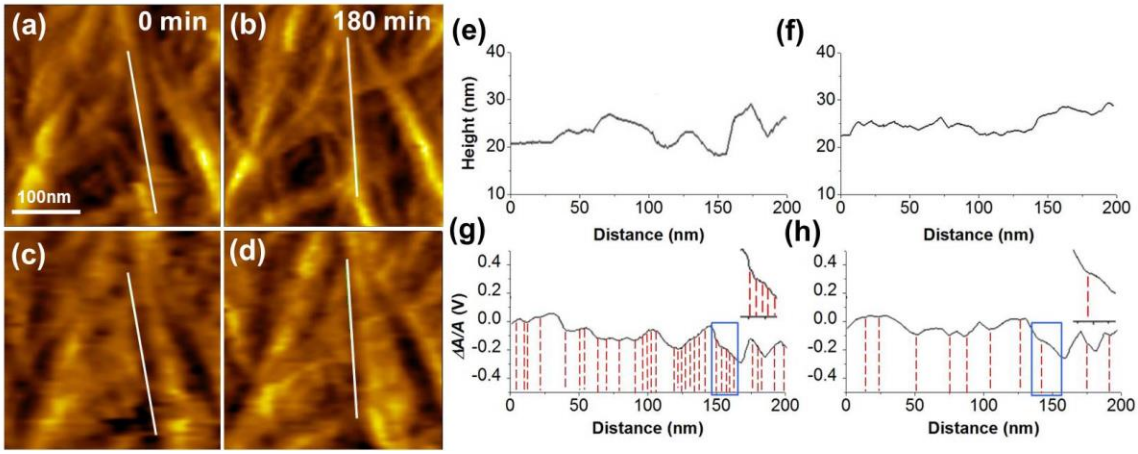

Figure 5.2 *In-situ* AFM recognition imaging of cellulose microfibrils and binding site analysis. (a, b) Topography and (c, d) recognition images of crystalline cellulose fibril before (0 min) and after (180 min) presence of free CBM molecules (3.38 μM). The white lines label the topography (e, f) and recognition (g, h) cross-section of a single cellulose fibril. The red, dashed lines highlighted the individual binding sites before and after the blocking by free CBM molecules. The blue boxes indicate the differences of binding sites at 0 min and 180 min on a certain location of that cellulose fibril.

To reveal the details of CBM binding process and the changes of cellulose surface morphology along the reaction time, a series of AFM topography and recognition images were collected with the initial CBM3a concentration of 0.2 μM, as an example. Figure 5.3 shows the images obtained at 0 min, 30 min, 120 min, and 300 min after injection of

CBM3a solution. The cellulose surface morphology and the change of the binding sites were also revealed by cross-section analysis.

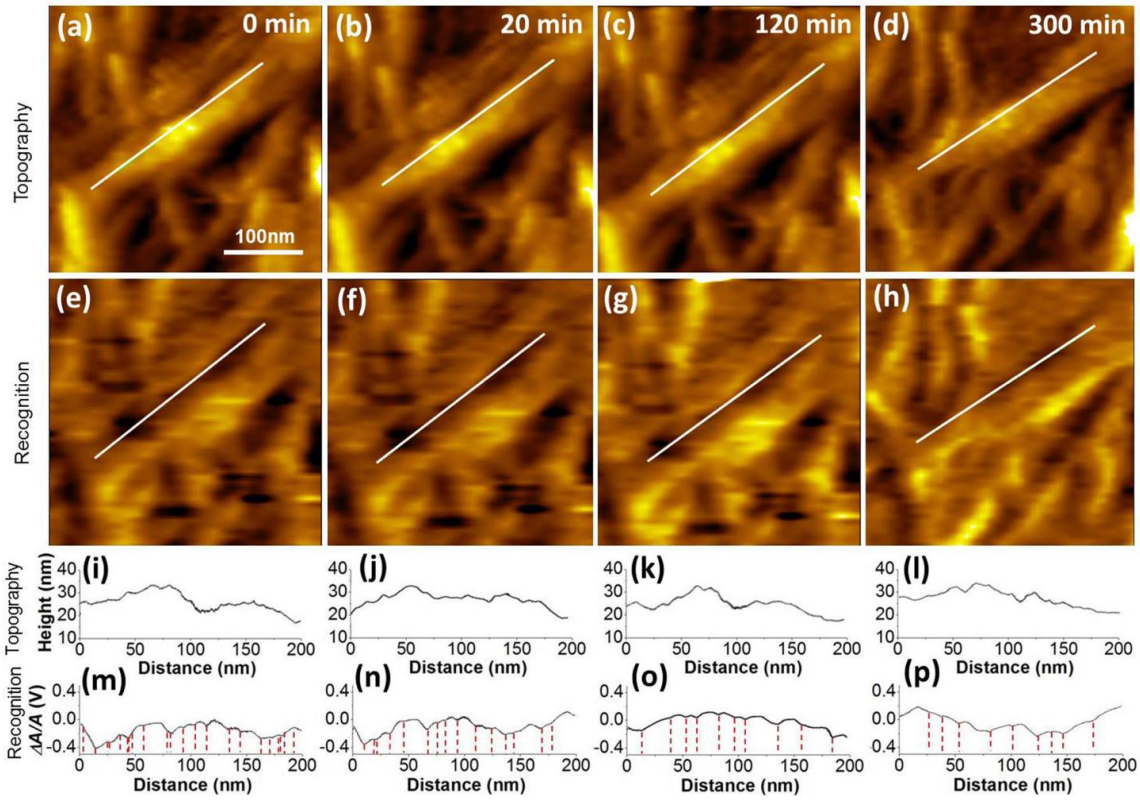

Figure 5.3 Timeline of CBM3a binding to crystalline cellulose. (a-d) Topography images; (e-h) recognition images; (i-l) cross-sections of topography images along the white lines; (m-p) cross-sections of recognition images along the white lines. Some representative binding sites are label with dashed red lines.

With the presence of CBM3a molecules, the surface of each crystalline cellulose fibril was gradually covered by CBM (Figure 5.3(a-d)). Simultaneously, more and more small features appeared along the cellulose fibril (Figure 5.3(a-d)). About 20 small "bumps" with the diameter of ~5 nm were observed at 300 min along the fibril labeled by

the white line, suggesting the regular alignment of CBM3a molecules (Figure 5.3(i-l)). Besides, the number of representative binding sites decreased from about 22 to 9 after 300 min reaction (Figure 5.3(e-h) and (m-p)), indicating a weaker and nonspecific interaction between the CBM3a on AFM tip and cellulose due to blocking of binding sites. Different from the results with the higher CBM concentration, the average blockage of binding sites reduced to 60-70% after saturated binding at 300 min under this lower concentration of CBMs.

Different from bulk experiment, we were able to directly observe the time-dependent alignment of individual CBM3a molecule along a single cellulose fibril at a smaller scale in AFM images (Figure 5.4). In topography images (Figure 5.4(a-d)), the morphology of the cellulose fibril kept changing and a highly regular pattern was finally observed along the fibril after 300 min, indicating the binding of increasing number of CBM molecules onto cellulose as indicated by the blue arrows. The recognition images (Figure 5.4(e-h)) showed a clearer trend of decreasing number of binding sites (highlighted by white dashed circles) due to the surface coverage of free CBM molecules.

The 3D images (Figure 5.4(i-l)) also provided the binding and alignment details of individual CBM molecule along cellulose fibril. After 120 min reaction, the CBM molecules on cellulose fibril began to show a regular pattern until the formation of a well-arranged alignment of nine “bumps” at 300 min (indicated by blue arrows in Figure 5.4(b-d) and (j-l)). Notably, the changes of the surface morphology and binding sites were significant during the first 120 min, but ones between 120 min and 300 min were not pronounced. This difference implied that the CBM-cellulose binding happened faster in the first 1 to 2 h then slowed down until saturation.

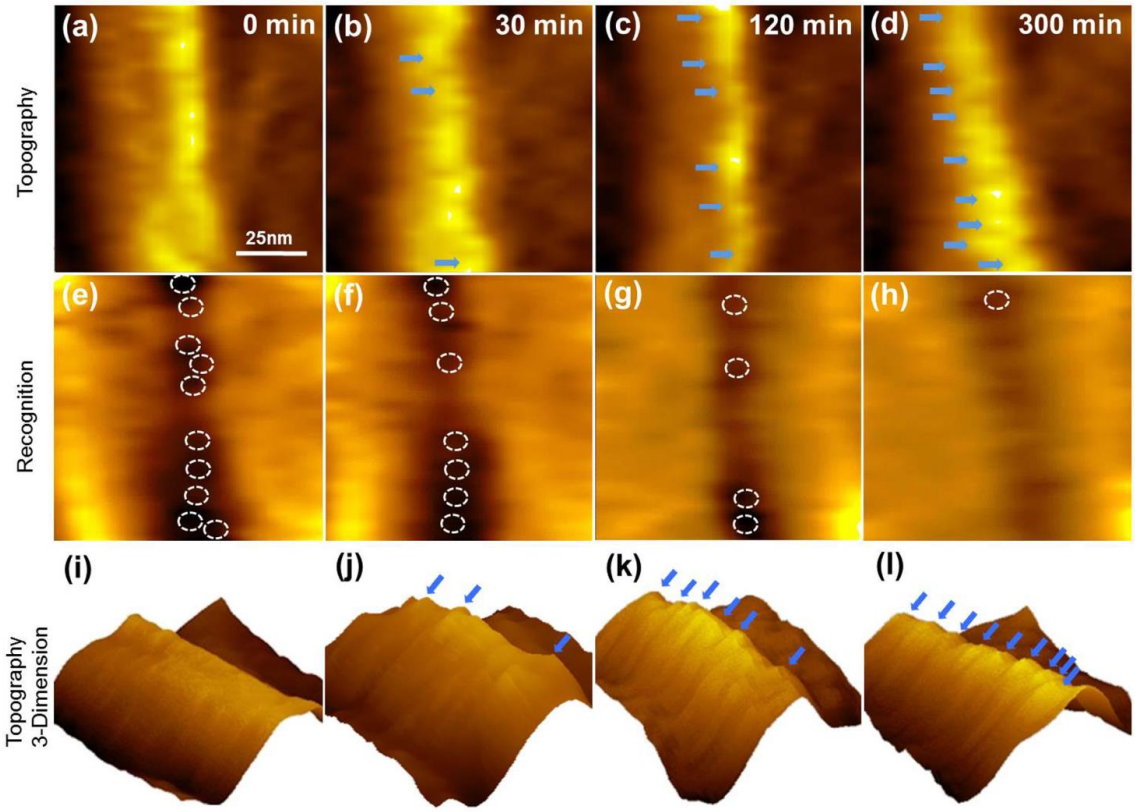

Figure 5.4 AFM topography (a-d), recognition (e-h) and 3D (i-l) images of CBM3a-cellulose binding at a smaller scale. The blue arrows in (b-d) and (j-l) indicate the regularly aligned CBM3a molecules binding on a crystalline cellulose fibril from 0 min to 300 min. The binding sites are labeled by white, dashed circles.

The same situation was also found in Figure 5.3(k, l, o and p). The above observations provided important information of the binding behavior of CBM3a molecule. The binding efficiencies of CBM at different stages of time could lead to a more profound insight into the enzymatic hydrolysis process.

5.3.2 Binding kinetics study and determination of minimal effective initial concentration

To quantitatively determine the binding process of CBM3a to cellulose, we also studied the reaction kinetics of CBM3a-cellulose interaction. The CBM3a binding

reaction mechanism was based on a 1:1 single-molecule surface reaction model for the CBM3a and cellulose molecules. The CBM3a-cellulose interaction process can be expressed as follows:[173]

$$\text{CBM3a}(M) + \text{cellulose}(C) < \frac{k_{on}}{k_{off}} > \text{binding complex}(MC) \qquad \text{Equation 5.1}$$

Here, M is the concentration of injected CBM3a molecules; C is the concentration of estimated initial binding sites on the cellulose surface; MC is the concentration of CBM3a-cellulose binding complex at time t on the sample surface. The calculations of C and MC were described in detail in Table 5.1. The initial concentration of CBM3a (M_0) was considered constant during the entire reaction course if excess of CBM3a molecules were added, compared to the relatively small concentration of cellulose (C_0) on the substrate surface.

The average counts and concentrations of binding sites and bound CBM-cellulose complexes of a full 300 nm × 300 nm scanned area are summarized in Table 5.1.

Table 5.1 The average counts and concentrations of available binding sites and bound CBM-cellulose complexes at different reaction time. The average number of initial binding sites is 180 on a 300 nm × 300 nm scanned area.

Time (min)	Counts of available binding sites	C (M)	Counts of bound CBM-cellulose complexes	MC (M)
0	180	4.6644 E^{-9}	0	0
30	157	4.0684 E^{-9}	23	5.9601 E^{-10}
120	109	2.8245 E^{-9}	71	1.8399 E^{-9}
300	74	1.9176 E^{-9}	106	2.7468 E^{-9}

After the initial binding sites on cellulose in the scanned area were blocked by CBM3a molecules and reached to a saturation state, $MC(t)$ became a constant value $MC(\infty)$ (Equation 5.2 and 5.3).

The classic reaction rate can be expressed as follows:

$$\frac{\mathrm{d}MC}{\mathrm{d}t} = k_{\mathrm{on}}(C_0 - MC)M_0 - k_{\mathrm{off}}MC(t) \qquad \text{Equation 5.2}$$

Here *MC(t)* is the concentration of binding complex at time *t* on sample surface, C_0 is the initial concentration of cellulose on sample surface. The initial concentration of CBM3a *(M_0)* can be considered as constant during entire reaction curse if excess of CBM3a molecules were added compared to the relatively small number of cellulose molecules (C_0) on sample surface.[173] Therefore, the concentration of binding complex *MC(t)* can be solved as

$$MC(t) = \frac{k_{\mathrm{on}}M_0C_0}{k_{\mathrm{on}}M_0 + k_{\mathrm{off}}} \cdot [1 - e^{-(k_{\mathrm{on}}M_0 + k_{\mathrm{off}})t}] \qquad \text{Equation 5.3}$$

Here M_0 was determined at the beginning of reaction, *MC(t)* values were obtained by counting the numbers of binding molecules from the AFM images along reaction time.

With the dissociation constant k_{off} estimated by the Bell's model from single-molecule unbinding force measurements,[177, 196] the on rate k_{on} could also be determined from the relationship below (Equation 5.4):

$$k_{\mathrm{on}} = \frac{MC(\infty)k_{\mathrm{off}}}{M_0[C_0 - MC(\infty)]} \qquad \text{Equation 5.4}$$

Here, both the initial binding sites on cellulose molecules C_0 and the final binding complex *MC(∞)* were counted based on the AFM images. With the k_{off} value estimated from single-molecule unbinding force measurements,[196] the dissociation constant k_{d} value was also calculated from the k_{on} and k_{off} (Equation 5.5):

$$k_{\mathrm{d}} = \frac{k_{\mathrm{off}}}{k_{\mathrm{on}}} \qquad \text{Equation 5.5}$$

To better understand the specific process of CBM3a-cellulose interactions, seven different M_0 values (3.38 μM, 2.37 μM, 1.20 μM, 0.5 μM, 0.3 μM, 0.2 μM and 0.1 μM) were used to obtain the real-time reaction curve. The fitting curves based on Equation 5.2 were compared with their corresponding experimental data points (Figure 5.5). Here, the CBM3a concentrations were converted from the numbers of molecules counted in each AFM image along reaction time t. The saturation time $t_{(0.99)}$ was defined as the reaction time when the concentration of occupied binding sites is 99% of the maximum bound CBM3a concentration at the end of reaction (see the fitting curves in Figure 5.5).

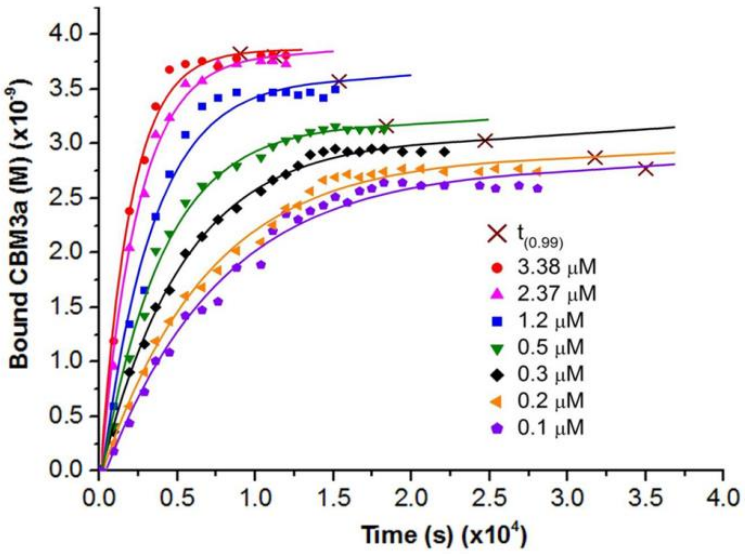

Figure 5.5 CBM3a against reaction time plots for different initial concentrations of CBM3a (M_0). $t_{(0.99)}$ is the saturation time when the concentration of occupied binding sites is 99% of the maximum bound CBM3a concentration at the end of reaction.

The value of $t_{(0.99)}$ at each concentration was calculated from its corresponding fitting curve, and highlighted as cross marks on the fitting curve of each M_0 concentration in Figure 5.5. The k_d values also depended on the M_0 concentrations. When M_0 increased, both $MC(\infty)$ and k_d increased in the binding process (Table 5.2).

Table 5.2 The calculations of k_d values from k_{off} and k_{on} at different initial concentrations of CBM (M_0).

M_0 (μM)	3.38	2.37	1.20	0.50	0.30	0.20	0.10
k_{on}($s^{-1}M^{-1}$)	1.68×10^4	2.18×10^4	2.97×10^4	4.97×10^4	5.88×10^4	7.37×10^4	12.73×10^4
k_{off} (s^{-1})	0.0089	0.0089	0.0089	0.0089	0.0089	0.0089	0.0089
k_d (μM)	0.53	0.41	0.31	0.20	0.15	0.12	0.07

Both M_0 and t showed the exponential relationships with the binding complex concentration MC (Equation 5.6). According to Equation 5.4, the relationships among $MC(t)$, M_0, and t were complicated and deserve more study. Because the values of $k_{on,}M_0$ were always larger than the k_{off} values,[196] the k_{off} term was ignored from Equation 5.4, and the simplified equation is:

$$MC(t) = C_0(1 - e^{-k_{on}M_0 t}) \qquad \text{Equation 5.6}$$

Therefore, both M_0 and t showed the exponential relationships with the binding complex concentration $MC(t)$.

Then the relationship between M_0 and t can be expressed as

$$t_{(0.99)} = \frac{\ln[C_0 MC_{(0.99)}]}{-k_{on}M_0} \qquad \text{Equation 5.7}$$

Here $MC_{(0.99)}$ represents the saturation binding complex concentration at saturation time $t_{(0.99)}$. The plots of $t_{(0.99)}$ against M_0 are shown below in Figure 5.6. The saturation time significantly decreased when initial CBM3a concentration increased. According to Equation 5.7, the initial CBM3a concentration M_0 and saturation time $t_{(0.99)}$ had a simple

reciprocal relationship if the change of saturation complex concentration, the *MC* value at $t_{(0.99)}$, could be neglected.

According to the work of Lee *et al*., the values of k_{off}, k_{on}, and k_d obtained from the force spectroscopy approach (force measurements of k_{off} based on Bell's model and subsequent application of Equation 5.3 to solve only k_{on} from recognition images) differed by a best fit of the entirety of the competitive inhibition data.[173] The distribution was not expected to be homogeneous due to non-ideal mixing of the injected solution. Therefore, the binding rate was assumed to lag behind the estimation in Equation 5.3 under an ideal-mixing condition. This was also confirmed by Equation 5.3 with k_{off} determined from force spectroscopy. Thereby, the binding kinetics could be determined more realistically using force spectroscopy in real experiments.

Figure 5.6 showed the plot of $t_{(0.99)}$ against M_0 and the trend of these data points was very close to a reciprocal relationship. However, when M_0 decreased in the experiments, the value of saturation complex concentration (marked as brown cross for each M_0 value in Figure 5.5) gradually decreased. Therefore, the saturation time $t_{(0.99)}$ was determined by both initial CBM3a concentration M_0 and measured complex concentration $MC_{(0.99)}$. Strictly speaking, the relationship between $t_{(0.99)}$ and M_0 was more complex than a highly simplified reciprocal fitting curve.

In the experimental analysis, we aimed to obtain a minimal effective initial CBM3a concentration M_0 so that the binding reaction could reach saturation with a reasonable $t_{(0.99)}$. Here, linear fittings were used for the four data points in the left part and three data points in the right part of Figure 5.6. The intersection of these two fitting line showed the minimal effective initial CBM3a concentration and its corresponding

saturation time $t_{(0.99)}$. Based on this estimation, the initial CBM3a concentration should be 5.1×10^{-7} M and the saturation time will be 17200 second or 287 min. If the purpose was to obtain shorter saturation time, further increasing of CBM3a initial concentration would not be efficient any more. On the other hand, the CBM3a initial concentrations lower than 5.1×10^{-7} M would dramatically increase the reaction time to reach binding saturation on the cellulose surface. The 5.1×10^{-7} M should be an economic value for the CBM3a-cellulose surface binding reaction.

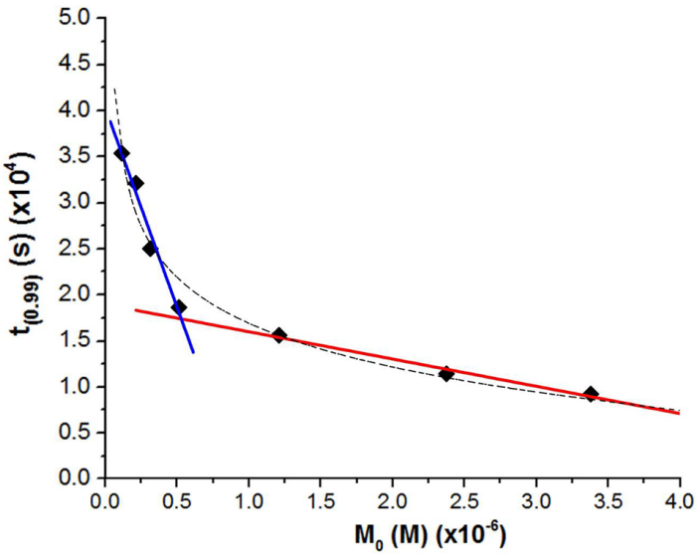

Figure 5.6 Plot of $t_{(0.99)}$ against a series of M_0. Data-points determined by low M_0 and high $t_{(0.99)}$ are fitted by blue line and data-points determined by high M_0 and low $t_{(0.99)}$ are fitted by red line. Trend of the changes of $t_{(0.99)}$ is guided by the dashed black line. The point near intersection indicates the minimal effective initial concentration of M_0 (around 5.1×10^{-7} M).

Other literature reported the reaction times of CBM3a-cellulose interaction with various criteria and methods.[48, 240] For instance, Goldstein and co-workers reported that a

plateau value of 1.2 μM complex was attained by 60 min with 2 μM CBM incubated with 1 mg/mL Avicel.[236] Besides, the measured complex concentration dropped to around half of the maximum value after prolonged incubation of 18 h. This was assumed to be caused by gradual denaturation of the CBMs or by disrupted cellulose surface during non-hydrolytic processes according to Din *et al.*[241] Our single-molecule measurements provided important information about the reaction process as well as time at the nanometer scale. It is well known that the binding kinetics can differ widely among cellulose sample preparations, surface immobilizations, reaction temperatures, and so forth. Thus the very close agreement between bulk experiment and single molecule measurement was not expected in this study. In our work, we used small CBM molecules to study only the binding process and kinetics of CBM-cellulose interaction. When a larger enzyme molecule is used, a different and more complex hydrolysis process is expected to be observed with different binding sites distribution and changes of counts in a time course.

5.4 Conclusions

The free CBM3a molecules of different concentrations were observed to bind to crystalline cellulose efficiently and regularly, especially in the first 120 min. Single-molecule kinetics revealed the detailed relationships among the real-time CBM3a concentration on cellulose surface, reaction time, and initial CBM3a concentration in solution. The saturation time when the concentration of occupied binding sites is 99% of the maximum bound CBM3a concentration, $t_{(0.99)}$, was determined by the AFM recognition images and kinetic model we used in this study. The minimal effective initial CBM3a concentration was found to be 5.1×10^{-7} M at a comparatively short reaction time

of 287 min when the reaction time and initial CBM3a concentration were considered as critical conditions in the experiments. The single-molecule kinetics used in this study was based on large amounts of AFM experimental results and can guide the future experiments on similar reaction systems.

CHAPTER 6

SUMMARY AND OUTLOOK

6.1 Summary

The binding of CBM to cellulose plays an important role in plant cell wall degradation by cellulolytic enzymes. Different from the information provided by bulk experiments, the above studies provided new information on binding kinetics of CBM binding to crystalline cellulose down to the single molecule level by AFM recognition imaging and dynamic force spectroscopy.

a. Binding of CBM3a to natural crystalline cellulose was visualized and measured at single molecule level by *in situ* real-time AFM imaging and SMDFS. The GNP-CBM3a complexes bound to the cellulose surface, closely aligning along the cellulose fibril axis. The unbinding force was measured to be 44.96 ± 18.80 pN under a loading rate of 67.2 nN/s. The binding of CBM3a to crystalline cellulose was determined to be specific and fast.

b. The binding efficiency of both CBM3a and CBM2a to cellulose was determined by the recognition area percentage (RAP) on the crystalline cellulose fibrils surface using AFM recognition imaging. Some important dynamic and kinetic parameters, namely the unbinding forces, reconstructed free energy change, energy barrier and bond lifetime constant, were quantified using SMDFS, which illuminated the affinities of CBMs binding to natural and single cellulose surface from a totally different aspect.

c. The structural changes, specifically on crystalline cellulose, of natural, dilute sulfuric acid pretreated and delignified cell wall surfaces of poplar, switchgrass, and corn stover were determined using AFM recognition imaging. The surface structural changes were studied at single molecule level based on the RAP of exposed crystalline cellulose over the imaged cell wall surface. The results showed that the cell wall surface crystalline cellulose coverage increased from 17-20% to 18-40% after dilute acid pretreatment at 135 ˚C under different acid concentrations and reached to 40-70% after delignification. Corn stover cell walls also showed less recalcitrance due to more effective pretreatments and delignification compared to poplar and switchgrass. The optimal acid concentration was determined to be 0.5% acid at 135 ˚C, especially for corn stover. This study provides a better understanding of surface structural changes after pretreatment such as lignin relocation, re-precipitation, and crystalline cellulose distribution, and can lead to potential improvements of biomass pretreatment.

d. The CBM molecules with different concentrations were observed to bind to cellulose efficiently and regularly, especially in the first 60-120 min. The saturation time $t_{(0.99)}$, when the concentration of occupied binding sites is 99% of the maximum bound CBM3a concentration at the end of reaction, was determined by fitting different concentrations of CBM3a against reaction time. The minimal effective initial CBM3a concentration was estimated to be 5.1×10^{-7} M at 287 min reaction time.

To summarize, the overall studies successfully determined the binding kinetics of CBMs on crystalline cellulose, as well as the structural changes of plant cell wall surface before and after pretreatment at single molecule level. The in-depth understanding of the binding mechanisms of the CBM-cellulose interactions may pave the way for more efficient plant cell wall degradation and eventually facilitate biofuel production. This research also provides a radical method for the study of single-molecule affinity between CBM and cellulose that is critical to the engineering of novel cellulolytic enzymes.

6.2 Outlook

Investigating the binding behavior of specific CBM with known properties may improve understanding of the mechanism of enzyme-plant cell wall interaction.

a. This approach can be applied to study the intricate architecture, especially the surface morphology of the plant cell walls; meanwhile dissect the major components and their distribution in the plant cell walls. For instance, CBMs of different types and/or from different families which target amorphous cellulose or hemicellulose, have the capacity of mapping the distribution and content of the above carbohydrates on the plant cell walls. Determination of the binding specificity can be extended down to the fine microstructures, especially the linkage of cellulose to other non-carbohydrates components, such as lignin. Besides, the structure and component changes between the plant cell walls pretreated by different chemicals or procedures can be quantitatively compared by AFM recognition imaging as well.
b. The mechanisms of enzymatic hydrolysis of the plant cell walls can also be determined at single-molecule level by AFM recognition imaging and

SMDFS. The morphology of the plant cell wall surface and the structure and size of the enzymes in combination greatly affect the hydrolysis efficiency. In most cases, the specificity of the CBMs reflects the specificity of the catalytic modules, and this can be verified in the more complex hydrolysis procedure by the intact enzyme molecule. Specifically, the binding sites and hydrolysis kinetics of the intact enzyme molecule different in sizes can be quantified on diverse cell wall surfaces, and the results can be compared with that of CBM or catalytic modules only. Therefore, how the CBM targeting affect the substrate coverage by intact enzymes as well as the cellulose degradation efficiency is expected to be addressed.

c. The structural changes during plant cell wall expansion or disassembly may also be monitored at single-molecule level. For example, expansin from a distinct CBM family is a specific protein conducting expansion activity in the plant cell walls. As one of the cell wall proteins, expansin takes part in the plant cell wall loosening during plant growth, and also in the softening of fruits.[242] It has proved to induce non-hydrolytic activity on plant cell wall polysaccharides, e.g., between cellulose and xyloglucans, and break the H bonding among the polymer network to loosen and elongate the plant cell walls.[243] The reversible binding activity of single expansin molecule along the wrapped cellulose fibrils can be monitored to look into the deformation or disassembly of interwoven polysaccharides. Therefore, the mechanisms of plant cell wall expansion can be further understood based on the changes of microstructure of the plant cell walls.

REFERENCES

1. Carroll, A., Somerville, C. *Annu. Rev. Plant Biol.* **2009**, *60*, 165-182.

2. Zaldivar, J.; Nielsen, J.; Olsson, L. *Appl. Microbiol. Biot.* **2001**, *56* (1-2), 17-34.

3. Solomon, B. D. *Ecol. Econ. Rev.* **2010**, *1185*, 119-134.

4. Jordan, D. B.; Bowman, M. J.; Braker, J. D.; Dien, B. S.; Hector, R. E.; Lee, C. C.; Mertens, J. A.; Wagschal, K. *Biochem. J.* **2012**, *442*, 241-252.

5. Wei, H.; Xu, Q.; Taylor, L. E., 2nd; Baker, J. O.; Tucker, M. P.; Ding, S. Y. *Curr. Opin. Biotech.* **2009**, *20* (3), 330-338.

6. Cook, C.; Devoto, A. *J. Sci. Food Agr.* **2011**, *91* (10), 1729-1732.

7. Somerville, C.; Bauer, S.; Brininstool, G.; Facette, M.; Hamann, T.; Milne, J.; Osborne, E.; Paredez, A.; Persson, S.; Raab, T.; Vorwerk, S.; Youngs, H. *Science* **2004**, *306* (5705), 2206-2211.

8. Bailey, I. W. *Ind. Eng. Chem.* **1938**, *30* (1), 40-47.

9. Harris, P. J.; Stone, B. A. Wiley-Blackwell Oxford, 2008.

10. McCann, M. C.; Bush, M.; Milioni, D.; Sado, P.; Stacey, N. J.; Catchpole, G.; Defernez, M.; Carpita, N. C.; Hofte, H.; Ulvskov, P.; Wilson, R. H.; Roberts, K. *Phytochemistry* **2001**, *57* (6), 811-821.

11. Smith, L. G. Plant cell division: Building walls in the right places. *Nat. Rev. Mol. Cell Biol.* **2001**, *2* (1), 33-39.

12. Zeng, Y.; Zhao, S.; Yang, S.; Ding, S. Y. *Curr. Opin. Biotechnol.* **2014**, *27*, 38-45.

13. Henrissat, B. *Cellulose* **1994**, *1* (3), 169-196.

14. Himmel, M. E.; Ding, S. Y.; Johnson, D. K.; Adney, W. S.; Nimlos, M. R.; Brady, J. W.; Foust, T. D. *Science* **2007**, *315* (5813), 804-807.

15. Grabber, J. H. *Crop. Sci.* **2005**, *45* (3), 820-831.

16. Ding, S. Y.; Himmel, M. E. *J. Agr. Food Chem.* **2006**, *54* (3), 597-606.

17. Ding, S. Y.; Zhao, S.; Zeng, Y. N. *Cellulose* **2014**, *21* (2), 863-871.

18. Postek, M. T.; Vladár, A.; Dagata, J.; Farkas, N.; Ming, B.; Wagner, R.; Raman, A.; Moon, R. J.; Sabo, R.; Wegner, T. H.; Beecher, J. Development of the metrology and imaging of cellulose nanocrystals. *Meas. Sci. Technol.* **2011**, *22* (2), 024005.

19. Obel, N.; Erben, V.; Schwarz, T.; Kuhnel, S.; Fodor, A.; Pauly, M. *Molecular plant* **2009**, *2* (5), 922-932.

20. Burgert, I. *Am. J. Bot.* **2006**, *93* (10), 1391-1401.

21. Perera, P. N.; Schmidt, M.; Schuck, P. J.; Adams, P. D. *Anal. Chim. Acta* **2011**, *702* (2), 172-177.

22. Moon, R. J.; Martini, A.; Nairn, J.; Simonsen, J.; Youngblood, J. *Chem. Soc. Rev.* **2011**, *40* (7), 3941-3994.

23. Cho, H. M.; Gross, A. S.; Chu, J. W. *J. Am. Chem. Soc.* **2011**, *133* (35), 14033-14041.

24. Eichhorn, S. J.; Baillie, C. A.; Zafeiropoulos, N.; Mwaikambo, L. Y.; Ansell, M. P.; Dufresne, A.; Entwistle, K. M.; Herrera-Franco, P. J.; Escamilla, G. C.; Groom, L.; Hughes, M.; Hill, C.; Rials, T. G.; Wild, P. M. *J. Mater. Sci.* **2001**, *36* (9), 2107-2131.

25. Susheel, K.; Alain, D.; Bibin Mathew, C.; Luc, A.; James, N.; Elias, N. *Int. J.Polym. Sci.* **2011**, *2011*, 837875.

26. Bergenstrahle, M.; Thormann, E.; Nordgren, N.; Berglund, L. A. *Langmuir* **2009**, *25* (8), 4635-4642.

27. G ŕio, F. M.; Fonseca, C.; Carvalheiro, F.; Duarte, L. C.; Marques, S.; Bogel-Łukasik, R. *Bioresour. Technol.* **2010**, *101* (13), 4775-4800.

28. Nishiyama, Y.; Langan, P.; Chanzy, H. *J. Am. Chem. Soc.* **2002**, *124* (31), 9074-9082.

29. Nishiyama, Y.; Sugiyama, J.; Chanzy, H.; Langan, P. *J. Am. Chem. Soc.* **2003**, *125* (47), 14300-14306.

30. Sticklen, M. *Nat. Rev. Genet.* **2008**, *9*, 433-443.

31. Himmel, M. E.; Bayer, E. A. *Curr. Opin. Biotechnol.* **2009**, *20*, 316-317.

32. Gilbert, H. J. *Plant Physiol.* **2010**, *153*, 444-455.

33. Himmel, M. E. Blackwell Publishing, 2008.

34. Xu, Q.; Ding, S. Y.; Brunecky, R.; Bomble, Y. J.; Himmel, M. E.; Baker, J. O. *Biotechnol. Biofuels* **2013**, *6* (1), 126.

35. Matthews, J. F.; Skopec, C. E.; Mason, P. E.; Zuccato, P.; Torget, R. W.; Sugiyama, J.; Himmel, M. E.; Brady, J. W. *Carbohyd. Res.* **2006**, *341* (1), 138-152.

36. Mazeau, K. *Carbohyd. Polym.* **2011**, *84* (1), 524-532.

37. Donohoe, B. S.; Decker, S. R.; Tucker, M. P.; Himmel, M. E.; Vinzant, T. B. *Biotechnol. Bioeng.* **2008**, *101* (5), 913-925.

38. G ŕio, F.M.; Fonseca, C.; Carvalheiro, F.; Duarte, L. C.; Marques, S.; Bogel-Łukasik, R. *Bioresour. Technol.* **2010**, *101* (13), 26.

39. Yoshida, M.; Liu, Y.; Uchida, S.; Kawarada, K.; Ukagami, Y.; Ichinose, H.; Kaneko, S.; Fukuda, K. *Biosci. Biotech. Biochem.* **2008**, *72* (3), 805-810.

40. Beckham, G. T.; Bomble, Y. J.; Bayer, E. A.; Himmel, M. E.; Crowley, M. F. Applications of computational science for understanding enzymatic deconstruction of cellulose. *Curr. Opin. Biotechnol.* **2011**, *22* (2), 231-238.

41. Cantarel, B. L.; Coutinho, P. M.; Rancurel, C.; Bernard, T.; Lombard, V.; Henrissat, B. *Nucleic Acids Res.* **2009**, *37*, D233-D238.

42. Gilbert, H. J. *Plant Physiol.* **2010**, *153* (2), 444-455.

43. Boraston, A. B.; Bolam, D. N.; Gilbert, H. J.; Davies, G. J. *Biochem. J.* **2004**, *382*, 769-781.

44. Boraston, A. B., Kwan, E., Chiu, P., Warren, R. A. J. and Kilburn, D. G. *J. Biol. Chem.* **2003**, *278*, 6120-6127.

45. Ali, M. K., Hayashi, H., Karita, S., Goto, M., Kimura, T., Sakka, K. and Ohmiya, K. *Biosci. Biotechnol. Biochem.* **2001**, *65*, 41-47.

46. Gilkes, N. R., Kilburn, D. G., Warren, R. A. J. and Miller, Jr, R. C. *J. Biol. Chem.* **1988**, *263*, 10401-10407.

47. Hall, J., Black, G. W., Ferreira, L. M., Millward-Sadler, S. J., Ali, B. R., Hazlewood, G. P. and Gilbert, H. J. *Biochem. J.* **1995**, *309*, 749-756.

48. Bolam, D. N.; Ciruela, A.; McQueen-Mason, S.; Simpson, P.; Williamson, M. P.; Rixon, J. E.; Boraston, A.; Hazlewood, G. P.; Gilbert, H. J. *Biochem. J.* **1998**, *331*, 775-781.

49. Tomme, P.; Vantilbeurgh, H.; Pettersson, G.; Vandamme, J.; Vandekerckhove, J.; Knowles, J.; Teeri, T.; Claeyssens, M. *Eur. J. Biochem.* **1988**, *170* (3), 575-581.

50. Betzig, E.; Patterson, G. H.; Sougrat, R.; Lindwasser, O. W.; Olenych, S.; Bonifacino, J. S.; Davidson, M. W.; Lippincott-Schwartz, J.; Hess, H. F. *Science* **2006**, *313*, 1642-1645.

51. Greenleaf, W. J.; Woodside, M. T.; Block, S. M. *Annu. Rev. Biophys. Biomol.* **2007**, *36*, 171-190.

52. Qian, X. H.; Ding, S. Y.; Nimlos, M. R.; Johnson, D. K.; Himmel, M. E. *Macromolecules* **2005**, *38* (25), 10580-10589.

53. Thuvander, F.; Kifetew, G.; Berglund, L. A. *Wood Sci. Technol.* **2002**, *36* (3), 241-254.

54. Xu, G. Y.; Ong, E.; Gilkes, N. R.; Kilburn, D. G.; Muhandiram, D. R.; Harris-Brandts, M.; Carver, J. P.; Kay, L. E.; Harvey, T. S. *Biochemistry* **1995**, *34* (21), 6993-7009.

55. Simpson, P. J.; Xie, H.; Bolam, D. N.; Gilbert, H. J.; Williamson, M. P. *J. Biol. Chem.* **2000**, *275* (52), 41137-41142.

56. Mulakala, C.; Reilly, P. J. *Proteins* **2005**, *61* (3), 590-596.

57. Boraston, A. B. *Biochem. J.* **2005**, *385*, 479-484.

58. McCartney, L.; Blake, A. W.; Flint, J.; Bolam, D. N.; Boraston, A. B.; Gilbert, H. J.; Knox, J. P. *Proc. Natl. Acad. Sci. USA* **2006**, *103* (12), 4765-4770.

59. Cicortas Gunnarsson, L.; Montanier, C.; Tunnicliffe, R. B.; Williamson, M. P.; Gilbert, H. J.; Nordberg Karlsson, E.; Ohlin, M. *Biochem. J.* **2007**, *406* (2), 209-214.

60. Abbott, D. W.; Ficko-Blean, E.; van Bueren, A. L.; Rogowski, A.; Cartmell, A.; Coutinho, P. M.; Henrissat, B.; Gilbert, H. J.; Boraston, A. B. *Biochemistry* **2009**, *48* (43), 10395-10404.

61. Adam, M. A. M.; Phillips, M. S.; Jones, J. T.; Blok, V. C. *Physiol. Mol. Plant P.* **2008**, *72* (1-3), 21-28.

62. Zhao, X.; Rignall, T. R.; McCabe, C.; Adney, W. S.; Himmel, M. E. *Chem. Phys. Lett.* **2008**, *460* (1-3), 284-288.

63. Mulakala, C.; Reilly, P. J. *Proteins* **2005**, *60* (4), 598-605.

64. Zhong, L.; Matthews, J. F.; Hansen, P. I.; Crowley, M. F.; Cleary, J. M.; Walker, R. C.; Nimlos, M. R.; Brooks, C. L., 3rd; Adney, W. S.; Himmel, M. E.; Brady, J. W. *Carbohyd. Res.* **2009**, *344* (15), 1984-1992.

65. Yui, T.; Shiiba, H.; Tsutsumi, Y.; Hayashi, S.; Miyata, T.; Hirata, F. *J. Phys. Chem. B* **2010**, *114* (1), 49-58.

66. Shimon, L. J. W.; Pages, S.; Belaich, A.; Belaich, J. P.; Bayer, E. A.; Lamed, R.; Shoham, Y.; Frolow, F. *Acta Crystallogr. D* **2000**, *56*, 1560-1568.

67. Lehtio, J.; Sugiyama, J.; Gustavsson, M.; Fransson, L.; Linder, M.; Teeri, T. T. *Proc. Natl. Acad. Sci. USA* **2003**, *100* (2), 484-489.

68. Tormo, J.; Lamed, R.; Chirino, A. J.; Morag, E.; Bayer, E. A.; Shoham, Y.; Steitz, T. A. Crystal structure of a bacterial family-III cellulose-binding domain: A general mechanism for attachment to cellulose. *Embo. J.* **1996**, *15* (21), 5739-5751.

69. McLean, B. W.; Bray, M. R.; Boraston, A. B.; Gilkes, N. R.; Haynes, C. A.; Kilburn, D. G. *Protein Eng.* **2000**, *13* (11), 801-809.

70. Gierlinger, N.; Schwanninger, M. *Plant Physiol.* **2006**, *140* (4), 1246-1254.

71. Van Sandt, V. S.; Suslov, D.; Verbelen, J. P.; Vissenberg, K. **2007**, *100* (7), 1467-1473.

72. Steinbach, G.; Pomozi, I.; Zsiros, O.; Pay, A.; Horvath, G. V.; Garab, G. *Cytometry A* **2008**, *73* (3), 202-208.

73. Richter, S.; Mussig, J.; Gierlinger, N. *Planta* **2011**, *233* (4), 763-772.

74. Agarwal, U.; Atalla, R. *Planta* **1986**, *169* (3), 325-332.

75. Zhao, X. B.; Zhang, L. H.; Liu, D. H. *Biofuels Bioprod. Biorefin.* **2012**, *6* (5), 561-579.

76. Chen, Y.; Stevens, M. A.; Zhu, Y. M.; Holmes, J.; Moxley, G.; Xu, H. *J. Ind. Microbiol. Biot.* **2012**, *39* (5), 691-700.

77. Kumar, R.; Mago, G.; Balan, V.; Wyman, C. E. *Bioresour. Technol.* **2009**, *100* (17), 3948-3962.

78. Chundawat, S. P. S.; Donohoe, B. S.; Sousa, L. D.; Elder, T.; Agarwal, U. P.; Lu, F. C.; Ralph, J.; Himmel, M. E.; Balan, V.; Dale, B. E. *Energy Environ. Sci.* **2011**, *4* (3), 973-984.

79. Ifuku, S.; Nogi, M.; Abe, K.; Handa, K.; Nakatsubo, F.; Yano, H. *Biomacromolecules* **2007**, *8* (6), 1973-1978.

80. Berlioz, S.; Molina-Boisseau, S.; Nishiyama, Y.; Heux, L. *Biomacromolecules* **2009**, *10* (8), 2144-2151.

81. Edge, S.; Potter, U. J.; Steele, D. F.; Tobyn, M. J.; Staniforth, J. N. *Micron* **1998**, *29* (6), 469-471.

82. Ek, R.; Alderborn, G.; Nystrom, C. *Int. J. Pharm.* **1994**, *111* (1), 43-50.

83. Tetard, L.; Passian, A.; Venmar, K. T.; Lynch, R. M.; Voy, B. H.; Shekhawat, G.; Dravid, V. P.; Thundat, T. *Nat. Nanotechnol.* **2008**, *3* (8), 501-505.

84. Tetard, L.; Passian, A.; Thundat, T. *Nat. Nanotechnol.* **2009**, *5* (2), 105-109.

85. Hansma, P.; Elings, V.; Marti, O.; Bracker, C. *Science* **1988**, *242* (4876), 209-216.

86. Parot, P.; Dufrêne, Y. F.; Hinterdorfer, P.; Le Grimellec, C.; Navajas, D.; Pellequer, J. L.; Scheuring, S. *J. Mol. Recogn.* **2007**, *20* (6), 418-431.

87. Shiramine, K. I.; Muto, S.; Shibayama, T.; Sakaguchi, N.; Ichinose, H.; Kozaki, T.; Sato, S.; Nakata, Y.; Yokoyama, N.; Taniwaki, M. *J. Appl. Phys.* **2007**, *101* (3), 033524.

88. Resch, R.; Friedbacher, G.; Grasserbauer, M. *Fresen. J. Anal. Chem.* **1997**, *358* (1-2), 352-355.

89. Ke, S. H.; Uda, T.; Stich, I.; Terakura, K. *Appl. Phys. A* **2001**, *72*, S63-S66.

90. Uchihashi, T.; Ishida, T.; Komiyama, M.; Ashino, M.; Sugawara, Y.; Mizutani, W.; Yokoyama, K.; Morita, S.; Tokumoto, H.; Ishikawa, M. *Appl. Surf. Sci.* **2000**, *157* (4), 244-250.

91. Gainutdinov, R.; Arutyunov, P. *Russ. Microelectron.* **2001**, *30* (4), 219-224.

92. Gondran, C. F. H.; Michelson, D. K. *J. Vac. Sci. Technol. A* **2006**, *24* (4), 1185-1190.

93. Kuhle, A.; Sorensen, A. H.; Zandbergen, J. B.; Bohr, J. *Appl. Phys. A-Mater.* **1998**, *66*, S329-S332.

94. Ding, S. Y.; Xu, Q.; Crowley, M.; Zeng, Y.; Nimlos, M.; Lamed, R.; Bayer, E. A.; Himmel, M. E. *Curr. Opin. Biotech.* **2008**, *19* (3), 218-227.

95. Tetard, L.; Passian, A.; Farahi, R.; Kalluri, U.; Davison, B.; Thundat, T. *Ultramicroscop*y **2010**, *110* (6), 701-707.

96. Ding, S. Y.; Himmel, M. E. *J. Agric. Food Chem.* **2006**, *54* (3), 10.

97. Ding, S. Y.; Xu, Q.; Ali, M. K.; Baker, J. O.; Bayer, E. A.; Barak, Y.; Lamed, R.; Sugiyama, J.; Rumbles, G.; Himmel, M. E. *Biotechniques* **2006**, *41* (4), 435-442.

98. Li, R.; Fei, J.; Cai, Y.; Li, Y.; Feng, J.; Yao, J. *Carbohyd. Polym.* **2009**, *76* (1), 94-99.

99. Kirby, A. R.; Gunning, A. P.; Morris, V. J. *Biopolymers* **1996**, *38* (3), 355-366.

100. Kirby, A. R.; Gunning, A. P.; Waldron, K. W.; Morris, V. J.; Ng, A., *Biophys. J.* **1996**, *70* (3), 1138-1143.

101. Morris, V. J.; Gunning, A. P.; Kirby, A. R.; Round, A.; Waldron, K.; Ng, A., *Int. J. Biol. Macromol.* **1997**, *21* (1-2), 61-66.

102. Marga, F.; Grandbois, M.; Cosgrove, D. J.; Baskin, T. I. *Plant J.* **2005**, *43* (2), 181-190.

103. Fahlén, J.; Salmén, L. *Biomacromolecules* **2005**, *6* (1), 6.

104. Lacayo, C. I.; Malkin, A. J.; Holman, H. Y.; Chen, L.; Ding, S. Y.; Hwang, M. S.; Thelen, M. P. *Plant Physiol.* **2010**, *154* (1), 121-133.

105. Tingaut, P.; Zimmermann, T.; Lopez-Suevos, F. *Biomacromolecules* **2010**, *11* (2), 454-464.

106. Mccann, M. C.; Wells, B.; Roberts, K. *J. Cell Sci.* **1990**, *96*, 323-334.

107. Wistara, N.; Young, R. A. *Cellulose* 1999, *6* (4), 291-324.

108. Fujino, T.; Sone, Y.; Mitsuishi, Y.; Itoh, T. *Plant Cell Physiol.* **2000**, *41* (4), 486-494.

109. Simola-Gustafsson, J.; Hortling, B.; Peltonen, J. *J. Colloid Polym. Sci.* **2001**, *279* (3), 221-231.

110. Baker, A. A; Helbert, W.; Sugiyama, J.; Miles, M. J. *Biophys. J.* **2000**, *79* (2), 1139-1145.

111. Baker, A. A.; Helbert, W.; Sugiyama, J.; Miles, M. J. *Appl. Phys. A-Mater.* **1998**, *66*, S559-S563.

112. Cosgrove, D. J. *Nature* **2000**, *407* (6802), 321-326.

113. Feiz, L.; Irshad, M.; Pont-Lezica, R. F.; Canut, H.; Jamet, E. *Plant methods* **2006**, *2*, 10.

114. Singh, S.; Simmons, B. A.; Vogel, K. P. *Biotechnol. Bioeng.* **2009**, *104* (1), 68-75.

115. Wan, J. Q.; Wang, Y.; Xiao, Q. *Bioresour. Technol.* **2010**, *101* (12), 4577-4583.

116. Gunning, A. P.; Mackie, A. R.; Kirby, A. R.; Kroon, P.; Williamson, G.; Morris, V. J. *Macromolecules* **2000**, *33* (15), 5680-5685.

117. Yu, H.; Liu, R. G.; Shen, D. W.; Wu, Z. H.; Huang, Y. *Carbohyd. Polym.* **2008**, *72* (1), 122-127.

118. Roman, M.; Winter, W. T. *Biomacromolecules* **2004**, *5* (5), 1671-1677.

119. Li, R. J.; Fei, J. M.; Cai, Y. R.; Li, Y. F.; Feng, J. Q.; Yao, J. M. *Carbohyd. Polym.* 2009, *76* (1), 94-99.

120. Yokota, S.; Ueno, T.; Kitaoka, T.; Wariishi, H. *Carbohyd. Res.* **2007**, *342* (17), 2593-2598.

121. Zhang, Y. H.; Cui, J.; Lynd, L. R.; Kuang, L. R. *Biomacromolecules* **2006**, *7* (2), 644-648.

122. Beck-Candanedo, S.; Roman, M.; Gray, D. G. *Biomacromolecules* **2005**, *6* (2), 1048-1054.

123. Hsu, J. C.; Penner, M. H. *J. Agr. Food Chem.* **1991**, *39* (8), 1444-1447.

124. Kvien, I.; Tanem, B. S.; Oksman, K. *Biomacromolecules* **2005**, *6* (6), 3160-3165.

125. Kontturi, E.; Vuorinen, T. *Cellulose* **2009**, *16* (1), 65-74.

126. White, A. R.; Brown, R. M. *Proc. Natl. Acad. Sci. USA* **1981**, *78* (2), 1047-1051.

127. Imai, T.; Boisset, C.; Samejima, M.; Igarashi, K.; Sugiyama, J. *Febs. Lett.* **1998**, *432* (3), 113-116.

128. Lee, I.; Evans, B. R.; Woodward, J. *Ultramicroscopy* **2000**, *82* (1-4), 213-221.

129. Filonova, L.; Gunnarsson, L. C.; Daniel, G.; Ohlin, M. *BMC Plant Biol.* **2007**, *7* 54.

130. Machado, J.; Araujo, A.; Pinto, R.; Gama, F. M. *Cellulose* **2009**, *16* (5), 817-824.

131. Lee, I.; Evans, B. R.; Lane, L. M.; Woodward, J. *Bioresource. Technol.* **1996**, *58* (2), 163-169.

132. Divne, C.; Stahlberg, J.; Teeri, T. T.; Jones, T. A. *J. Mol. Biol.* **1998**, *275*, (2) 309-325.

133. Liu, Y. S.; Zeng, Y.; Luo, Y.; Xu, Q.; Himmel, M. E.; Smith, S. J.; Ding, S. Y. *Cellulose* **2009**, *16* (4), 587-597.

134. Liu, H.; Fu, S.; Zhu, J.; Li, H.; Zhan, H. *Enzyme. Microb. Tech.* **2009**, *45* (4), 274-281.

135. Altaner, C.; Knox, J. P.; Jarvis, M. C. *Bioresources* **2007**, *2* (2), 284-295.

136. Igarashi, K.; Koivula, A.; Wada, M.; Kimura, S.; Penttila, M.; Samejima, M. *J. Biol. Chem.* **2009**, *284* (52), 36186-36190.

137. Hildén, L., Johansson, G. *Biotechnol. Lett.* **2004**, *26*, 1683-1963.

138. Porter, S. E.; Donohoe, B. S.; Beery, K. E.; Xu, Q.; Ding, S. Y.; Vinzant, T. B.; Abbas, C. A.; Himmel, M. E. *Biotechnol. Bioeng.* **2007**, *98* (1), 123-131.

139. Carrard, G.; Koivula, A.; Soderlund, H.; Beguin, P. *Proc. Natl. Acad. Sci. USA* **2000**, *97* (19), 10342-10347.

140. Hildén, L.; Daniel, G.; Johansson, G. *Biotechnol. Lett.* **2003**, *25* (7), 553-558.

141. Georgelis, N.; Yennawar, N. H.; Cosgrove, D. J. *Proc. Natl. Acad. Sci. USA* **2012**, *109* (37), 14830-14835.

142. McLean, B. W.; Boraston, A. B.; Brouwer, D.; Sanaie, N.; Fyfe, C. A.; Warren, R. A.; Kilburn, D. G.; Haynes, C. A. *J. Biol. Chem.* **2002**, *277* (52), 50245-50254.

143. Carrard, G.; Linder, M. *Eur. J. Biochem.* **1999**, *262* (3), 637-643.

144. Zhong, L. H.; Matthews, J. F.; Hansen, P. I.; Crowley, M. F.; Cleary, J. M.; Walker, R. C.; Nimlos, M. R.; Brooks, C. L.; Adney, W. S.; Himmel, M. E.; Brady, J. W. *Carbohyd. Res.* **2009**, *344* (15), 1984-1992.

145. Li, T.; Yan, S.; Yao, L. *J. Mol. Model.* **2012**, *18* (4), 1355-1364.

146. Nimlos, M. R.; Matthews, J. F.; Crowley, M. F.; Walker, R. C.; Chukkapalli, G.; Brady, J. W.; Adney, W. S.; Cleary, J. M.; Zhong, L.; Himmel, M. E. *Protein Eng. Des. Sel.* **2007**, *20* (4), 179-187.

147. Noy, A.; Vezenov, D. V.; Kayyem, J. F.; Meade, T. J.; Lieber, C. M. *Chem. Biol.* **1997**, *4* (7), 519-527.

148. A-Hassan, E.; Heinz, W. F.; Antonik, M. D.; D'Costa, N. P.; Nageswaran, S.; Schoenenberger, C. A.; Hoh, J. H. *Biophys. J.* **1998**, *74* (3), 1564-1578.

149. Stroh, C.; Wang, H.; Bash, R.; Ashcroft, B.; Nelson, J.; Gruber, H.; Lohr, D.; Lindsay, S. M.; Hinterdorfer, P. *Proc. Natl. Acad. Sci. USA* **2004**, *101* (34), 12503-12507.

150. Johnson, W. T., Kada, G., Stroh, C., Gruber, H., Wang, H., Kienberger, F., Ebner, A., Lindsay, S. and Hinterdorfer, P. Simultaneous Topography and RECognition

Mapping with PicoTRECTM: A Powerful New Technology That Can Be Used To Map Nanometer-Scale Molecular Binding Sites On A Variety Of Surfaces, *Nanotechnology Conference and Trade Show*, pp. 679-682, **2005**, Anaheim, California, U.S.A.

151. Kienberger, F.; Ebner, A.; Gruber, H. J.; Hinterdorfer, P. *Acc. Chem. Res.* **2006**, *39* (1), 29-36.

152. Yu, J.; Jiang, Y.; Ma, X.; Lin, Y.; Fang, X. *Chem. Asian J.* **2007**, *2* (2), 284-289.

153. Dufrêne, Y. F.; Hinterdorfer, P. *Pflugers Arch.* **2008**, *456* (1), 237-245.

154. Muller, D. J.; Helenius, J.; Alsteens, D.; Dufrêne, Y. F. *Nat. Chem. Biol.* **2009**, *5* (6), 383-390.

155. Dong, M.; Sahin, O. *Nat. Commun.* **2011**, *2*, 247.

156. Liu, K.; Song, Y.; Feng, W.; Liu, N.; Zhang, W.; Zhang, X. *J. Am. Chem. Soc.* **2011**, *133* (10), 3226-3229.

157. Li, Y.; Qiao, H.; Xing, C.; Zhang, J.; Wang, L. X.; Wang, H.; Zhang, B.; Tang, J. *J. Struct. Biol.* **2011**, *176* (1), 46-51.

158. Landoulsi, J.; Dupres, V. *Chemphyschem* **2011**, ***12*** (7), 1310-1316.

159. Friddle, R. W.; Battle, K.; Trubetskoy, V.; Tao, J.; Salter, E. A.; Moradian-Oldak, J.; De Yoreo, J. J.; Wierzbicki, A. *Angew. Chem*. **2011**, *50* (33), 7541-7545.

160. Mori, T.; Asakura, M.; Okahata, Y. *J. Am. Chem. Soc.* **2011**, *133* (15), 5701-5703.

161. Kamruzzahan, A. S.; Ebner, A.; Wildling, L.; Kienberger, F.; Riener, C. K.; Hahn, C. D.; Pollheimer, P. D.; Winklehner, P.; Holzl, M.; Lackner, B.; Schorkl, D. M.; Hinterdorfer, P.; Gruber, H. J. *Bioconjugate Chem.* **2006**, *17* (6), 1473-1481.

162. Puntheeranurak, T.; Wimmer, B.; Castaneda, F.; Gruber, H. J.; Hinterdorfer, P.; Kinne, R. K. *Biochemistry* **2007**, *46* (10), 2797-2804.

163. Tang, J.; Ebner, A.; Ilk, N.; Lichtblau, H.; Huber, C.; Zhu, R.; Pum, D.; Leitner, M.; Pastushenko, V.; Gruber, H. J.; Sleytr, U. B.; Hinterdorfer, P. *Langmuir* **2008**, *24*,(4), 1324-1329.

164. Tang, J.; Ebner, A.; Badelt-Lichtblau, H.; Vollenkle, C.; Rankl, C.; Kraxberger, B.; Leitner, M.; Wildling, L.; Gruber, H. J.; Sleytr, U. B.; Ilk, N.; Hinterdorfer, P. *Nano Lett.* **2008**, *8* (12), 4312-4319.

165. Zhu, R.; Howorka, S.; Proll, J.; Kienberger, F.; Preiner, J.; Hesse, J.; Ebner, A.; Pastushenko, V. P.; Gruber, H. J.; Hinterdorfer, P. *Nat. Nanotechnol.* **2010**, *5* (11), 788-791.

166. Wildling, L.; Unterauer, B.; Zhu, R.; Rupprecht, A.; Haselgrubler, T.; Rankl, C.; Ebner, A.; Vater, D.; Pollheimer, P.; Pohl, E. E.; Hinterdorfer, P.; Gruber, H. J. *Bioconjugate Chem.* **2011**, *22* (6), 1239-1248.

167. Leitner, M.; Mitchell, N.; Kastner, M.; Schlapak, R.; Gruber, H. J.; Hinterdorfer, P.; Howorka, S.; Ebner, A. *ACS nano* **2011**, *5* (9), 7048-7054.

168. Puntheeranurak, T.; Neundlinger, I.; Kinne, R. K.; Hinterdorfer, P. *Nat. Protoc.* **2011**, *6* (9), 1443-1452.

169. Touhami, A.; Hoffmann, B.; Vasella, A.; Denis, F. A.; Dufrêne, Y. F. *Langmuir* **2003**, *19* (5), 1745-1751.

170. Dupres, V.; Verbelen, C.; Dufrêne, Y. F. *Biomaterials.* **2007**, *28* (15), 2393-2402.

171. Wang, B.; Guo, C.; Chen, G.; Park, B.; Xu, B. *Chem. Commun.* **2012**, *48* (1), 1644-1646..

172. Ebner, A.; Kienberger, F.; Kada, G.; Stroh, C. M.; Geretschlager, M.; Kamruzzahan, A. S. M.; Wildling, L.; Johnson, W. T.; Ashcroft, B.; Nelson, J.; Lindsay, S. M.; Gruber, H. J.; Hinterdorfer, P. *Chemphyschem* **2005**, *6* (5), 897-900.

173. Lee, S.; Mandic, J.; Van Vliet, K. J. *Proc. Natl. Acad. Sci. USA* **2007**, *104* (23), 9609-9614.

174. Hinterdorfer, P.; Dufrêne, Y. F. *Nat. Methods* **2006**, *3* (5), 347-355.

175. Zlatanova, J.; Lindsay, S. M.; Leuba, S. H. *Prog. Biophys. Mol. Bio.* **2000**, *74* (1-2), 37-61.

176. Lee, C. K.; Wang, Y. M.; Huang, L. S.; Lin, S. M. *Micron* **2007**, *38* (5), 446-461.

177. Bell, G. I. *Science* **1978**, *200* (4342), 618-627.

178. Jarzynski, C. *Phys. Rev. E* **1997**, *56* (5), 5018-5035.

179. Wang, W.; Yuan, T.; Wang, K.; Cui, B.; Dai, Y. *Bioresour. Technol.* **2012**, *107*, 282-286.

180. Blake, A. W.; McCartney, L.; Flint, J. E.; Bolam, D. N.; Boraston, A. B.; Gilbert, H. J.; Knox, J. P. *J. Biol. Chem.* **2006**, *281* (39), 29321-29329.

181. Zhang, M. M.; Wu, S. C.; Zhou, W.; Xu, B. Q. *J. Phys. Chem. B* **2012**, *116* (33), 9949-9956. Copyright 2012 American Chemical Society

182. Nowak, C.; Schach, D.; Gebert, J.; Grosserueschkamp, M.; Gennis, R. B.; Ferguson-Miller, S.; Knoll, W.; Walz, D.; Naumann, R. L. C. *J. Solid State Electr.* **2011**, *15* (1), 105-114.

183. Hainfeld, J. F.; Liu, W.; Halsey, C. M.; Freimuth, P.; Powell, R. D. *J. Struct. Biol.* **1999**, *127* (2), 185-198.

184. Jain, P. K.; Huang, X.; El-Sayed, I. H.; El-Sayad, M. A. *Plasmonics* **2007**, *2* (3), 107-118.

185. Chen, G. J.; Zhou, J. F.; Park, B.; Xu, B. Q. *Appl. Phys. Lett.* **2009**, *95* (4), 043103.

186. Xu, Q.; Tucker, M. P.; Arenkiel, P.; Ai, X.; Rumbles, G.; Sugiyama, J.; Himmel, M. E.; Ding, S. Y. *Cellulose* **2009**, *16* (1), 19-26.

187. Grandbois, M.; Beyer, M.; Rief, M.; Clausen-Schaumann, H.; Gaub, H. E. *Science* **1999**, *283* (5408), 1727-1730.

188. Toone, E. J. *Curr. Opin. Struc. Biol.* **1994**, *4* (5), 719-728.

189. Murashima, K.; Kosugi, A.; Doi, R. H. *J. Bacteriol.* **2005**, *187* (20), 7146-7149.

190. Hervé, C.; Rogowski, A.; Blake, A. W.; Marcus, S. E.; Gilbert, H. J.; Knox, J. P. *Proc. Natl. Acad. Sci. USA* **2010**, *107* (34), 15293-15298.

191. Thormann, E.; Simonsen, A. C.; Nielsen, L. K.; Mouritsen, O. G. *J. Mol. Recognit.* **2007**, *20* (6), 554-560.

192. Zawadzki, K. M.; Yaspelkis, B. B.; Ivy, J. L. *J. Appl. Physiol.* **1992**, *72* (5), 1854-1867.

193. Chen, I. J.; Chen, H. L.; Demetriou, M. *J. Biol. Chem.* **2007**, *282* (48), 35361-35372.

194. Matthews, J. F.; Beckham, G. T.; Bergenstrahle-Wohlert, M.; Brady, J. W.; Himmel, M. E.; Crowley, M. F. *J. Chem. Theory Comput.* **2012**, *8* (2), 735-748.

195. Kienberger, F.; Kada, G.; Mueller, H.; Hinterdorfer, P. *J. Mol. Biol.* **2005**, *347* (3), 597-606.

196. Zhang, M. M.; Wang, B.; Xu, B. Q. *Phys. Chem. Chem. Phys.* **2013**, *15* (17), 6508-6515. Copyright 2013 Royal Society of Chemistry

197. Evans, E. B. *Biophys. Chem.* **1999**, *82* (2-3), 83-97.

198. Evans, E.; Ritchie, K. *Biophys. J.* **1997**, *72* (4), 1541-1555.

199. Evans, E. *Annu. Rev. Biophys. Biomol. Struct.* **2001**, *30*, 105-128.

200. Merkel, R.; Nassoy, P.; Leung, A.; Ritchie, K.; Evans, E. *Nature* **1999**, *397* (6714), 50-53.

201. Hummer, G.; Szabo, A. *Acc. Chem. Res.* **2005**, *38* (7), 504-513.

202. Dong, X. M.; Revol, J. F.; Gray, D. G. *Cellulose* **1998**, *5* (1), 19-32.

203. Huang, Z. F.; Xu, B. Q.; Chen, Y. C.; Di Ventra, M.; Tao, N. J. *Nano Lett.* **2006**, *6* (6), 1240-1244.

204. Yuan, C. B.; Chen, A.; Kolb, P.; Moy, V. T. *Biochemistry* **2000**, *39* (33), 10219-10223.

205. Chundawat, S. P. S.; Beckham, G. T.; Himmel, M. E.; Dale, B. E. *Annu. Rev. Chem. Biomol. Eng.* **2011**, *2*, 121-145.

206. Martinez, A. T.; Speranza, M.; Ruiz-Duenas, F. J.; Ferreira, P.; Camarero, S.; Guillen, F.; Martinez, M. J.; Gutierrez, A.; del Rio, J. C. *Int. Microbiol.* **2005**, *8* (3), 195-204.

207. Yang, B.; Wyman, C. E. *Biofuels Bioprod. Biorefin.* **2008**, *2* (1), 26-40.

208. Jeoh, T.; Ishizawa, C. I.; Davis, M. F.; Himmel, M. E.; Adney, W. S.; Johnson, D. K. *Biotechnol. Bioeng.* **2007**, *98* (1), 112-122.

209. Lau, M. W.; Gunawan, C.; Dale, B. E. *Biotechnol. Biofuels* **2009**, *2*.

210. Li, J. B.; Henriksson, G.; Gellerstedt, G. *Bioresour. Technol.* **2007**, *98* (16), 3061-3068.

211. Zhang, H.; Thygesen, L. G.; Mortensen, K.; Kadar, Z.; Lindedam, J.; Jorgensen, H.; Felby, C. *Biotechnol. Biofuels* **2014**, *7*.

212. Bals, B.; Rogers, C.; Jin, M. J.; Balan, V.; Dale, B. *Biotechnol. Biofuels* **2010**, *3*.

213. Kim, T. H.; Lee, Y. Y. *Bioresour. Technol.* **2005**, *96* (18), 2007-2013.

214. Kaar, W. E.; Holtzapple, M. T. *Biomass Bioenerg.* **2000**, *18* (3), 189-199.

215. Foston, M.; Ragauskas, A. J. *Biomass Bioenerg.* **2010**, *34* (12), 1885-1895.

216. Gao, X.; Kumar, R.; Singh, S.; Simmons, B. A.; Balan, V.; Dale, B. E.; Wyman, C. E. *Biotechnol. Biofuels* **2014**, *7*.

217. Baboukani, B. S.; Vossoughi, M.; Alemzadeh, I. *Biosyst. Eng.* **2012**, *111* (2), 166-174.

218. Bondesson, P. M.; Galbe, M.; Zacchi, G. *Biotechnol. Biofuels* **2013**, *6*.

219. Ishizawa, C. I.; Jeoh, T.; Adney, W. S.; Himmel, M. E.; Johnson, D. K.; Davis, M. F. *Cellulose* **2009**, *16* (4), 677-686.

220. Moxley, G.; Gaspar, A. R.; Higgins, D.; Xu, H. *J. Ind. Microbiol. Biot.* **2012**, *39* (9), 1289-1299.

221. Selig, M. J.; Viamajala, S.; Decker, S. R.; Tucker, M. P.; Himmel, M. E.; Vinzant, T. B. *Biotechnol. Progr.* **2007**, *23* (6), 1333-1339.

222. Donohoe, B. S.; Vinzant, T. B.; Elander, R. T.; Pallapolu, V. R.; Lee, Y. Y.; Garlock, R. J.; Balan, V.; Dale, B. E.; Kim, Y.; Mosier, N. S.; Ladisch, M. R.; Falls, M.; Holtzapple, M. T.; Sierra-Ramirez, R.; Shi, J.; Ebrik, M. A.; Redmond, T.; Yang, B.;

Wyman, C. E.; Hames, B.; Thomas, S.; Warner, R. E. *Bioresour. Technol.* **2011**, *102* (24), 11097-11104.

223. Kristensen, J. B.; Thygesen, L. G.; Felby, C.; Jorgensen, H.; Elder, T. *Biotechnol. Biofuels* **2008**, *1* (1), 5.

224. Kawakubo, T.; Karita, S.; Araki, Y.; Watanabe, S.; Oyadomari, M.; Takada, R.; Tanaka, F.; Abe, K.; Watanabe, T.; Honda, Y.; Watanabe, T. *Biotechnol. Bioeng.* **2010**, *105* (3), 499-508.

225. Jung, S.; Foston, M.; Sullards, M. C.; Ragauskas, A. J. *Energ. Fuels* **2010**, *24*, 1347-1357.

226. Zhang, M. M.; Chen, G. J.; Kumar, R.; Xu, B. Q. *Biotechnol. Biofuels* **2013**, *6*. Copyright 2013 BioMed Central

227. Liu, C. G.; Wyman, C. E. *Ind. Eng. Chem. Res.* **2003**, *42* (21), 5409-5416.

228. Hansen, M. A. T.; Kristensen, J. B.; Felby, C.; Jorgensen, H. *Bioresour. Technol.* 2011, *102* (3), 2804-2811.

229. Wang, B.; Guo, C. L.; Zhang, M. M.; Park, B.; Xu, B. Q. *J. Phys. Chem. B* **2012**, *116* (17), 5316-5322.

230. Kumar, R.; Hu, F.; Sannigrahi, P.; Jung, S.; Ragauskas, A. J.; Wyman, C. E. *Biotechnol. Bioeng.* **2013**, *110* (3), 737-753.

231. Sannigrahi, P.; Kim, D. H.; Jung, S.; Ragauskas, A. *Energy Environ. Sci.* **2011**, *4* (4), 1306-1310.

232. Chundawat, S. P.; Venkatesh, B.; Dale, B. E. *Biotechnol. Bioeng.* **2007**, *96* (2), 219-231.

233. Nidetzky, B.; Steiner, W.; Claeyssens, M. *Biochem. J.* **1994**, *303*, 817-823.

234. Linder, M.; Teeri, T. T. *Proc. Natl. Acad. Sci. USA* **1996,** *93* (22), 12251-12255.

235. Tomme, P.; Boraston, A.; McLean, B.; Kormos, J.; Creagh, A. L.; Sturch, K.; Gilkes, N. R.; Haynes, C. A.; Warren, R. A. J.; Kilburn, D. G. *J. Chromatogr. B* **1998**, *715* (1), 283-296.

236. Goldstein, M. A.; Takagi, M.; Hashida, S.; Shoseyov, O.; Doi, R. H.; Segel, I. H. *J. Bacteriol.* **1993**, *175*, (18), 5762-5768.

237. Jervis, E. J.; Haynes, C. A.; Kilburn, D. G. *J. Biol. Chem.* **1997**, *272* (38), 24016-24023.

238. Kurasin, M.; Valjamae, P. *J. Biol. Chem.* **2011**, *286* (1), 169-177.

239. Zhang, M. M.; Wang, B.; Xu, B. Q. *J. Phys. Chem. B* **2014**, *118* (24), 6714-6720.

240. Gill, J.; Rixon, J. E.; Bolam, D. N.; McQueen-Mason, S.; Simpson, P. J.; Williamson, M. P.; Hazlewood, G. P.; Gilbert, H. J. *Biochem. J.* **1999**, *342*, 473-480.

241. Din, N.; Gilkes, N. R.; Tekant, B.; Miller, R. C.; Warren, A. J.; Kilburn, D. G., *Nat. Biotechnol.* **1991**, *9* (11), 1096-1099.

242. Cosgrove, D. J. *Nature* **2000**, *407* (6802), 321-326.

243. Mcqueenmason, S. J.; Cosgrove, D. J. *Plant Physiol.* **1995**, *107* (1), 87-100.